Electron Optics Simulation for Designing Carbon Nanotube based Field Emission X-Ray Source

by
Shabana Sultana

A dissertation submitted to the faculty of the University of North Carolina at Chapel Hill in partial fulfillment of the requirement for the degree of Doctor of Philosophy in the Curriculum in Applied Science and Engineering.

Chapel Hill
2010

Approved by

Advisor: Dr. Jianping Lu

Reader: Dr. Otto Zhou

Reader: Dr. Sha Chang

Reader: Dr. David Lalush

Reader: Dr. René López

Reader: Dr. Frank Sprenger

ABSTRACT

SHABANA SULTANA: Electron Optics Simulation for Designing Carbon Nanotube based Field Emission X-Ray Source

(Under the direction of Dr. Otto Zhou and Dr. Jianping Lu)

In this dissertation, electron optics simulation for designing carbon nanotube (CNT) based field emission x-ray source for medical imaging applications will be presented. However, for design optimization of x-ray tubes accurate electron beam optics simulation is essential. To facilitate design of CNT x-ray sources a commercial 3D finite element software has been chosen for extensive simulation. The results show that a simplified model of uniform electron field emission from the cathode surface is not sufficient when compared to experimental measurements. This necessitated the development of a refined model to describe a macroscopic field emission CNT cathode for electron beam optics simulations. The model emulates the random distribution of CNTs and the associated variation of local field enhancement factor. The main parameter of the model has been derived empirically from the experimentally measured I-V characteristics of the CNT cathode. Simulation results based on this model agree well with experiments which include measurements of the transmission rate and focus spot size. The model provides a consistent simulation platform for optimization of electron beam optics in CNT x-ray source design.

A systematic study of electron beam optics in CNT x-ray tubes led to the development of a new generation of compact x-ray source with multiple pixels. A micro focus field emission x-ray source with a variable focal spot size has been fully characterized and evaluated. It has been built and successfully integrated into micro-CT scanners which are capable of dynamic cardiac imaging of free-breathing small animals with high spatial and temporal resolutions. In addition a spatially distributed high power multi-beam x-ray source has also been designed and integrated into a stationary digital breast tomosynthesis (s-DBT) configuration. This system has the potential to reduce the total scan time to 4 seconds and yield superior image quality in breast imaging.

To
Abba, Ma
&
Shamim

ACKNOWLEDGEMENTS

I express my sincere appreciation and thanks to my advisor, Dr. Jianping Lu for his guidance throughout this work. He has been so patient and a great teacher who has helped me understand a lot of the basic science associated with this work. His thoughtful insights and his enthusiasm towards basic research has been a great inspiration for me. I extend my deepest appreciation to Dr. Otto Zhou. He has been a constant source of encouragement and guidance. I would also like to thank Dr. Frank Sprenger for his helpful discussions. I would also like to thank my committee members, Dr. Lalush, Dr. Sha Chang and Dr. Lopez for their advice and guidance.

I want to take this opportunity to thank all my group members, past and present. Last but not the least I want to thank my family for their unconditional love and support.

TABLE OF CONTENTS

LIST OF TABLE

LIST OF FIGURES

LIST OF EQUATIONS

Chapter 1 : Introduction

> “A faint fluorescence spied out of the corner of a man's eye in a darkened laboratory heralded the discovery, one hundred years ago, of a new kind of rays that would revolutionize physics and medicine.”[1]

1.1 X-Ray Imaging

This was in 1895, 8th November when Prof. Wilhelm Conrad Röntgen, a physicist at Julius Maximilian University of Würzburg in Germany, discovered x-rays during his study of cathode rays (electrons). The discovery of x-rays opened doors for a myriad of applications. It has widespread applications in science and engineering starting with physics and biology research laboratories. X-rays are used to see lattice structures in crystals to DNA strands in fibers. Even in astrophysics and cosmology x-rays have provided invaluable information. In airports x-ray scanners are omnipresent with better and advanced detection capabilities for explosives and hazardous materials. Application of x-rays in medical imaging and diagnostics has revolutionized the concept of full body scans and radiation therapy. Figure (1.1) depicts some of the applications of x-rays. In this work x-ray imaging for medical applications will be discussed in detail.

X-Ray Imaging for Medical Applications

The application of x-rays for medical diagnosis and therapy has expanded enormously since its discovery primarily due to its non-invasive technique of imaging. Today the boundary between diagnostic and therapeutic applications of x-rays is less distinct. X-ray images are incorporated directly into treatment plans to obtain real-time images during treatment.

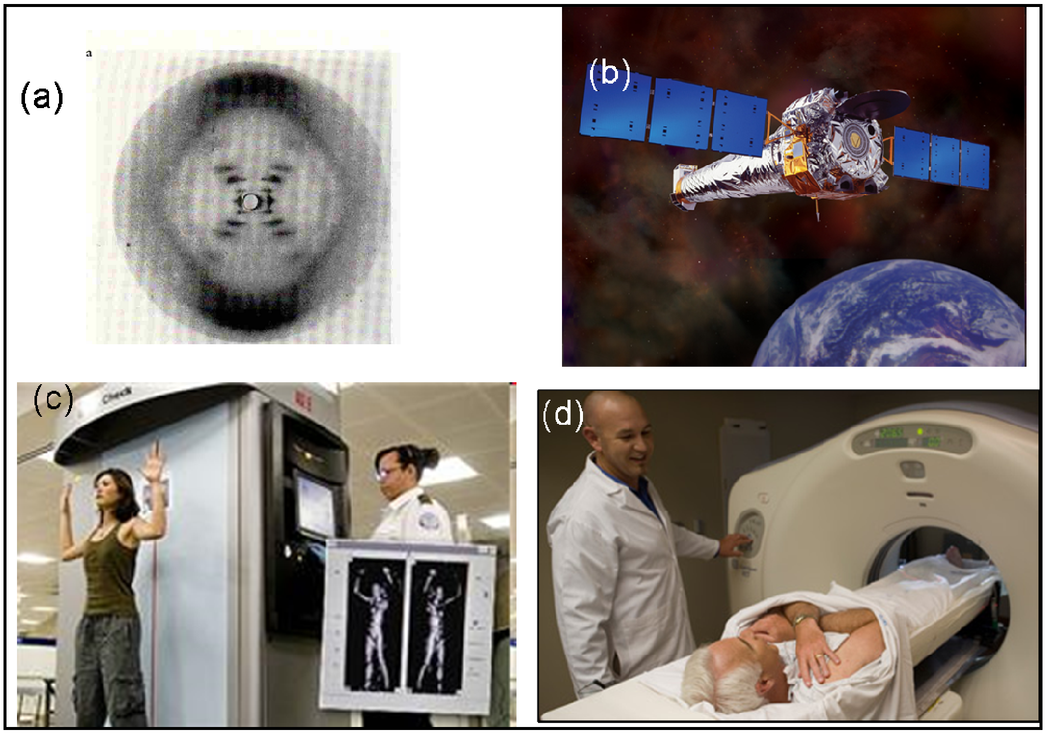

Figure 1.1 (a) The x-ray diffraction photo of B-form DNA. Image reproduced from reference [2] (b) The Chandra X-ray telescope was launched on STS-93 by NASA on July 23, 1999. (http://astronomy 2009.nasa.gov/topics_jan.htm)(c) An x-ray inspection system widely used in airport security screening purpose, this is a full body scanner. (http:// www.midlandsconnect.com /neighborhood /story.aspx?id=398827) (d) Computed tomography scanner creates several high-resolution images that are a cross-section of the scanned portion of the body (http://www.protons.com/about-us/photo-tour/when-treatment-starts.html)

X-ray Imaging can be distinguished into “Projection Radiography” and “Computed Tomography”. In projection radiography a 3D object is projected into a 2D image. Some of projection modalities include:

- *Routine diagnostic radiography,* including chest x-rays, fluoroscopy and mammography. A typical chest x-ray image can be seen in Figure (1.2).
- *Digital Radiography,* which includes all scans in routine radiography, but images are recorded digitally instead of on film.
- *Angiography,* in which the systems are specialized for imaging blood arteries and vessels.
- *Neuroradiology***,** include specialized x-ray systems for precision studies of the skull and cervical spine.
- *Mobile x-ray systems,* which are portable x-ray units designed for operating rooms or emergency vehicles.

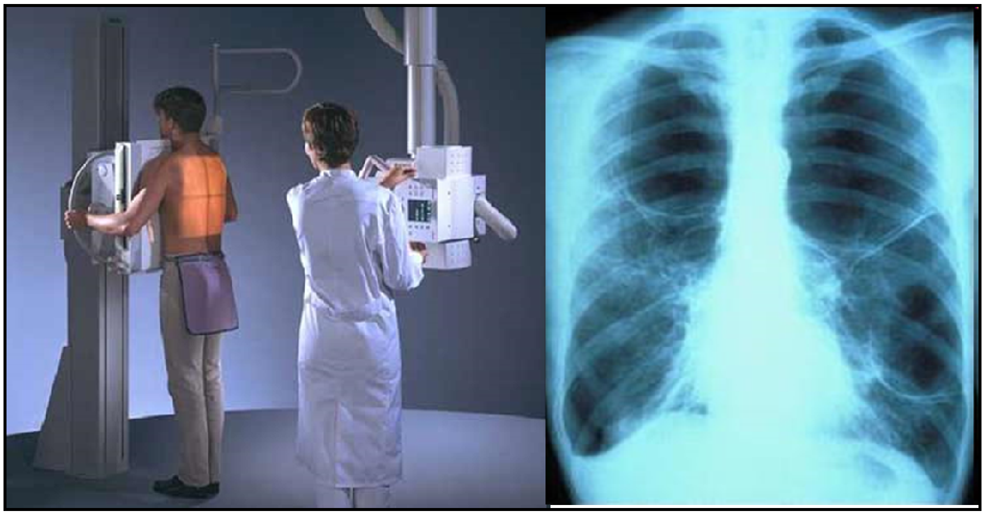

Figure 1.2. (left)Image reproduced from reference [3] (right) A typical chest X ray. This one (apparently) shows emphysema bubbles in the patient's left lung, which are severely affecting breathing. Photo courtesy of National Heart, Lung and Blood Institute (NHLBI) and National Institutes of Health.

In ‘Computed Tomography” (CT) a three dimensional image of an object is reconstructed from multiple projections images taken from different viewing angles. CT is popular because it eliminates artifacts from tissue overlap. A typical CT scanner is represented in Figure (1.3). If CT were to have separate modalities, it would be (standard) single slice CT, helical CT, and multi-slice CT.

Figure 1.3: A CT scanner where a three dimensional image is reconstructed of an object from multiple projections images taken from different viewing angles. Image reproduced from (http://www.daviddarling.info/encyclopedia/C/computed_tomography _scanning.html)

The benefit of computed tomography is that it is available for a wide range of nominal resolutions, which allows the imaging of whole bodies down to the tissue level. Figure (1.4) shows computed tomography-generated images, including high resolution CT, micro-CT and nano-CT.

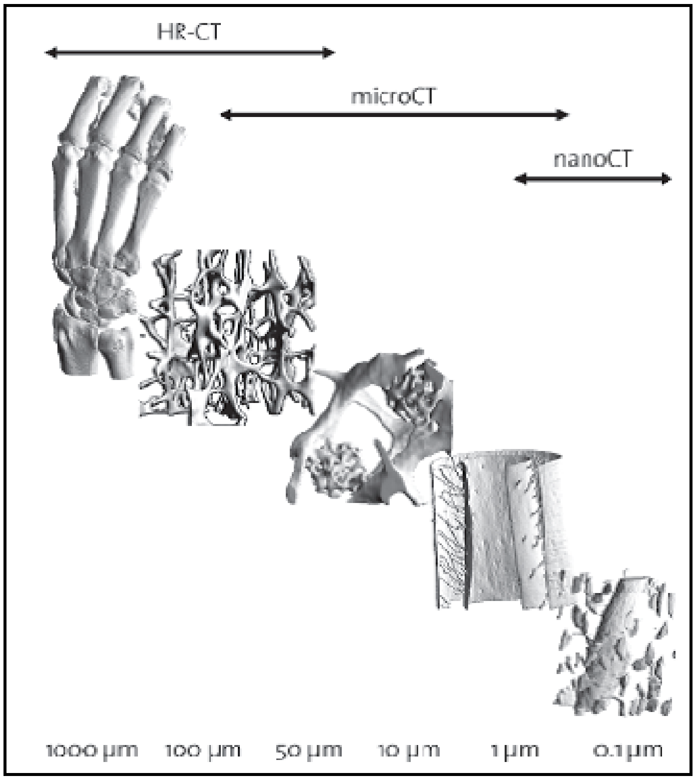

Figure 1.4: Hierarchical imaging using computed tomography (CT). The technique can be used on a large scale with different resolutions while always using the same physical principles. In high resolution CT (HR-CT) domain, normal x-ray tubes can be used as a source whereas for micro-CT special micro focus x-ray tubes are required. The lower range of micro-CT as well as the nano-CT domain is currently best assessed using synchrotron radiation (SR). The images show from left to right, the human hand, trabecular bone structure, microcallus, murine cortical bone surface of a femur with internal vasculature, and a capillary in bone surrounded by osteocyte lacunae [4].

1.2 X-Ray Source Technology

The fundamental technology of x-ray generation has not changed much since its discovery eventhough its applications have expanded vastly. Typically two main components are required for x-ray generation: a source of charged particles (most often we use electrons) and a means of accelerating or decelerating them. This simple mechanism has been used for over a century for x-ray generation and is still the dominant technique used in conventional x-ray tubes even today. Recent development of the synchrotron sources provides a different mechanism of x-ray generation; however, its engineering challenges have restricted its application. Before we go into the details of source technology here are the fundamentals of x-rays.

1.2.1 Introduction to X-Rays

X-rays were discovered in 1895, 8th November by Prof. Wilhelm Conrad Röntgen, a physicist at Julius Maximilian University of Würzburg in Germany, during his study of cathode rays (electrons). On application of a voltage difference across a glass vacuum discharge tube he saw some unknown rays were produced and he named them “X-rays” due to its unknown properties. After extensive work he discovered an intriguing property of x-rays, its strong penetrating power. It not only increased with increase in energy but also varied for different materials. Röntgen demonstrated this by taking the first ever x-ray image of his wife’s hand with a ring on her finger as shown in Figure (1.5). Prof. Röntgen received the first Nobel Prize in Physics for his extraordinary work of discovering x-rays [1].

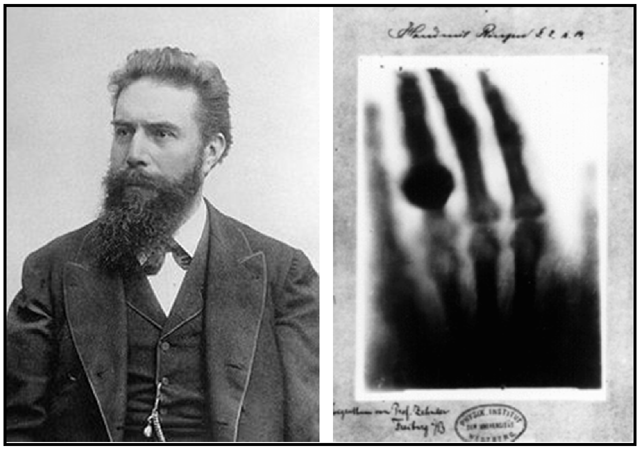

Figure 1.5: (left) Picture of the famous physicist Prof. Wilhelm Conrad Röntgen. (right) The first ever x-ray image taken, the left hand of Mrs Röntgen [5]

Energetic electrons interact and transfer energy to an absorbing medium by collisional transfer and radiative transfer. In radiative transfer, the energetic electron’s interaction with an atom produces x-rays. X-rays have high frequency and short wavelength ranging between 10^{-8} meters to 10^{-12} meters with corresponding photon energies E = 124 eV to 1.24 MeV.

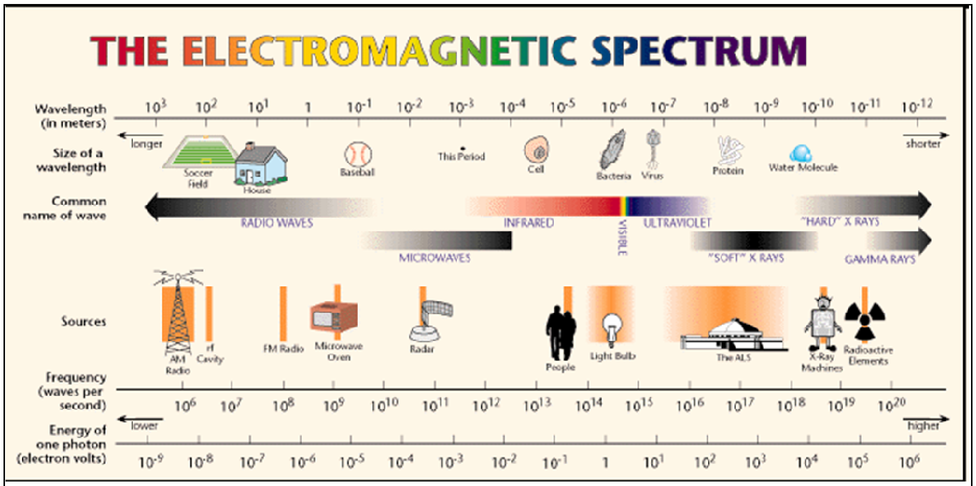

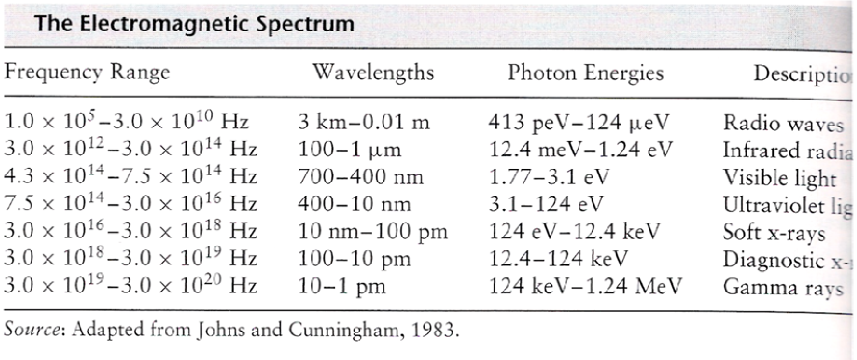
The Electromagnetic Spectrum

Frequency Range	Wavelengths	Photon Energies	Descriptio
$1.0 \times 10^5 - 3.0 \times 10^{10}$ Hz	3 km–0.01 m	413 peV–124 μeV	Radio waves
$3.0 \times 10^{12} - 3.0 \times 10^{14}$ Hz	100–1 μm	12.4 meV–1.24 eV	Infrared radia
$4.3 \times 10^{14} - 7.5 \times 10^{14}$ Hz	700–400 nm	1.77–3.1 eV	Visible light
$7.5 \times 10^{14} - 3.0 \times 10^{16}$ Hz	400–10 nm	3.1–124 eV	Ultraviolet lig
$3.0 \times 10^{16} - 3.0 \times 10^{18}$ Hz	10 nm–100 pm	124 eV–12.4 keV	Soft x-rays
$3.0 \times 10^{18} - 3.0 \times 10^{19}$ Hz	100–10 pm	12.4–124 keV	Diagnostic x-
$3.0 \times 10^{19} - 3.0 \times 10^{20}$ Hz	10–1 pm	124 keV–1.24 MeV	Gamma rays

Source: Adapted from Johns and Cunningham, 1983.

Figure 1.6: The electromagnetic spectrum with the corresponding frequency, wavelength and energies. The top image has been reproduced from reference [6]. The bottom image has been reproduced from reference [7]

X-rays are produced when energetic electrons interact with an atom. During this process two types of x-rays are produced: Bremsstrahlung radiation (which spreads over the entire energy range) and characteristic radiation (peaks at certain energies depending on the target material) as seen in Figure (1.7)

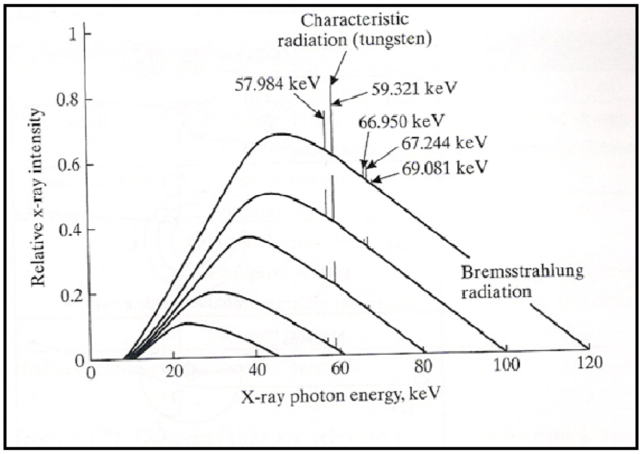

Figure 1.7: X-ray spectrum of a tungsten target. Both characteristic and Bremsstrahlung x-rays can be seen. Low energy x-rays of both types are absorbed by the medium. Image reproduced from reference [7]

1.2.2 Conventional X-Ray Source

The x-ray tube is by far the prevailing conventional x-ray source type used in medical imaging to security scanning systems. During the nascent stage of x-ray tube development, the Crookes tube was used for x-ray generation. It was a partially evacuated electrical discharge glass bulb containing two electrodes named after its inventor the British physicist William Crookes. A gaseous x-ray tube could only provide very low x-ray flux and was very unreliable which limited its applications. This led to the development of the Coolidge tube, named after its inventor, Dr. William D. Coolidge, a General Electric scientist. These tubes are called Thermionic tubes because of the thermionic electron emission mechanism. As seen in Figure (1.11), it consists of a high vacuum tube housing, a metal filament (cathode) and a target material (anode). The filament emits electrons when heated to 1000-1500º C which are then accelerated towards the target anode [8]. X-ray radiations are generated when these high energy electrons bombard the anode. Although there has been tremendous progress in terms of performance, the basic principle of x-ray generation has not changed much over the past century.

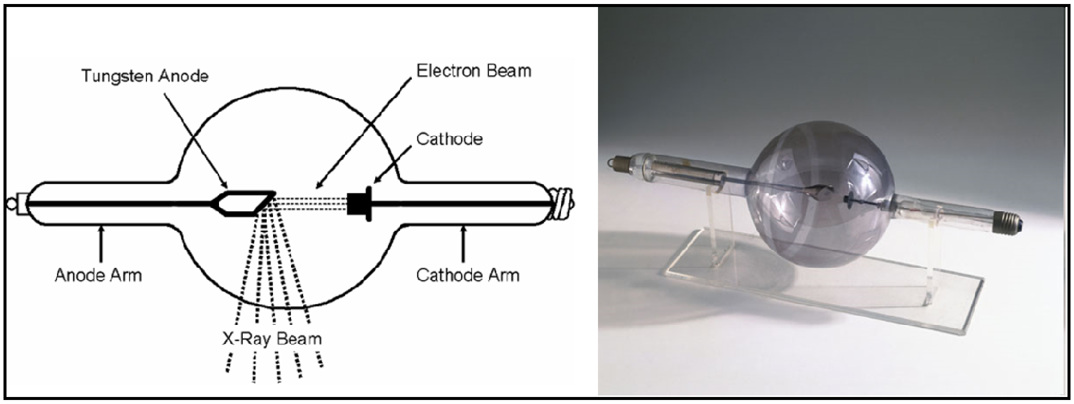

Figure 1.8: (left) schematic representation of a Coolidge tube consisting of a spherical glass bulb, a filament cathode and a tungsten anode. The key advantages of the Coolidge tube were its stability, and the fact that the intensity and energy of the x-rays could be controlled independently (http://www.orau.org /PTP/ collection/ xraytubescoolidge/ coolidgeinformation .htm). (right) Photograph of a Coolidge tube from Science Museum/ Science & Society Picture Library (http://www.science museum.org.uk/images/ I012 /10325841.aspx)]

Conventional x-ray tubes are the most commonly used x-ray source type; however, it has its own limitation. The “hot cathode” requires a heating mechanism and high power consumption which makes the system bulky. Also, the intrinsic heating process for electron emission limits the temporal resolution of the system. High operating temperatures also reduce the lifetime of the tube mainly due to oxidation of the metal filament. In addition, the emitted electrons are randomly distributed in space and have wide energy distribution.

1.2.3 Synchrotron X-Ray Source

Synchrotron radiation is electromagnetic radiation generated by a synchrotron. It is generated by the acceleration of ultrarelativistic (i.e., moving near the speed of light) charged particles through magnetic fields. This may be achieved artificially in synchrotrons or storage rings, or naturally by fast electrons moving through magnetic fields in space. The radiation produced may range over the entire electromagnetic spectrum, from radio waves to infrared light, visible light, ultraviolet light, X-rays, and gamma rays. It is distinguished by its characteristic polarization and spectrum [9].

Synchrotron x-ray sources have many advantages over Conventional x-ray source as very high brightness about hundreds of thousands times higher than conventional x-ray tubes. Also pulsed x-ray radiation with desired temporal resolution (upto nanosecond) can be generated. They have high spatial resolution (can be as small as sub-micron meter or even nanometer). In addition it has large energy range, the radiation covers a wide range of energy and the beam energy is tunable.

Although synchrotron x-rays have the potential to bring a dramatic improvement in the field of science and engineering, generation of synchrotron radiation is not trivial and needs high energy physics facility to accelerate the electrons. The high cost and limited availability of synchrotron facilities restrict its widespread application.

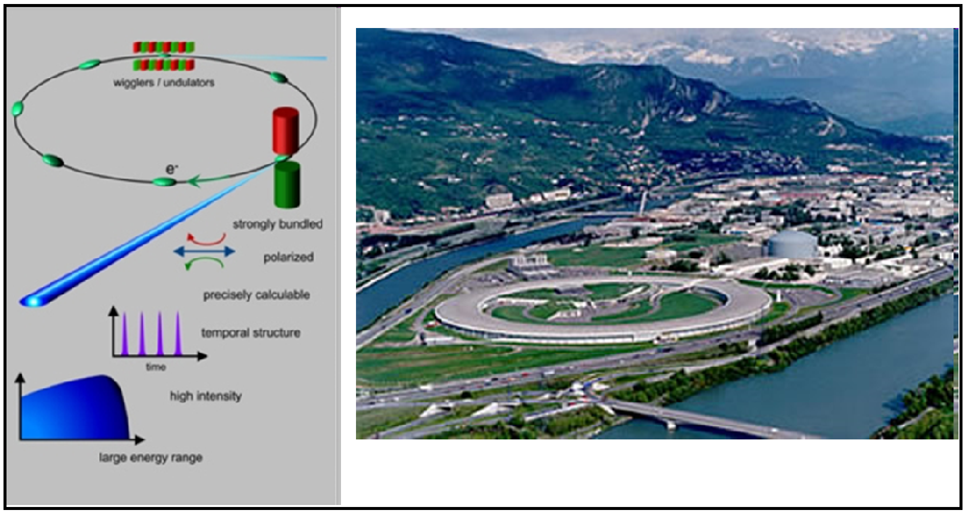

Figure 1.9: (left) Schematics of generation of synchrotron x-ray radiation and its properties.(http://www.physik.uni-kiel.de/kfs/Infos/Quellen/synchrotronradiation.php?Druck =ein). (right) Picture of the ESRF: European Synchrotron Radiation Facility, Grenoble, France Swiss/Norwegian beam lines: SNBL(http://www.ingap.uio.no/research/Methods/In_situ@ SNBL /)

1.3 Carbon Nanotubes as Field Emitters

There has been a tremendous progress in the x-ray technology since its discovery in 1895; however, there has been practically no change in the x-ray generation mechanism as mentioned earlier. In many applications including medical imaging and diagnostics, conventional x-ray sources are just not adequate. There is a dire need for an x-ray source with improved spatial and temporal resolution. A potential solution to this issue might be the newly developed carbon nanotube (CNT) based field emission x-ray source. In the next few sections a brief description of the emission theory will be given followed by an introduction to the field emission x-ray source.

1.3.1 Electron Emission Theory

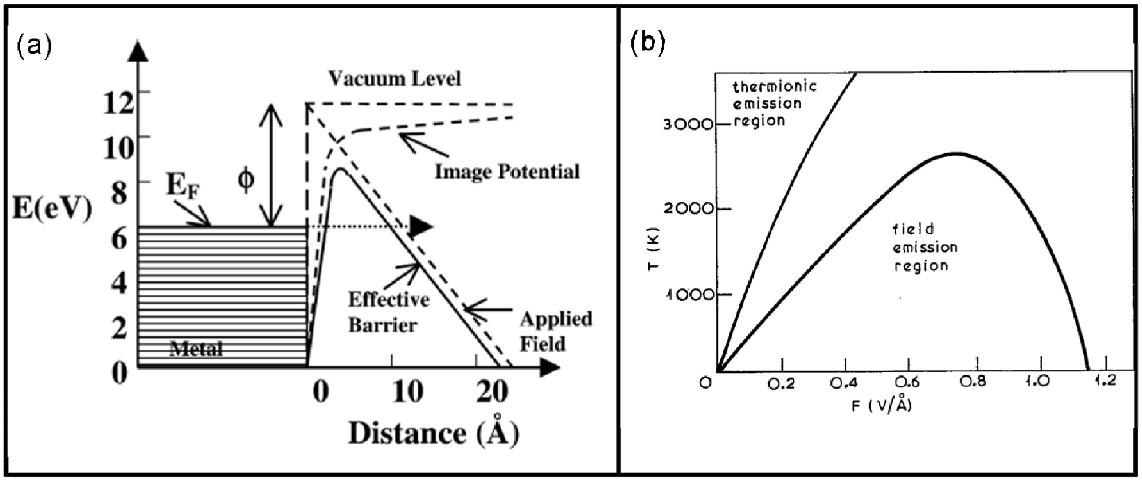

Figure 1.10 : Potential-energy diagram illustrating the effect of an external electric field on the energy barrier for electrons at a metal surface [10,11]

The emission of electrons from a conducting material like a metal follows Fermi-Dirac statistics. Electron emission processes are central to many effects at surfaces and interfaces. In a conducting material (typically metals), at low temperatures the energy of most electrons is lower than the Fermi energy [12]. Due to the surface energy barrier, electrons are bounded inside the metal. Emission of electrons occurs when the electron has sufficient energy to overcome this energy barrier as shown in Figure (1.13(a)). This can be done by either thermal emission or field emission and is described in the following section. The two different regimes of the different emission mechanisms can be seen in Figure (1.10(b)).

Thermionic Emission

Thermionic emission is the emission of electrons from a material when it is heated to high temperatures (typically 1000 – 3000ºC), such that the electrons have enough energy to escape from the Fermi-level to the vacuum level as shown in Figure (1.10). Thermionic emission is a common electron extraction mechanism. A classical example of thermionic emission is the emission of electrons from a hot metal cathode in a vacuum tube. Thermionic emission follows the Richardson-Dushman equation, where T is the metal temperature, ϕ is the work function, and k is the Boltzmann constant.

$$J = 120T^2 e^{-\frac{\phi}{kT}} \left[A/cm^2\right], \text{ where } T \sim 1000\ ^{\circ}\mathrm{C} \qquad \text{Equation 1.1}$$

Thermionic emission is widely used in various applications; however, it has its own disadvantages. Thermionic sources have low energy efficiency due to the high operating temperature that contributes to the energy loss by radiation. Figure (1.11) illustrates the principle of the thermionic emitter. Other limitations include change in shape of the emitter due to the thermal expansion. In addition, out-gassing from these emitters cause vacuum degradation, which results in limited lifetime.

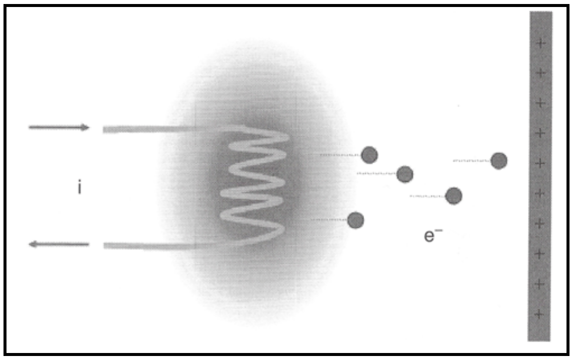

Figure 1.11: Principle of thermionic emitter: a metal is heated high enough to give the free electrons enough energy to overcome the surface potential barrier [13].

Field Emission Theory

Field emission is an alternative mechanism for extraction of electrons without the limitations of thermionic emission since electrons are emitted at room temperature. Field emission is a quantum-mechanical phenomenon in which electrons tunnel through a potential barrier at the surface of a solid (usually metal) when an external electric field is applied. Under the external electric field, the potential barrier shows finite width and therefore is permeable to the electrons. At the same time, the height of the barrier is smaller. The Fowler-Nordheim equation (Equation) describes the field emission mechanism ,

$$I = aV^2 \exp\left(-\frac{b\phi^{1.5}}{\beta V}\right) \qquad \text{Equation 1.2}$$

where I is the emission current, V is the applied voltage, ϕ is the work function and β is the field enhancement factor [14]. The work function is an intrinsic property of the material that cannot be varied and determines the emission characteristics of the material. The field enhancement factor is inversely related to the shape of the emitter: as the radius of the emitter decreases the field enhancement factor increases. Moreover, if the field enhancement factor increases, the field concentration also increases and the effective threshold voltage decreases.

When sharp cathodes are used for field emission, the electric field around the sharp tip is highly enhanced and a macroscopic field of a few V/µm can be sufficient to cause emission as seen in Figure (1.15).

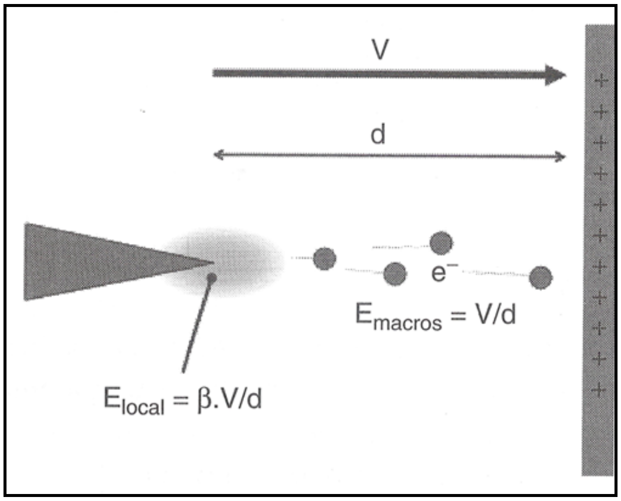

Figure 1.12: Schematic diagram of a field emitter; the electric field around the sharp tip is enhanced to the point where electrons can tunnel through the surface barrier [Error! Bookmark not defined.Error! Bookmark not defined.**].**

1.3.2 Field Emission in Carbon Nanotubes (CNT)

Carbon nanotubes were first observed and reported by Sumio Iijima from byproducts obtained during the synthesis of fullerenes [15]. At that time Iijima observed multiwalled carbon nanotubes (MWNTs) as seen in Figure (1.13). Two years later in 1993, single-wall carbon nanotubes (SWNTs) were synthesized. CNTs are a stable form of carbon consisting of long (>1µm) graphitic cylinders with nano-scale diameters (<50nm) and can be categorized into Single-wall Nanotubes (SWNT), Multi-wall Nanotubes (MWNT) and Double-wall Nanotubes (DWNT). The chemical bonding of nanotubes is composed entirely of sp^2 bonds, similar to those of graphite. This bonding structure, which is stronger than the sp^3 bonds found in diamonds, provides the molecules with their unique strength. Nanotubes naturally align themselves into "ropes" held together by Van der Waals forces [16, 17].

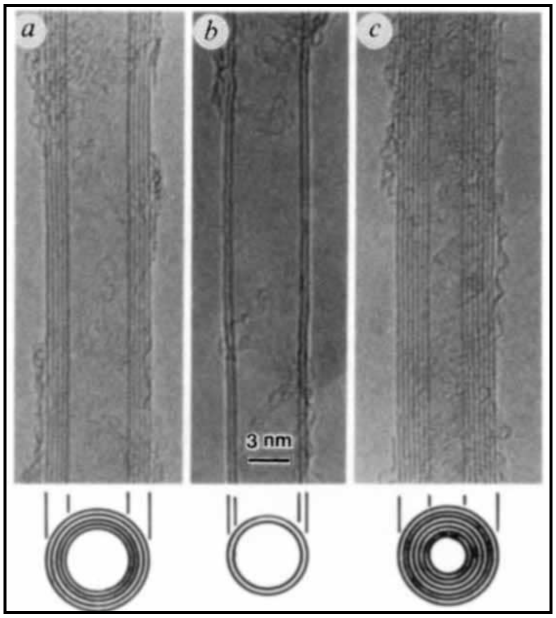

Figure 1.13: Electron micrographs of the early carbon nanotubes. (a) Tube with five graphitic sheets (b) Two-sheet tube (c) seven-sheet tube [15].

CNTs can be synthesized by various techniques such as arc discharge, laser ablation and chemical vapor deposition (CVD). Most of these processes take place in vacuum or with process gases. CVD growth of CNTs can occur in vacuum or at atmospheric pressure. CNT's extraordinary geometric property of high aspect ratio, coupled with their high mechanical strength and chemical stability, makes them excellent electron field emitters. Despite the large work function (~5eV) associated with graphite and nanotubes, high field concentrations can be effectively induced at the sharp nanotube tips that allow electrons to overcome the surface barrier and emit into vacuum at low macroscopic fields.

The small dimensions, high strength, and the remarkable physical properties of CNTs make them a very unique material with very promising applications. Some of the applications are shown in Figure (1.14).

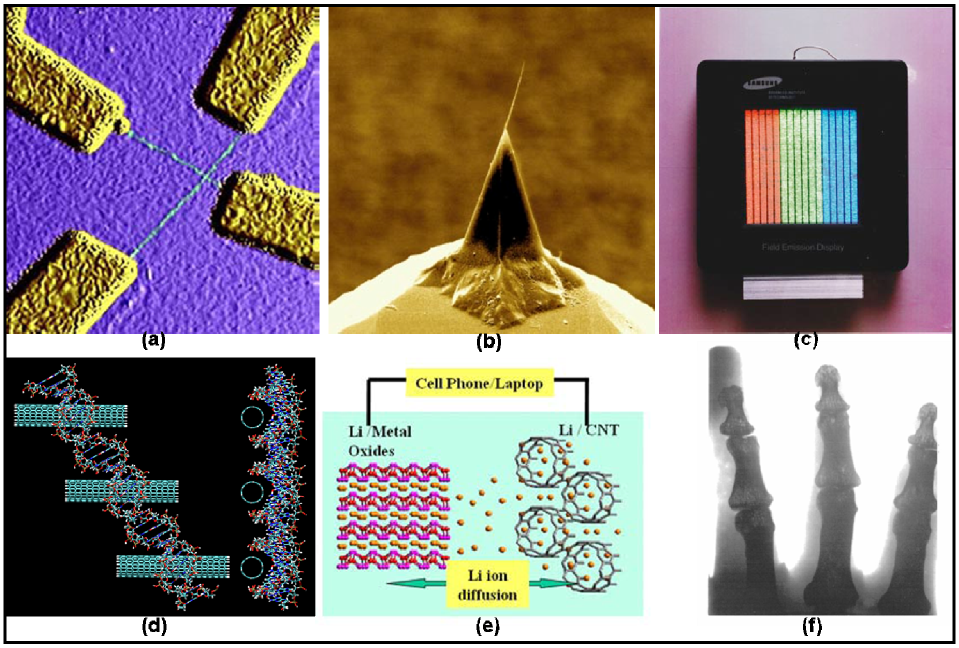

Figure 1.14: (a) An AFM image of a nanotube microelectronic circuit [18] (b) CNT on a cantilever tip (reproduced from http://www.nanoscience.ch/nccr/nanoscience/pictures /gallery_01/gallery_01_03) (c) The emitting image of a fully sealed SWNT-FED[19] (d) DNA interaction with CNTs (reproduced from http://www.seas.harvard.edu/ekaxiras/research/research.html) (e) A CNT based Li ion battery (Courtesy of Soojin Oh) (d) An x-ray image of a humanoid hand using carbon nanotube based field emission x-ray tube[25].

– *Scanning probe microscopy*: the small tip diameter, large aspect ratio, and large young's modulus give the CNT-equipped AFM and SPM tips ability to detect sub-nanometer feature and deep trenches.

– *Nano-electronics*: semiconductor nanotubes can be used for metal-semiconductor (Schottky) diodes, PN junction diodes, and field-effect transistors (FETs), whereas metal nanotubes can be used for single-electron tunneling transistors.

– *Field emission*: the large aspect ratio and unique electrical properties make CNTs the ideal field emitters. Potential applications include vacuum microelectronics, microwave amplifiers, field emission displays, and x-ray tubes.

– *Chemical, physical, and biological sensors*: the small size, large surface to volume ratio, and unique one dimension structure make CNTs the ultimate sensors which can potentially improve sensitivity, lower detection limit, reduce sample amount, and increase detection speed.

- *Composites*: carbon nanotubes enhanced composites are a near-term application and some of them have been commercialized. The examples include conducting polymers, multifunctional polymer composites, conducting metal matrix composites, and higher fracture-strength ceramics.
- *Other applications*: noticeable other applications include integrated circuit manufacturing, catalyst support and adsorbents, storage/intercalation of hydrogen.

1.4 Carbon Nanotube based Field Emission X-ray Source

One of the major breakthroughs in the history of modern vacuum microelectronics was the successful use of field emitters as electron sources. Compared to conventional thermionic sources, field emission from “cold cathodes’ offered some attractive characteristics, including instantaneous response to field variation, resistance to temperature variation and a non-linear, exponential current-voltage relationship. In spite of all the potential, early attempt to produce so called Spindt-type emitters [20, 21] for field emission display and x-ray sources for miniature devices was a big failure. This was primarily due to the inability to maintain high vacuum (10^{-9} Torr or better) and the need of very high extraction field to maintain a reasonable emission current. The sharp etched tips were vulnerable to damage from the high-energy ions created by electron impact ionization which limited their lifetime [22]. Nonetheless, Spindt-type cathodes were deployed in many devices such as microwave amplifiers, high resolution cathode ray tubes, electron microscopy and flash x-ray photography [23].

The invention of microtip field emitter arrays (FEA) renewed efforts for exploring novel cold cathode materials for better and more reliable performance. The search resulted in the emergence of a new class of carbon-based materials which included diamond, diamond-like or amorphous carbon and carbon nanotubes. In the 1970s, investigators had already established the fact that carbon based materials were very stable and reliable field emitters. The 1990s further established the fact that carbon nanotubes with their one dimensional nano-scale structures were attractive field emitters. The nanotubes with aspect ratio greater than 1000 indicated that they were excellent field emitters with low turn-on field and high emission current density. Field emission current of 1μA from SWNTs and current densities as high as 4 A/cm^2 from multiple nanotubes had been observed [22, 24]. This makes CNT field emitters ideal candidates to be incorporated into field emission displays as well as point sources such as an electron gun.

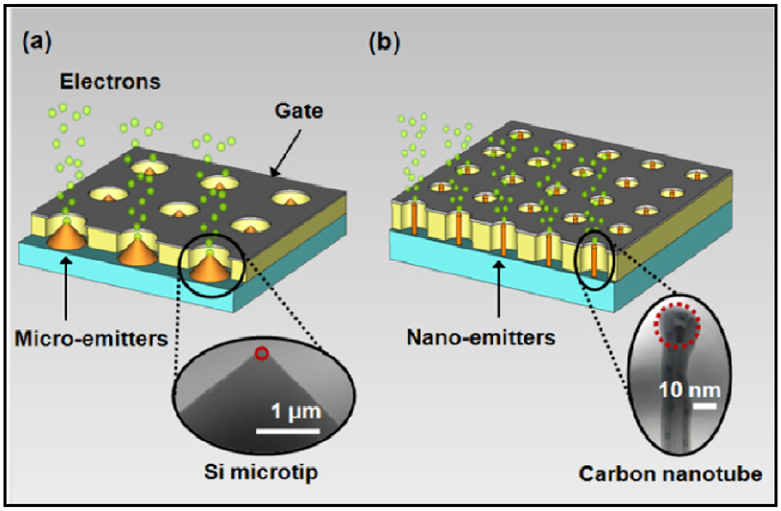

Figure 1.15: Schematic representations of (a) FE microtriodes possessing microtips as emitters, (b) FE nanotriodes possessing low-dimensional nanomaterials as emitters [25].

The new millennium brought the focus on the feasibility of field emission x-ray sources using CNTs across the world. H. Sugie from Nagoya Institute of Technology (NIT), Japan, reported the development of an x-ray tube using aligned CNT field emitters in 2001 [26]. In this particular case they had developed a technique to align CNTs on a cobalt-coated W wire as the field emitter. The CNTs continue to emit electrons with 1.5μA emission current for more than 1 hour at a pressure of 2 × 10-7 Torr. X-ray image of a large scale integrated (LSI) circuit was taken using the field emission x-ray tube, as shown in Figure (1.16 (a)). They claimed that the field emission x-ray tube showed high spatial resolution compared to thermal emission x-ray source.

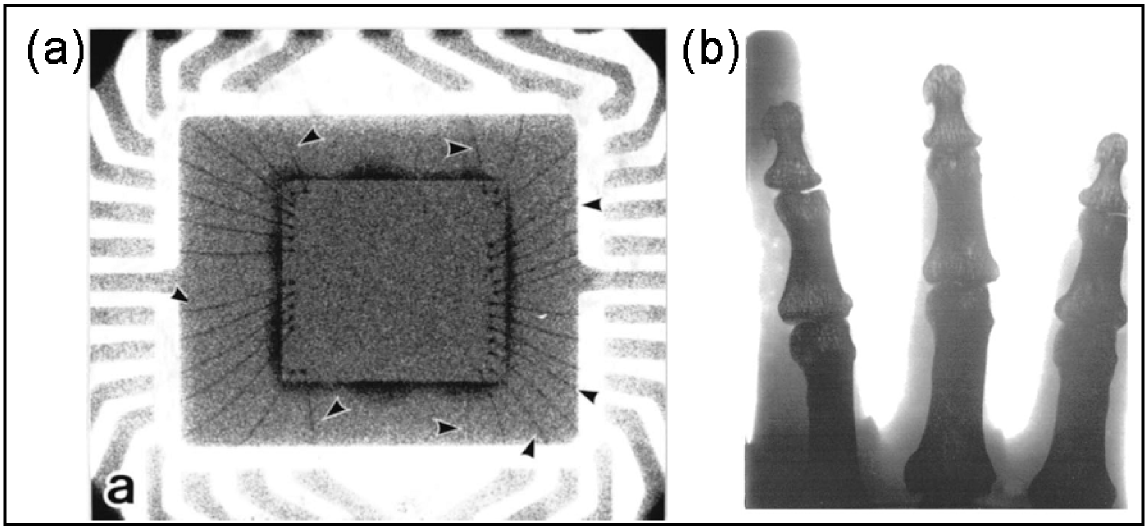

Figure 1.16 (a) X-ray image of a large scale integrated (LSI) circuit taken at Nagoya Institute of Technology, Japan [Error! Bookmark not defined.Error! Bookmark not defined.**].(b)Image of a human hand phantom taken using the x-ray source (developed at UNC, Chapel Hill, US) at 14kVp and 180mAs [**Error! Bookmark not defined.Error! Bookmark not defined.**]. (b) Shows the image of a human hand phantom taken using this x-ray source developed at UNC in 2002 [27].**

The first CNT field emission x-ray source was developed in our group “Zhougroup” in 2002 [27]. Optimization of the CNT film morphology gave a high emission current of 28mA from a 0.2cm^2 area CNT cathode. Figure (1.15(b)) shows the image of a human hand phantom taken using this x-ray source at 14kVp and 180mAs. Details of this x-ray source and its future evolution and improvement will follow in later chapters. Since then commercial vendors developing medical imaging devices have followed suit. Figure (1.17) shows a fixed gantry tomosynthesis system for image-guided radiation therapy based on a CNT field emission x-ray source from Siemens Medical Solutions USA, Inc.

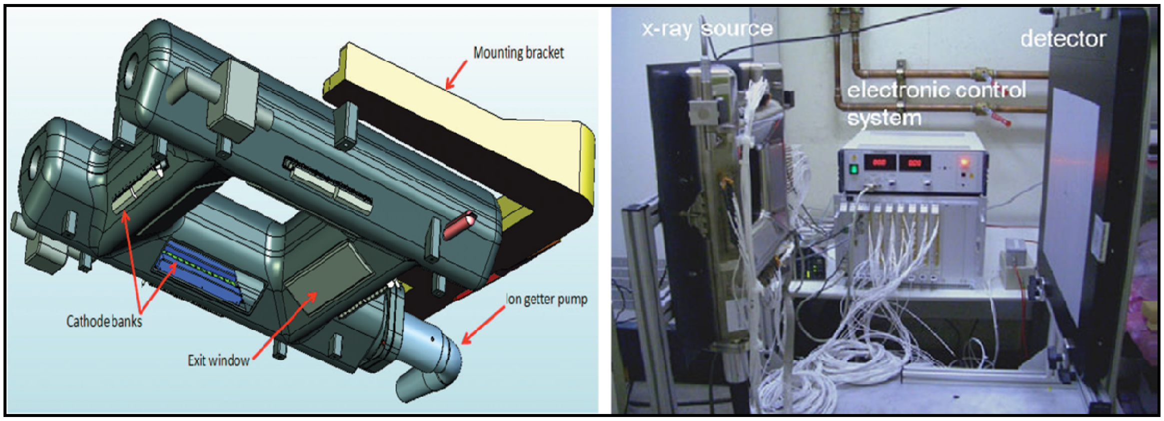

Figure 1.17 : Fixed gantry tomosynthesis system for image-guided radiation therapy based on CNT from Siemens Medical Solutions USA, Inc. Image reproduced from reference [28,29]

1.5 Motivation and Objectives

Advanced x-ray sources with miniature size, high stability, inexpensive with high spatial and temporal resolution has a huge demand in scientific and industrial research. Currently conventional thermionic tubes are the most commonly used x-ray radiation source, however, its intrinsic electron generation mechanism limits its temporal resolution. Synchrotron source satisfies most of the requirements but its limited accessibility, physical size and high cost limits its application.

On the other hand, the CNT field emission x-ray source is a novel technique which can address most of the limitations. With an instantaneous response time, x-ray radiation with programmable waveforms and high temporal resolution can be generated using the field emission cathode, which is desired for time-resolved x-ray radiography [30]. However, an interesting challenge exists for the CNT x-ray technology, the need of lightweight and power efficient miniature x-ray tubes with high spatial resolution. Here we are aiming to resolve some of the aforesaid challenges.

In this dissertation, I will present my research on the development of CNT based field emission x-ray sources with an electrostatic lens as the primary focusing element and to analyze its behavior and performance using electron optics simulation. In order to accurately simulate the electron behavior, an intuitive but simple emission model has been developed to emulate the behavior of CNT field emission in macroscopic cathodes and has been interfaced with the simulation software. The objective of this emission model is to provide a more accurate representation of the field emission mechanism in macroscopic CNT cathodes as the initial particle dynamics play a critical role in shaping the final results.

Reliable computer simulation during design phase is crucial for the performance of the final product. A unique advantage of simulation is the ability to visualize design changes and device performance in short period of time, and different changes can be explored simultaneously. This insight often provides the stimulus necessary for further invention and improvement. In this work, the focus is primarily on the spatial resolution and miniaturization of the x-ray source. In addition, application of spatially distributed CNT based multi-beam x-ray source for medical imaging has been explored.

1.6 Summary

In this chapter an introduction to x-ray imaging has been provided. X-rays have applications in various fields but the primary focus in this research work is on medical imaging devices. This is followed by the basic properties of x-rays. Emphasis has been laid on the electron emission theory and potential alternatives to thermionic x-ray sources. A brief introduction has been given on cold cathodes followed by the excellent field emission properties of carbon nanotube. Development of carbon nanotube based x-ray sources and its current status has been reviewed. Motivation and objectives to design and characterize prototype CNT based field emission x-ray sources have been stated. To achieve this target, development of an electron emission model representing the field emission mechanism has been deemed to be necessary.

References

---

[1] Howard H. Seliger, ‘Wilhelm Conrad Rontgen and the Glimmer of Light”, Physics Today, p, 25-31, 1995.

[2] W.A.Hendrickson, “X-rays in molecular biophysics”, Physics Today, 11: p. 42-48, 1995.

[3] http://blass.com.au/definitions/x-ray%20machine

[4] Martin Stauber and Ralph Müller**,”** Methods in Molecular Biology, Vol. 455: Osteoporosis: Methods and Protocols. Micro-Computed Tomography: A Method for the Non-Destructive Evaluation of the Three-Dimensional Structure of Biological Specimens”, p. 273-292.

[5] http://en.wikipedia.org/wiki/Wilhelm_R%C3%B6ntgen

[6] http://www.lbl.gov/MicroWorlds/ALSTool/EMSpec/EMSpec2.html

[7] Jerry L. Prince and Jonathan M. Links, “Medical Imaging; Signals and Processing”, Pearson Prentice Hall Bioengineering.

[8]http://www.orau.org/PTP/collection/xraytubescoolidge/coolidgeinformation.htm p://www.orau.org/PTP/collection/xraytubescoolidge/coolidgeinformation.htm

[9] http://en.wikipedia.org/wiki/Synchrotron_radiation

[10] Y. Cheng and O. Zhou**,**”Electron field emission from carbon nanotubes”, C.R. Physique 4, 1021-1033, 2003.

[11] A. Modinos, ”Field, Thermionic , and Secondary Electron Emission Spectroscopy”, Plenum Press.

[12] http://www.buzzle.com/editorials/2-12-2005-65657.asp

[13] Meyyappan, M., Carbon Nanotubes: Science and Applications. Boca Raton: CRC Press., 2005.

[14] R. H. Fowler and L. W. Nordheim, Proceedings of the Royal Society of London, Ser. A 119, 173, 1928.

[15] Iijima S,”Helical microtubules of graphitic carbon”, Nature 354(7 November), 1991.

[16] http://www.nanocyl.com/CNT-Expertise-Centre/Carbon-Nanotubes

[17] http://en.wikipedia.org/wiki/Carbon_nanotube

---

[18] P.L. McEuen, Single wall carbon nanotubes. Physics World, p. 31-36, 2000.

[19] W.B. Choi, et al., Fully sealed, high-brightness carbon-nanotube field-emission display. Appl. Phys. Lett., 75: p. 3129, 1999.

[20] C.A. Spindt, et al., “Physical properties of thin-film field emission cathodes with molybdenum cones”, Journal of Applied Physics, p. 5248-5263, 1976.

[21] I. Brodie and C.A. Spindt, “Vacuum Microelectronics” in Advances in Electronics and Electron Physics, 83: p. 1-106, 1992.

[22] Zhu W., Vacuum Microelectronics. New York: John Wiley & Sons, Inc. 2001.

[23] W.P. Dyke and W.W. Dolan, Advances in Electronics and Electron Physics, Vol8, Academic Press: New York, p. 89,1956.

[24] W. Zhu, et al., “Very high current density from carbon nanotube field emitters”, Applied Physics Letters,75(6): p. 873-875,1999.

[25] P Y Chen, T C Cheng, J H Tsai and Y L Shao,” Space charge effects in field emission nanodevices”, Nanotechnology 20. 405202, 2009.

[26] H. Sugie, et al.,”Carbon nanotubes as electron source in an x-ray tube”, Applied Physics Letters, 78: p. 2578, 2001.

[27] G.Z. Yue, et al., “Generation of continuous and pulsed diagnostic imaging x-ray radiation using a carbon-nanotube-based field-emission cathode”, Applied Physics Letters,81(2): p. 355,2002.

[28] Jonathan S. Maltz et al, “Fixed gantry tomosynthesis system for radiation therapy image guidance based on a multiple source x-ray tube with carbon nanotube cathodes”, Med. Phys. 36 (5), p.1624, May 2009.

[29] F. Sprenger , X. Calderon-Colon, Y. Cheng, K. Englestad, J. Lu, J. Maltz, A. Paidi, X. Qian, D. Spronk, S. Sultana, G. Yang, O. Zhou, “Distributed source x-ray tube technology for tomosynthesis imaging”, Proc. of SPIE Vol. 7622, 2010.

[30] Y. Cheng, J. Zhang, Y. Z. Lee, B. Gao, S. Dike, W. Lin, J. P. Lu, O. Zhou, “Dynamic radiography using a carbon-nanotube-based field-emission x-ray source”, Review of Scientific Instruments, Vol. 75,10, October 2004.

Chapter 2 : Electron Optics Simulation for CNT X-Ray Source

2.1 General – Electron Optics

"Electron Optics" deals with the motion of electrons in an electric and/or magnetic field. Its origin can be traced back in the writings of an Irish mathematician, Hamilton who published a series of papers in the Proceedings of the Royal Irish Academy, around 1828. Passing to the purely electrostatic case, in 1913 Coolidge had surrounded the tungsten filament of his x-ray tube with a shield. This presumably acted as a rough focusing arrangement, in addition to keeping the electron charges from accumulating on the glass walls of the tube. However, it was not until 1926 that Busch laid the foundation for the practice of Electron Optics where he showed that a short axially symmetrical magnetic field could act as a lens towards an electron beam. This followed an increased interest in this field. Perhaps one of the classic example of electron optics is the electron microscope developed in 1932 [1,2,3,4,5]as seen in Figure (2.1).

Electron beams can be focused by either a magnetic lens or an electrostatic lens. Here we will mainly discuss electrostatic lens since it is the primary focusing mechanism used in the CNT field emission x-ray (FEX) source. Electrostatic lenses satisfy the general properties of optical lenses. Systems of electrostatic lenses can be designed in the same way as optical lenses, so electrostatic lenses easily magnify or converge the electron trajectories.

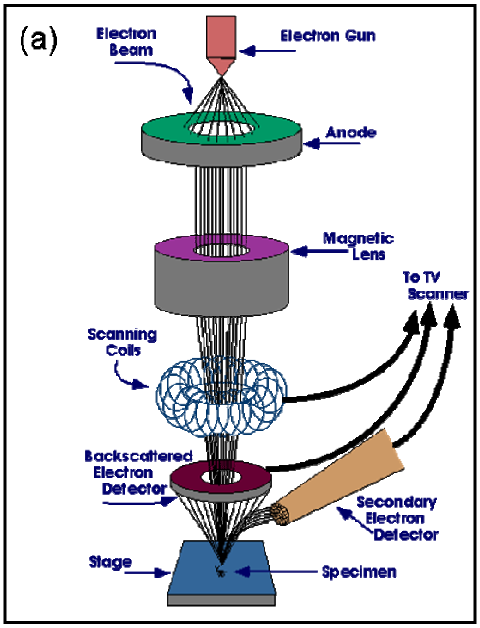

Figure 2.1: (a)Schematic representation of a Scanning Electron Microscope (SEM) where the electron bream makes its way through electromagnetic lenses which focus and direct the beam down towards the sample (Reproduced from http://mse.iastate.edu/microscopy /path2.html).

Typically an electrostatic lenses needs to be operated in a high vacuum environment to avoid unnecessary arcing from the electrodes. Some of their applications include electron microscopes, accelerators and even x-ray sources. However, electrostatic lenses suffer from various aberrations specially "spherical aberration" [6,7,8]. Spherical aberration causes electrons entering the lens parallel to the axis to have a focal length that varies non-linearly with their distance from the axis. This makes it impossible to get a finite focusing point of the electrons but rather a spot with a finite dimension. Limiting the beam to the central portion of the lens will minimize this effect, but, as with coma, changes in image intensity will lead to changes in the achievable spot size. Also, peripheral electrons will be over focused at the anode surface giving an enlarged focal spot [9].

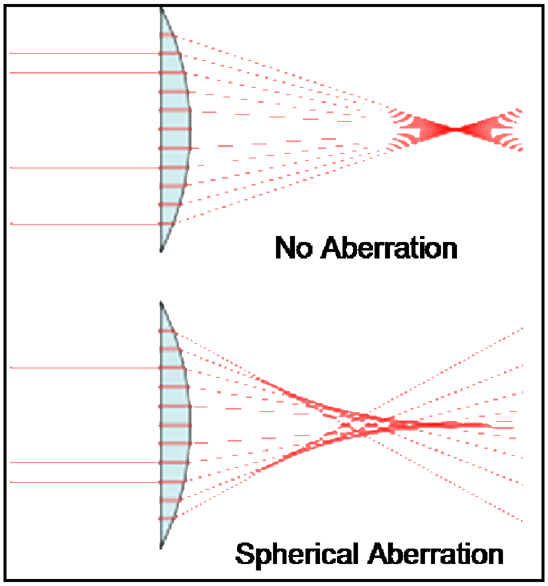

Figure 2.2: Schematic representation of Spherical aberration. Electrons entering the lens parallel to the axis have a focal length that varies non-linearly with their distance from the axis making it impossible to get a finite focusing point (Image reproduced from http://en.wikipedia.org/wiki/ Spherical_aberration).

“Space charge effect” is an electronic aberration caused by the electron beam itself and not by the lens optics. Space charge effect was first observed by Thomas Edison in light bulb filaments. This effect is typically seen in dielectric media (including vacuum) where an excess of electric charge is treated as a continuum of charge distributed over a region rather than distinct point-like charges. This does not happen in a conductive medium as the charge tends to be rapidly neutralized. Space charge effect has adverse effects on electron devices as the mutual repulsion of electrons within the beam can lead to deviations from the expected trajectories. A case of high current density might lead to such a problem. This might cause unwanted complications in the device performance [10].

2.2 Simulation Background - Finite Element Analysis

At an early stage of this research it was recognized that construction of a prototype stationary CNT field emission distributed x-ray source could present unique challenges, particularly with regard to design and assembly. Hence, it was decided that initial investigation would be undertaken using electrostatic simulation tools, to be followed by initial testing in the laboratory for confirmation. For this purpose a finite element (FE) based commercial software called OPERA - 3D from Cobham Technical Services (previously known as Vector Fields) was chosen as the tool to aid the design and study phase. The emphasis of the discussion in this chapter is to get a feel for the software and not how the software works. However, it is important to have a basic appreciation of its operation in order to apply it in an accurate manner. Hence, a brief overview of the simulation tool will be presented in this chapter from a physical rather than a mathematical perspective.

2.2.1 The Modeller

The Geometric Modeller aids the user to define the problem in hand that can be resolved using mathematical solution. The Modeller supplied by Vector Fields has a Graphical User Interface (GUI) that enables the user to describe the problem in a three dimensional space in terms of its geometry, boundary conditions and material properties. Once the description is complete in the form of a model, the information is converted to a database compatible with the solver that will be used to solve the problem.

The Modeller aids in manipulation of defined objects through operations such as transformations and combinations. Basic objects (blocks, cylinders, spheres etc.) can be built at any position in space. They can also be repositioned and modified after creation. Basic objects can also be merged, intersected or subtracted from other objects in space to create more complex geometries. Big complicated systems can be built from basic predefined building blocks. Other more advanced techniques allow the geometry to be modified e.g. by sweeping an existing face or by morphing a cell to a different shape using an algebraic expression.

Model Accuracy Considerations

At the first level, the accuracy of a result or solution is only as good as the description of the problem. This is not trivial when describing a physical problem using simulation tools to expect a fairly accurate result. For example in simulating a field emission source consisting of a cathode, it is extremely important that the emission surface have a very fine mesh size for accurate results. However, the overall model might have large dimensions making it impossible to have a fine mesh throughout the model structure. It is also computationally impossible for ordinary computers to handle such large volumes of data. It is up to the discretion of the user to judge where geometrically large elements will not affect the results significantly, and where it is necessary to refine the mesh to achieve the desired accuracy. In this case, the region near the emission surface needs to be finely discretized to allow proper computation of electron trajectories and of the potential barrier that forms due to space charge. Figure (2.3) shows an instance where the outer volume has a much coarser mesh size (0.5mm) compared to the more sensitive components (0.02mm for the electron extraction grid). The mesh size in the micro-focus x-ray tube configuration ranges between 0.02mm and 3mm.

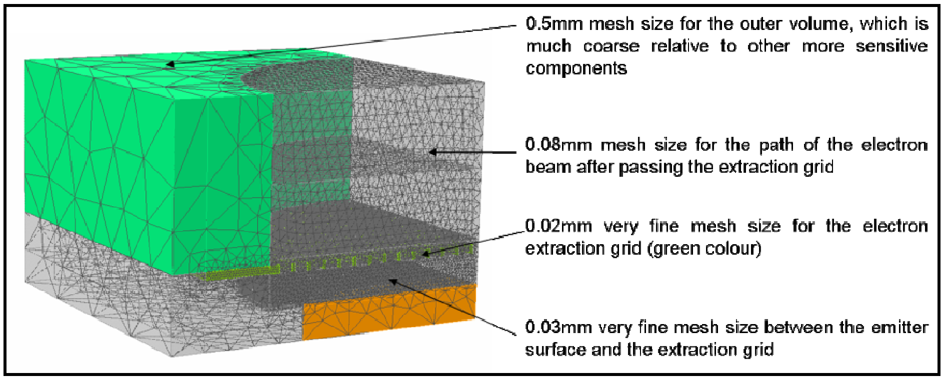

Figure 2.3: Shows an example of varying mesh size of the entire model. The outer volume has a much coarse mesh size compared to some of the sensitive internal components. The accuracy of the result is highly dependent on proper meshing and representation of the problem.

Also, correct boundary volume and conditions pertaining to the specific application is important to achieving reliable solution. The outer boundary volume must be sufficiently large to eliminate any artificial effect on the region of interest. Figure (2.4) shows an instance where the two cases have the same electrode size. However, the background volume, which is varied, has a significant effect on the electric field. The equipotential lines are plotted which are very different. Case1 has a sufficiently large volume and the final result should be independent of any artificial effect. However, Case2 will show very different results and is primarily due to the small boundary volume.

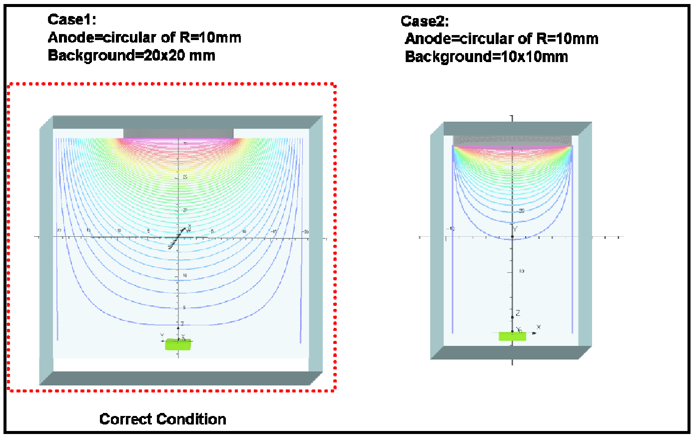

Figure 2.4: Example showing the effect of boundary volume on the region of interest. A sufficiently large volume should be selected to eliminate any artificial effect.

It is also important to make sure that correct boundary conditions have been specified for a particular application. Figure (2.5) is an example showing two different boundary conditions “Tangential Electric” and “Normal Electric” on the mirror face using quarter symmetry (represented by the yellow line). The two cases have very different field distribution. A plot of the potential distribution along the z-direction shows very different curves. “Tangential Electric” has been used for the mirror face in all the simulations using quarter symmetry. Towards the outer boundary there is the chamber or tube at ground potential which takes into account the equipotential condition. Hence, it very important to specify correct boundary conditions to get reliable results.

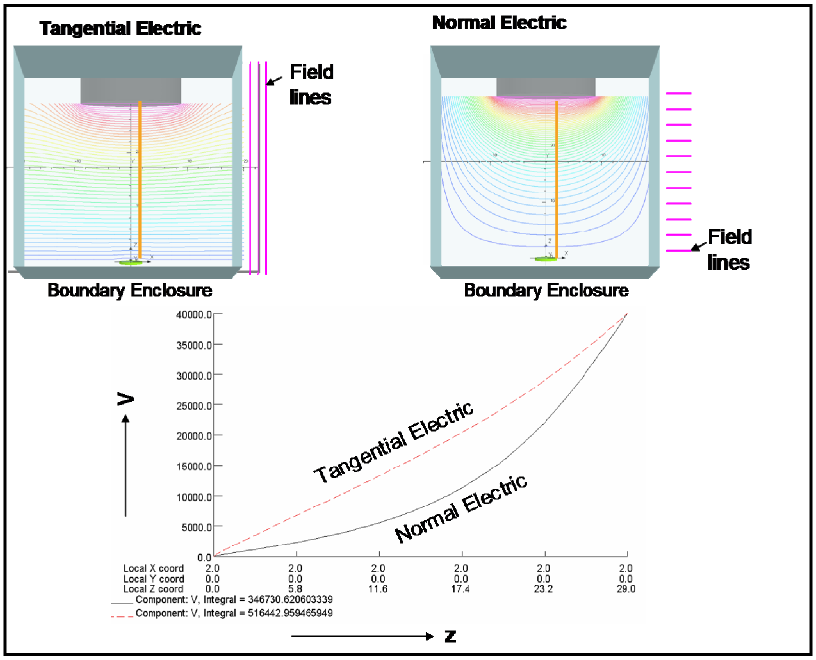

Figure 2.5: A schematic representation of different boundary conditions, “Tangential Electric” and “Normal Electric”. The plot in the bottom demonstrates the difference in the potential distribution along the axial direction for the two conditions.

There are no strict guidelines to creating a finite element model which is guaranteed to represent the physical problem satisfactorily. In such cases the experience of the user is very important to build a fairly accurate but feasible model. Also, critical assessment of the results is very important to determine the accuracy of the solution.

Model Creation

A complex FE model might look intimidating, however built from basic building blocks might not be that complicated. Here is an example of building a planar diode model consisting of a cathode and an anode with air volume separating the two electrodes. First the two electrodes are defined based on their geometric dimensions by specifying their geometric co-ordinates. This also specifies the air volume between the two electrodes as seen in Figure (2.6). The model can be built in two ways: block by block as seen in Figure (2.6(b)) or by using a script file as seen in Figure (2.7).

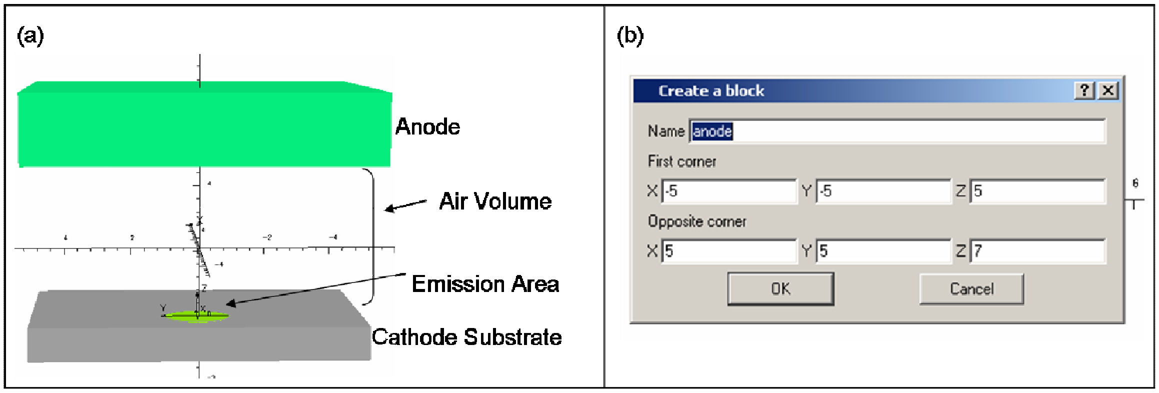

Name anode

First corner

X -5 Y -5 Z 5

Opposite corner

X 5 Y 5 Z 7

Figure 2.6: Example of FE model creation using block-by-block method.

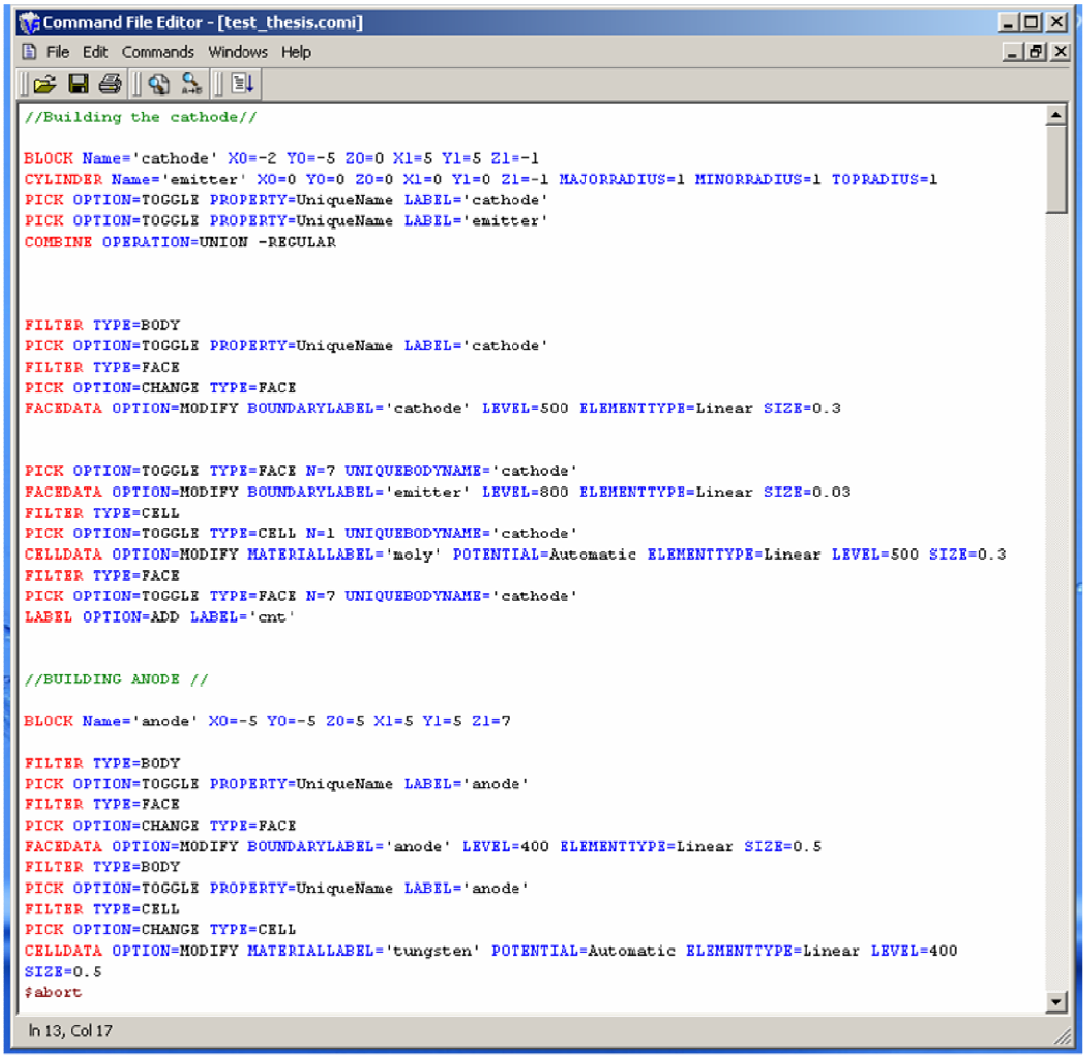

```
//Building the cathode//

BLOCK Name='cathode' X0=-2 Y0=-5 Z0=0 X1=5 Y1=5 Z1=-1
CYLINDER Name='emitter' X0=0 Y0=0 Z0=0 X1=0 Y1=0 Z1=-1 MAJORRADIUS=1 MINORRADIUS=1 TOPRADIUS=1
PICK OPTION=TOGGLE PROPERTY=UniqueName LABEL='cathode'
PICK OPTION=TOGGLE PROPERTY=UniqueName LABEL='emitter'
COMBINE OPERATION=UNION -REGULAR



FILTER TYPE=BODY
PICK OPTION=TOGGLE PROPERTY=UniqueName LABEL='cathode'
FILTER TYPE=FACE
PICK OPTION=CHANGE TYPE=FACE
FACEDATA OPTION=MODIFY BOUNDARYLABEL='cathode' LEVEL=500 ELEMENTTYPE=Linear SIZE=0.3


PICK OPTION=TOGGLE TYPE=FACE N=7 UNIQUEBODYNAME='cathode'
FACEDATA OPTION=MODIFY BOUNDARYLABEL='emitter' LEVEL=800 ELEMENTTYPE=Linear SIZE=0.03
FILTER TYPE=CELL
PICK OPTION=TOGGLE TYPE=CELL N=1 UNIQUEBODYNAME='cathode'
CELLDATA OPTION=MODIFY MATERIALLABEL='moly' POTENTIAL=Automatic ELEMENTTYPE=Linear LEVEL=500 SIZE=0.3
FILTER TYPE=FACE
PICK OPTION=TOGGLE TYPE=FACE N=7 UNIQUEBODYNAME='cathode'
LABEL OPTION=ADD LABEL='cnt'


//BUILDING ANODE //

BLOCK Name='anode' X0=-5 Y0=-5 Z0=5 X1=5 Y1=5 Z1=7

FILTER TYPE=BODY
PICK OPTION=TOGGLE PROPERTY=UniqueName LABEL='anode'
FILTER TYPE=FACE
PICK OPTION=CHANGE TYPE=FACE
FACEDATA OPTION=MODIFY BOUNDARYLABEL='anode' LEVEL=400 ELEMENTTYPE=Linear SIZE=0.5
FILTER TYPE=BODY
PICK OPTION=TOGGLE PROPERTY=UniqueName LABEL='anode'
FILTER TYPE=CELL
PICK OPTION=CHANGE TYPE=CELL
CELLDATA OPTION=MODIFY MATERIALLABEL='tungsten' POTENTIAL=Automatic ELEMENTTYPE=Linear LEVEL=400
SIZE=0.5
$abort
```

Figure 2.7: Example of a script file that can be used to build and run a FE model.

2.2.2 Non-Linear Static Solvers

In this work the solver used is SCALA. It is used to compute electrostatic fields in three dimensions which also take into account the effect of space charge in beams of charged particles. SCALA uses the finite element method to obtain self consistent solutions to the electrostatic Poisson's equation in the presence of charged particles. SCALA needs additional data in the form of description of the emission source. The space charge density included in the Poisson's equation, is found by calculating the trajectories of a set of particles under the influence of an electrostatic field. The particles trajectory is terminated when it encounters a material in the model other than air or when it meets the boundary of the solution domain.

2.2.2.1 *Scala Trajectory Algorithm*

In order to calculate the charged-particle trajectories, SCALA solves the coupled set of differential equations for the coordinates (x, y, z) and normalized (p_x p_y p_z) momenta, where $\sqrt{\left(p_x^2 + p_y^2 + p_z^1\right)} = 1$. From the particle's initial position, the program advances the trajectory by one step. The step size used in this initial calculation is determined by the maximum step length specified by the user or by the minimum size along any of the edges of this initial finite-element (depending on which is smaller).

The error is estimated by comparing the results of the 5th order and 4th order Runge-Kutta methods. If the error is too large for the specified tolerance τ then the step size is halved and the trajectory calculation repeated. This procedure is continued until the errors are consistent with the reduced tolerance $\tau_r = \tau/n^2$, where n is the number of times the step size has been halved. Only when the error estimate is less than the reduced tolerance, the step size is considered complete.

This step size is used throughout the remainder of the trajectory calculation and each step compares the step's error estimate with τ_r. If the error estimate is too large the step size is reduced, and if it is less than 10% of τ_r then it is increased but never beyond the lesser of the element size or the user specified value.

Scala Space Charge Assignment

The total electric field at any point in the finite element mesh, E_T, may be expressed as the sum of the boundary condition contributed due to the voltage boundary conditions specified by the user, E_E, and from the space charge distribution, ρ, due to the presence of the charged particles, E_{SC}. This may be written as $E_T = E_E + E_{SC}$. In close proximity to the emission surface the current density, J, is strongly coupled to E_T, and it is therefore necessary to iteratively determine E_T from J, and hence ρ.

On the first iteration, E_T is simply the value of E_E since no space charge has yet been assigned to the FE mesh. E_T is then used to calculate the current flowing from the emission surface that, because of the absence of any potential barrier associated with the space charge, tends to be very large. After charged particle tracking is complete, the first solution with space charge in it has a large negative E_{SC} (for electrons) value, and this can cause E_T to change sign. This gives rise to an excessive potential barrier near the cathode and, on the next iteration, the cathode current flowing into the mesh is "switched off". If unmodified, this would give rise to sustained oscillatory behavior.

To prevent this oscillatory behavior and to assist in obtaining a convergent solution, an under-relaxation or damping factor, f, can be introduced such that only a fraction of the computed space charge is assigned to the FE mesh on each iteration. The method used by Scala is: $\rho_{assigned} = \rho_{old} + (\rho_{new} - \rho_{old}) * f$, $0 < f \leq 1$. For the first iteration, $\rho_{old} = 0$ [11,12].

Scala Convergence Algorithm

The SCALA solver does not converge on the current but on the potential. The test for solution convergence depends on the relative change of potential found on each mesh nodes in the solution domain and the fields are then evaluated by calculating the derivative of the potential. During the creation of the analysis database, the convergence tolerance can be user specified. However, difficulty arises when an oscillatory state has reached. For example, this can occur when the beam current has been stabilized but the individual particle trajectories are still moving slightly due to slight change in potential at the end of iteration.

Other factors that might also affect convergence is insufficient beamlets from the emission surface, coarse mesh at the emission surface representing inaccurate space charge and field variation and also poorly defined models especially the emission surface.

2.2.2.2 Scala Emission Models

The primary charged particle beam in SCALA can be represented by a variety of emission models. The emission model defines the type of particle and emission characteristics that are required. The type of emission model to be used along with some additional data representing the initial beam dynamics is supplied in a separate file called the emitter file associated with the database file created. It should have the same name as the database file, but the suffix is *.emit*. SCALA includes thermionic, field and plasma emission models. Following are the different models supplied with SCALA to represent field emission models:

<u>Type 4: Fowler Nordheim Field emission</u>

In this type of emission, electrons are extracted by the application of an external electric field near the emission surface. Under the influence of the strong electric field quantum tunneling of electrons occur leading to the extraction of the electrons. In 1928 Fowler and Nordheim derived an equation for this tunneling current

$$J_e = 6.2 \times 10^2 \left(\frac{E_f}{\phi_w} \right)^{\frac{1}{2}} \frac{E^2}{E_f + \phi_w} e^{\frac{-6.84 \times 10^7 \phi_w^{1.5}}{E}}$$ **Equation 2.1**

where J_e is the current density in *Amps/cm2*, E_f is the Fermi energy of electrons in the metal, ϕ and E is the electric field in *Volts/Metre* applied to the metallic surface. The tunneling current therefore depends exponentially on the barrier height to the 3/2 power. The initial velocity of the articles is assumed to be the mean of the thermal velocity Maxwellian distribution.

<u>Type 3 and 20: Specified current and density</u>

The module has two options that allow either a current density and initial particle energy to be specified, or a total current, initial particle position and initial particle velocity to be specified by the user. Emitter type 20 has been used for most of the simulations where the total current, initial particle position and initial particle velocity are specified by the user in the form of an *.emit* file.

2.2.3 The Postprocessor

The postprocessor displays and performs additional analysis of the simulation results generated by the program. Once a model has been solved, Post-Processor facilitates advanced visual representation of the solution domain. It is capable of 3D display, hidden surface removal, perspective views according to the eye position relative to the model, and so on, in addition to numerous 3D surface and histogram representations. Some of the figures and plots in this work has been created using postprocessor and will be discussed individually.

OPERA-3D has been extensively used in this work for design and optimization of CNT field emission x-ray sources. Details of the system design have been described in chapters three and four. Here is a brief introduction to the development of CNT field emission x-ray sources at our group. Some of the challenges and constraints faced during this phase have been mentioned. A critical limitation during the design phase involved inaccurate representation of the CNT field emission mechanism on the emission surface during electron optics simulations. This necessitated a revisit to the field emission process in CNTs and further development of an electron emission model to represent this phenomenon more accurately. Detailed description of the emission model developed will follow in the next few sections.

2.3 Development of CNT based X-Ray Source

The first generation of CNT micro-focus tube developed at the "Zhougroup" comprised of a triode type x-ray tube without any focusing structure. Figure (2.8) is a schematic representation of the x-ray tube comprising of a CNT cathode, a gate mesh for the extraction of the electrons and an anode. However, the simulation results demonstrated that the focal spot at the anode was very large because of the beam divergence caused at the gate mesh. Some of the beams had divergence as large as 30º making it necessary to incorporate a focusing structure to the tube geometry to reduce the FSS. At this point a single focusing electrode was introduced, which achieved a demagnification of 3.3 at 40KV anode potential. This tube design with CNT cathode demonstrated the capability of high temporal resolution with pulsed x-ray radiation in the nanosecond range. It also proved to be a potential tool for small animal imaging. However, the tube design suffered from severe spherical aberration which limited the focal spot size [13,14,15].

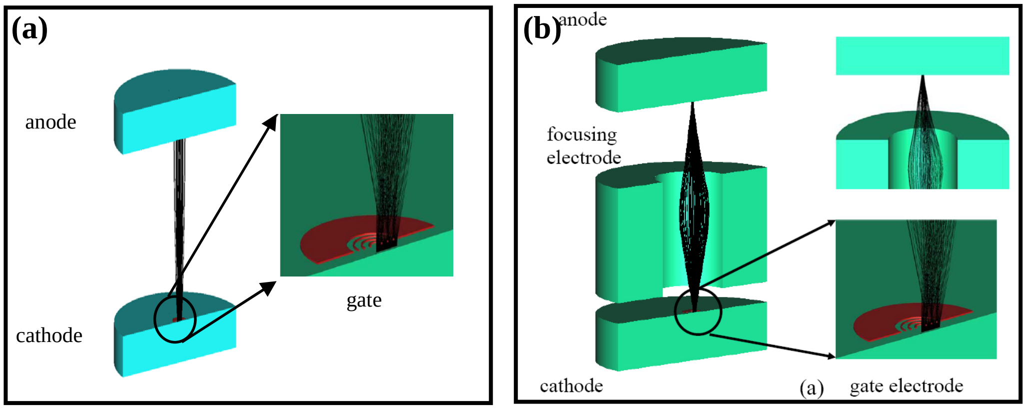

Figure 2.8: : Schematic of the micro focus X-ray tube (a) no focusing structure and (b) single focusing electrode.

Einzel Type Focusing Structure

The second generation CNT field emission x-ray tube came with an electrostatic focusing structure which overcame the limitation of spherical aberration. It consisted of a modified asymmetrical Einzel type lens focusing structure [16,17,18,19,20,21]. Einzel lenses are used in ion optics for focusing, which is achieved by the manipulation of the electric field in the path of the ions. Typically, Einzel type lenses are used for three-electrode lens structures where the first and third electrodes are at the same potential as shown in Figure (2.9). In this particular tube design it is an asymmetrical lens structure where the middle electrode has a truncated conical shape. This helps in pre-focusing the electron beam before reaching the third electrode. All the electrodes have independent controls. The stationary anode has a 12° tilt angle which gives a projection factor of ~4.7 along that axis. The micro-focus x-ray source uses an elliptical CNT cathode where the anode take off angle (θ) matches the ratio of the major axis (D) over the minor axis (d). This gives an isotropic FSS with diameter (d) as illustrated in Figure (2.10) [22].

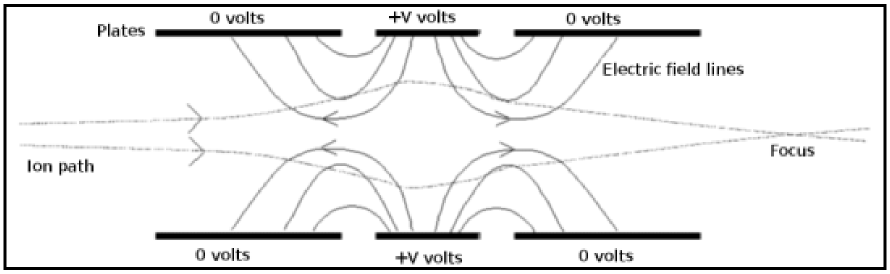

Figure 2.9: Schematic representation of an Einzel type lens. (Reproduced from reference http://en.wikipedia.org/wiki/Einzel_lens)

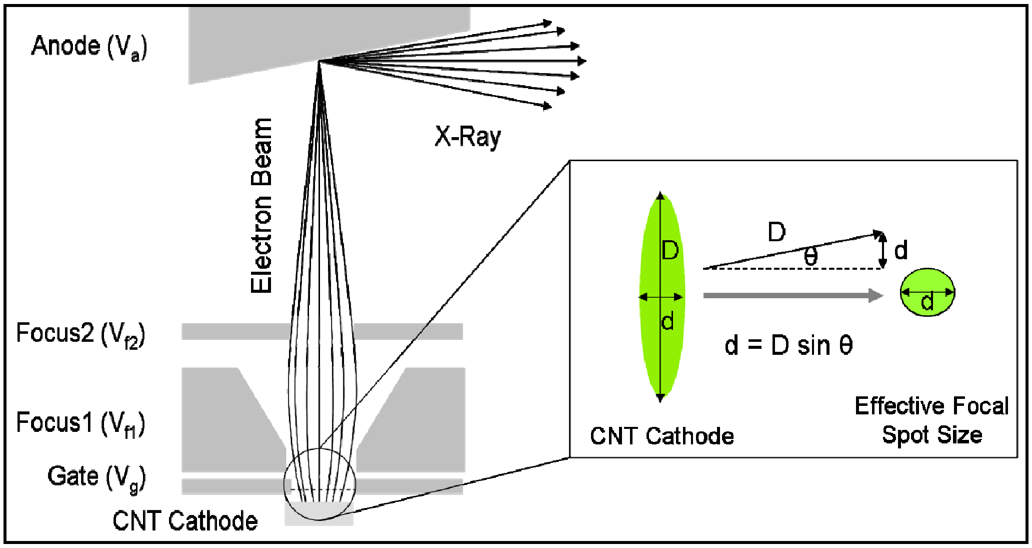

Figure 2.10: Schematic of a CNT based micro focus X-ray source which consists of CNT cathode, gate electrode, focusing electrode and a stationary anode. The inset shows the formation of an isotropic focal spot of an elliptical CNT cathode on the projected plane with the take-of angle of θ.

Before going into the details of the simulation model setup let us look into the requirements of a good x-ray source:

1. <u>High Spatial Resolution</u>: This is primarily determined by the focal spot size (FSS) of the x-ray source. It is the site of bombardment by electrons and emission of x-rays from the anode of an x-ray tube. Typically a current density plot on the anode surface is done, to which a Gaussian curve is fitted. The FSS is then defined as the area within which 80% of the x-ray radiation is generated as shown in Figure (2.11).

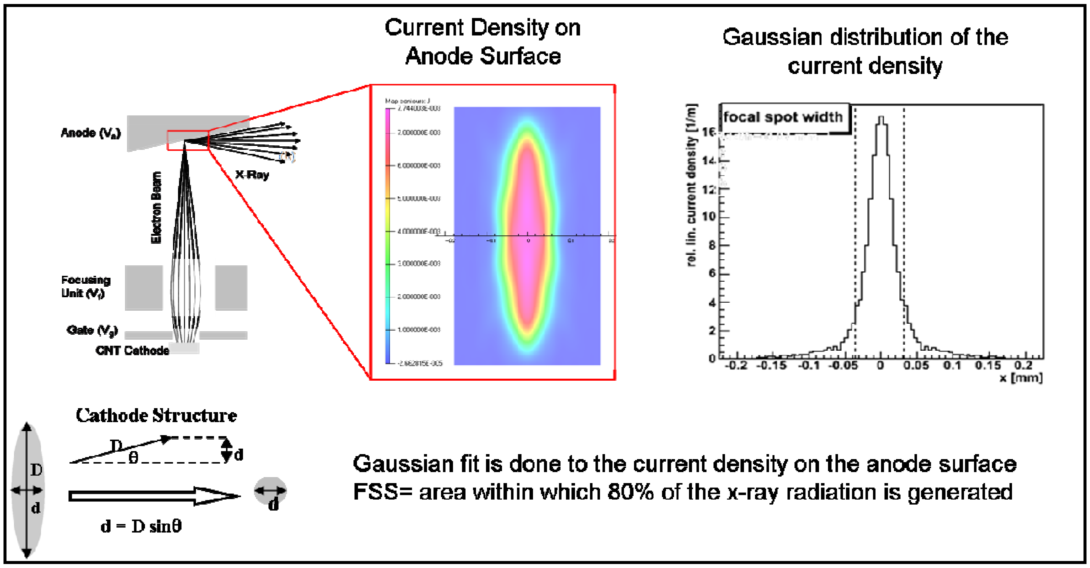

Gaussian fit is done to the current density on the anode surface
FSS= area within which 80% of the x-ray radiation is generated

Figure 2.11: The inset shows a representative plot of current distribution on the anode surface. The plot on the right shows a Gaussian distribution which is used to determine the FSS. This application program is written by Dr. Frank Sprenger.

2. <u>High X-Ray Flux:</u> This is determined by three factors, Large Cathode Size, High Transmission Rate and Good Focusing. A large cathode is going to deliver high current hence delivering high anode current. The transmission rate is the ratio between the Anode current to the Cathode Current. A good focusing structure will focus back more divergent electrons to the anode surface, thus increasing the anode current, hence more x-ray flux.

3. <u>Simple System Design:</u> It is always desirable to have a simple design making it more user friendly. Also, it make sit easy to maintain and troubleshoot.

4. Multiple Emitters: A multiple emitter source array is always desirable because it reduces the time delay between consecutive x-ray exposures due to source positioning. This decreases total scan time, eliminates image deterioration due to focal spot blur and also reduces the system size.

Limitation of the Electron Emission Model

Once the structure of the micro-focus tube was designed, electron optics simulations were performed to study the electron beam profile and do further optimization. For all the initial electrostatic simulations, the emission model used was "***Type 4: Fowler Nordheim Field emission*****".** The simulated focal spot data obtained using this model was much smaller compared to the experimentally measured value. There was no obvious reason where this artificial focusing was coming from in the simulated data. This led to further exploration and review of the model setup and the conditions used. Looking into the details we found out that the accuracy of the results is limited by how well the problem is defined by the user, in this case the emission model used to define the particle characteristics. Clearly "Type 4" emission model was inadequate for this work and we moved to "***Type 20 : Specified current and density***" where the emission model allows the user to specify the initial particle dynamics such as total current, initial particle position and initial particle velocity. This approach seemed to be an efficient way to represent the field emission process in macroscopic CNT cathodes.

2.4 CNT Field Emission Model

For better understanding of this emission model we need some basic idea about the field emission mechanism in carbon nanotubes. We are trying to develop a simple but intuitive emission model with simple fitting parameters that can guide us in predicting the behavior of the electron trajectory of the CNT field emission x-ray source that we will design and develop in this work. To generate this emitter file a MATLAB code has been written and then interfaced with OPERA-3D for electrostatic simulations. A detailed description of the electron emission model and the accuracy of the results have been discussed here.

2.5.1 Uniform Distribution Model

Initial simulations were performed using a simple model to characterize the CNT emission surface. The input parameters are specified as text file as shown in Figure (2.12(e)). The input parameters include a single emission surface with "***Type 4: Fowler Nordheim Field emission***" operating at room temperature 300K. This emission type assumes that the electrons are emitted uniformly across the entire macroscopic cathode with perpendicular orientation to the emission surface. The initial velocity is assumed to be the mean of the thermal velocity Maxwellian distribution. Other input data include work function and the field enhancement factor of the emitter material as shown in Figure (2.12). The field enhancement factor can be used as a scaling factor that allows the user to simply modify the emission model without re-specifying all the emission surface parameters. The default value is 1.0 if not specified. In this particular work the field enhancement factor has been adjusted to achieve the required cathode current (typically ~1mA for the micro-focus FEX).

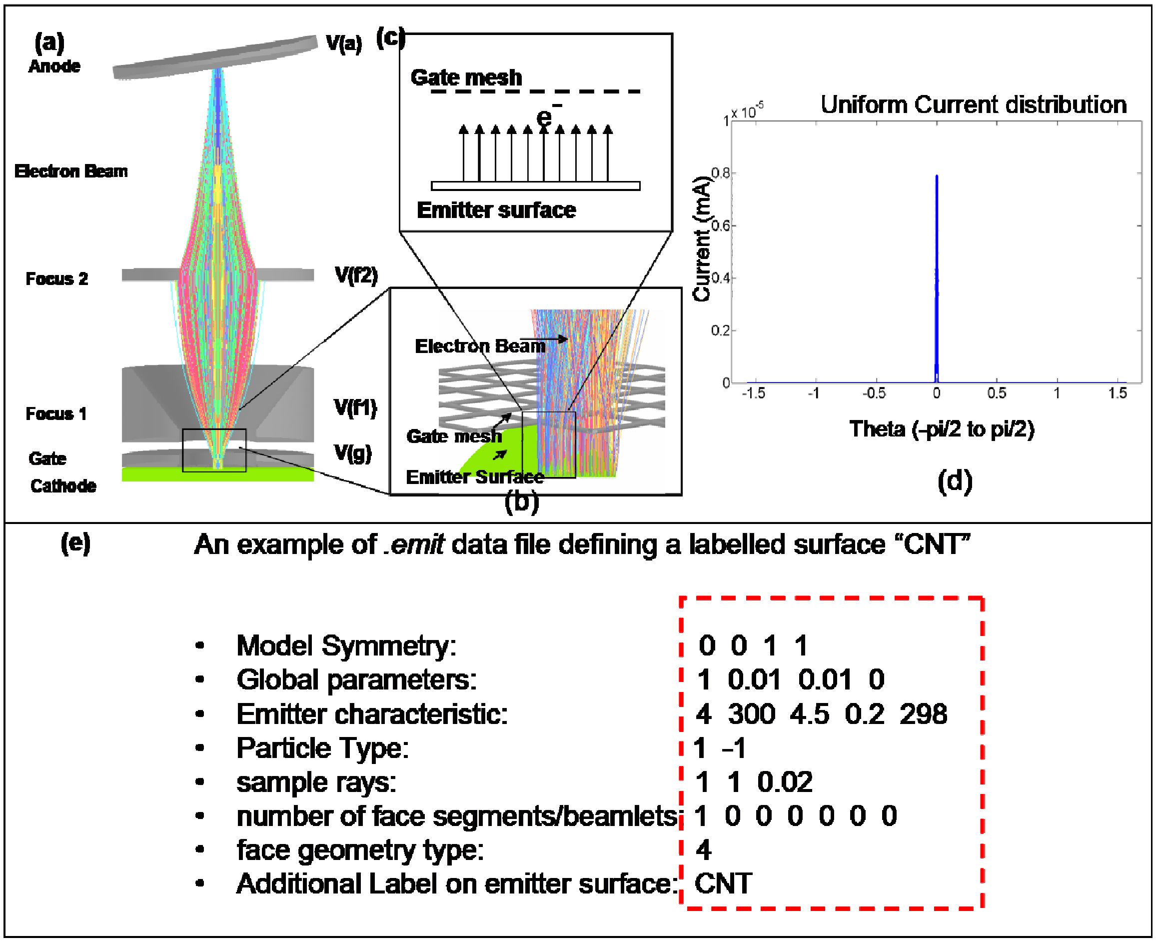

An example of *.emit* data file defining a labelled surface "CNT"

Model Symmetry:	0 0 1 1
Global parameters:	1 0.01 0.01 0
Emitter characteristic:	4 300 4.5 0.2 298
Particle Type:	1 -1
sample rays:	1 1 0.02
number of face segments/beamlets:	1 0 0 0 0 0 0
face geometry type:	4
Additional Label on emitter surface:	CNT

Figure 2.12: (a) Schematic representation of the micro-focus x-ray tube with the electron beam trajectory. (b) Shows the arrangement of the gate mesh on top of the CNT cathode for extraction of electrons. (c) Schematics of the electrons being emitted normal to the emission surface with no divergence and the current is strongly forward biased as shown in (d). (e) Example of an emitter file for Type4 emission model.

Using this "Uniform Distribution" model to characterize the emission surface, electron optics simulations were conducted in a micro-focus tube geometry. Figure (2.13(a)) shows the plot of the FSS as a function of Focus2 voltage. The simulated results were very promising with the potential to achieve a very small focal spot. However, when the experimental result was compared with the simulated data, the two curves exhibited huge discrepancy. Not only did the simulated FSS predict very different absolute values, its dependence on the varying Focus2 voltage was quantitatively different. While the simulated data showed a negative linear trend, the experimental measurements showed a parabolic curve. Furthermore, the transmission rate at the anode was much higher compared to the experimental values (Figure (2.13 (b))). These results suggest that just the tube geometry was not sufficient to get reliable simulation results. An accurate representation of the initial particle dynamics played a critical role in shaping the final results. Hence it became necessary to develop an electron emission model which accurately characterizes the field emission phenomenon in macroscopic CNT cathodes. A detailed description of the model is given in the next section.

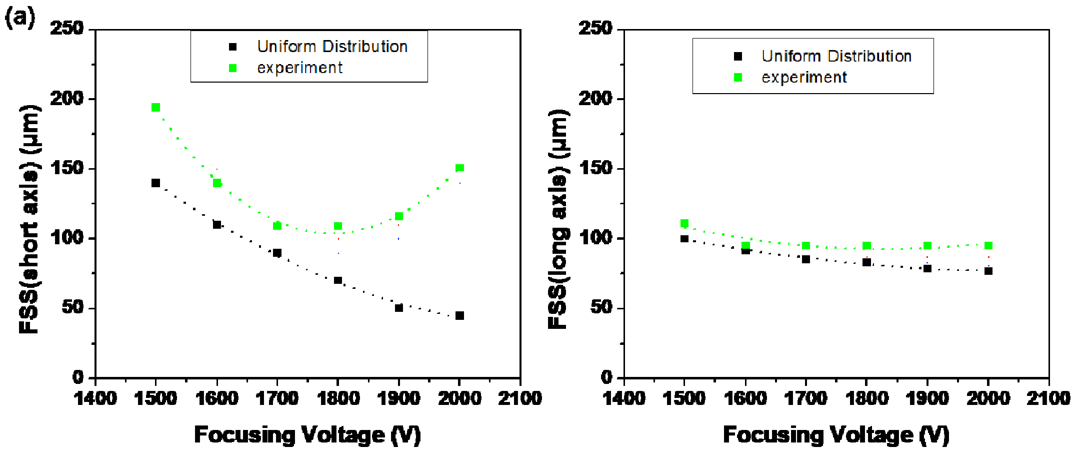

(b)

Transmission	Uniform Distribution	Experiment
Gate	68.8	69.0%
Anode	62.4	50.0%

Figure 2.13: (a) Plot of the FSS as a function of the Focus2 Voltage along the two axes. The Simulated data and experimentally measured data exhibit huge discrepancy. (b) Summary of transmission at gate and anode. The conditions for this setup are 40KV anode potential, 1260 gate potential and 900V Focus1 voltage. A cathode of 2.35x0.5mm was used.

2.5.2 Random Distribution Model

Since the “Uniform Distribution” model proved to be inadequate to define the initial particle dynamics a new model has been developed which takes into account the random distribution of the CNTs on the emission surface and their associated variation of field enhancement factor. The model has three main parts as follows:

- Emitter Position,
- Number of Emitters,
- Current Distribution, and
- Velocity Distribution.

2.5.2.1 Assignment of Emitter Positions

In an attempt to keep the model simple, no artificial structures emulating individual CNT emitter have been included on the emission surface. It is a 2D plane with each particle site being randomly selected. Also, no attempt has been made to associate the position with a particular particle direction or velocity.

An elliptical shape with the CNT cathode dimension has been specified as the emission surface area. Points on the elliptical surface are selected by setting X and Y to be equal to the major and minor axis of the ellipse and then multiplying it with the random numbers generated using “`rand`” function in MATLAB. The `rand` function generates arrays of random numbers whose elements are uniformly distributed in the interval (`0`,`1`). A check is then done to ensure that the point lies within the specified ellipse. If this is not the case, both values are discarded and a new pair of coordinates is selected. This process continues until the position requirement is satisfied. The Z coordinate is specified according to the position of the emission surface in the model (refer Figure (2.14(a))).

2.5.2.2 Number of Emitters

To have enough sampling of the data up to 10,000 emitter sites are chosen randomly over the emitter surface. Increasing emitter sites above 10,000 has no impact on simulation results as can be seen in Figure (2.14(b)).

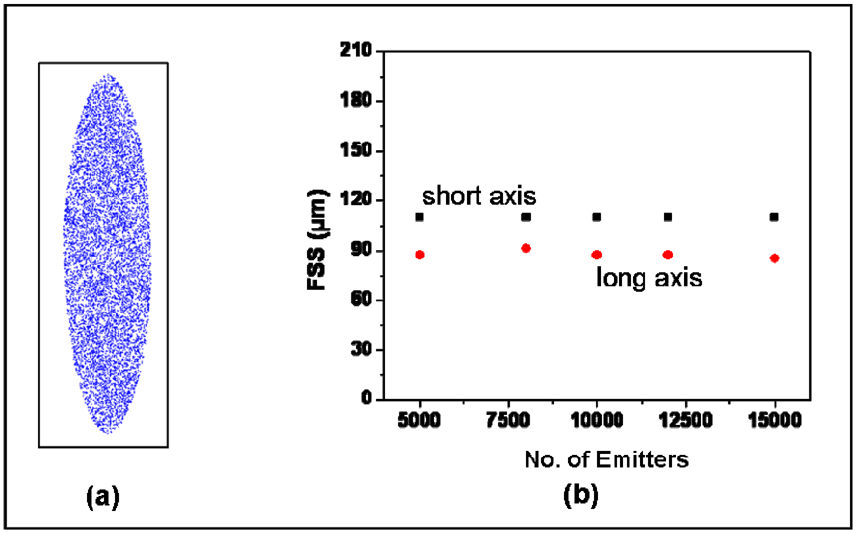

Figure 2.14: (a) Schematic representation of an elliptical emission surface with ransom emission sites. (b)Plot of FSS as a function of No. of emitters . The result suggests that 10,000 emission sites provide sufficient sampling of the data.

2.5.2.3 Assignment of Current Distribution

The assumption of uniform emission from all emission sites at an angle normal to the emission surface clearly oversimplifies the physics of the CNT field emitter. As one can see from the SEM picture of an activated cathode (Figure (2.15(a))), the CNTs are randomly distributed on the cathode surface with different orientation with a fraction of them aligned preferentially perpendicular to the cathode surface due to simple statistical distribution. On application of an external electric field, a fraction of these aligned CNTs start to field emit along with a second group that comes from field induced alignment. The current emitted by each nanotube is different and is a function of its length and the local field experienced by it.

In reality CNTs have different lengths, hence different field enhancement factor and depending on their orientation, individual emitters experience very different local electric field even though the same field is applied between the gate and the entire cathode surface (Figure (2.15(b)). As the emission current is exponentially dependent on the field enhancement factor from the F-N equation, it is incorrect to assume there is uniform emission. Hence a better representation of the field emission process over a large emission area should incorporate the random CNT orientation and the associated variation in the local field enhancement factor.

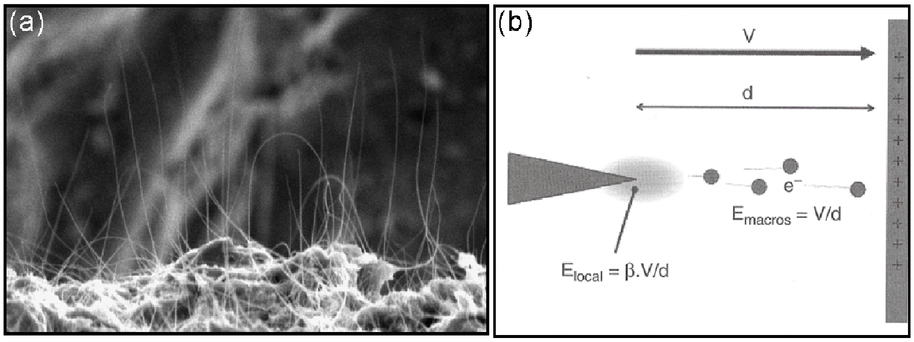

Figure 2.15: (a) SEM image of CNTs on a cathode substrate. (b) Field emission mechanism where the local electric field at the emitter tip is much higher compared to the macroscopic electric field [23].

Electron field emission from a metal surface is a quantum tunneling process which has been well studied. The emission current is determined by the Fowler–Nordheim (F–N) equation [24]:

$$I = A\frac{1.5\times10^{-6}}{\phi}\left(\frac{V}{d}\right)^2\beta^2\exp\left(\frac{10.4}{\sqrt{\phi}}\right)\exp\left(-\frac{6.44\times10^9\phi^{1.5}d}{\beta V}\right) \qquad \text{Equation: 2.2}$$

where, I, V, ϕ, and β are the emission current, applied voltage, work function, and field enhancement factor respectively. d is the distance between the cathode and the gate mesh over which the gate voltage V is applied. Though the original F-N equation was derived for macroscopic surfaces, it has been used successfully to describe the field emission of both macroscopic CNT cathodes and individual CNTs [25]. Therefore the total current in a macroscopic CNT emission surface with *n* emitters can be represented as:

$$I_{tot} = \sum_{i=1}^{n} A \frac{1.5\times10^{-6}}{\phi}\left(\frac{V}{d}\right)^{2} \beta_{i}^{2} \exp\left(\frac{10.4}{\sqrt{\phi}}\right) \exp\left(-\frac{6.44\times10^{9}\,\phi^{1.5} d}{\beta_{i} V}\right) \qquad \textbf{Equation 2.3}$$

The work function for CNT is known to be around 5eV [26,27]. For an individual nanotube along the electric field direction the field enhancement factor β is proportional to the aspect ratio (length/diameter) which can range from 100 to 10,000 depending on the size and the length of the nanotube.

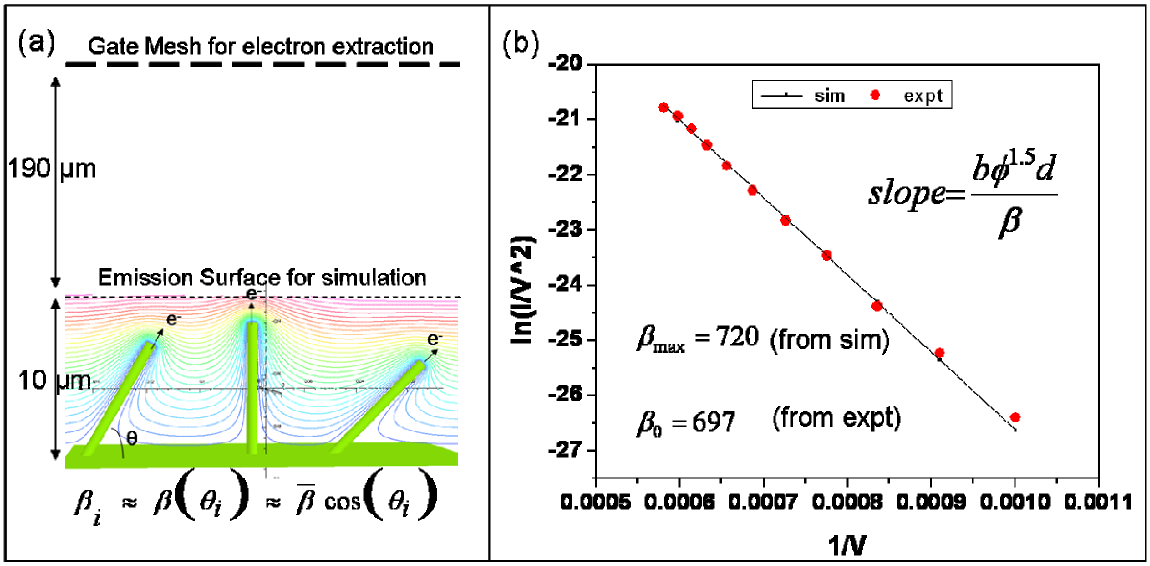

Figure 2.16: (a) Schematic representation of the emission surface with CNTs aligned at different angle. A high field concentration near the tips depict that electrons from the tips will be emitted along the field direction. Hence, it is fair to assume that the electrons will be emitted with an angle equal to the CNT orientation angle. (b) Plot of ln(I/V^2) vs (1/V) from the IV characterization of a 2.35x0.5mm cathode. The max. field enhancement factor can be determined from the slope of the curve.

We have already discussed how the individual CNT's are randomly oriented across the macroscopic emission surface and a small fraction of these start to field emit on application of an external electric field. A schematic representation of this process has been shown in Figure (2.16(a)) where the CNTs are oriented at different angles. We also see that there is a high field concentration near the tips implying that the electrons emitted from the tips will be in the field direction. In other words the electrons will have a divergence angle equal to the CNT orientation angle. Hence, it is fair to assume that an individual emitter oriented with polar angle θ, to the leading order approximation its field enhancement factor will be proportion to cosθ as follows:

$$\beta_i \approx \beta(\theta_i) \approx \beta_{\max} \cos(\theta_i)$$ **Equation 2.4**

where $\beta_{\max}$ is the field enhancement factor across the macroscopic cathode.

To confirm this assumption an F-N plot for a particular cathode size for a given experimental setup was generated using Equation 2.3. From the slope of this plot $\beta_{\max}$ was derived to be 720. This particular $\beta_{\max}$ was selected because this set of data fit well with the measured F-N plot for this particular setup as shown in Figure (2.16(b)). Now the average field enhancement factor ($\overline{\beta}$) can be derived from the $\beta_{\max}$ using the following equation:

$$\overline{\beta} = \frac{1}{\theta_{\max}} \int_0^{\theta_{\max}} \beta_{\max} Cos\theta.d\theta = \frac{1}{\theta_{\max}} \beta_{\max} Sin\theta_{\max}$$ **Equation 2.5**

The $\overline{\beta}$ will be very close to the β_0 value derived from the slope of the F-N plot of the experimentally measured data which is 697 for this particular cathode (refer Figure (2.16(b))). β_0 will vary depending on the cathode performance and the experimental setup. The $\theta_{\max}$ does indicate some kind of forward biasing and is limited by the divergence angle (refer Figure (2.17)). It means the electrons with small divergence contribute significantly to the total emission current.

From our experimental characterization of seven different cathodes, β_0 was determined to be 1018 (at V/d=8V/μm). Therefore the total current in a cathode can be represented as:

$$I_{tot} = \sum_{i=1}^{10,000} A \frac{1.5\times10^{-6}}{\phi}\left(\frac{V}{d}\right)^2 \exp\left(\frac{10.4}{\sqrt{\phi}}\right)\beta_i{}^2 \exp\left(-\frac{6.44\times10^9 \phi^{1.5} d}{\beta_i V}\right) \qquad \textbf{Equation 2.6}$$

where $\alpha = \dfrac{b\phi^{1.5} d}{\beta_{\max} V}$ and ϕ =4.9eV. Depending on the value of α, the emitting current can be a very sensitive function of the orientation angle θ of the CNT relative to the applied field direction. In the case of large α, the current is strongly forward biased, only those CNTs oriented close to the z direction contribute significantly to the total emission current. For very small α, emission is uniform across the emission surface. From the cathode characteristics α has been deduced to be 8.6 using β=1018 (previously derived) at an applied electric field of V/d=8V/um. The current distribution as a function of orientation for this value of α is shown in Figure (2.16). As can be seen, the distribution is in between the extreme limits of uniform emission among all angles and that of singular distribution along the z-direction. The emitting current is normalized such that the total cathode current is the same as the experimental values (typically ~1mA for the micro-focus FEX). In this model the current distribution has been empirically derived at a microscopic scale. However, the output has been used as input data for simulations at a macroscopic level.

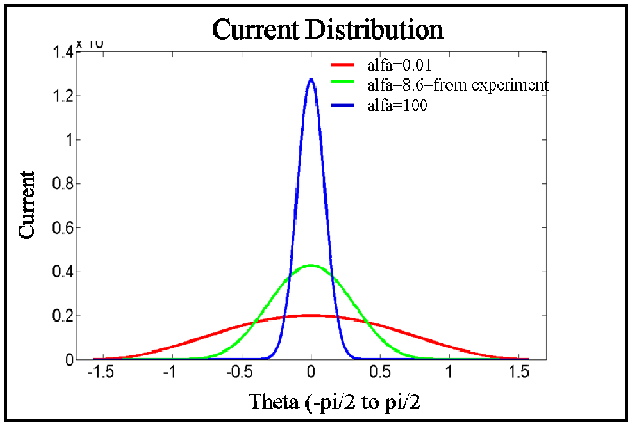

Figure 2.17: Plot of current as a function of angle theta. The current distribution is very different with different values of α.

2.5.2.4 Assignment of Particle Velocity

To fully characterize the initial particle dynamics in the emission model we need to specify velocity distribution of the particles in addition to current distribution. The initial velocity is determined using the equation:

$$KE = \frac{1}{2}mv^2$$

Equation 2.7

where KE is the kinetic energy, m is the electron mass and v is the initial velocity. Once the average velocity is deduced its components can be calculated by taking into account the angular emission distribution. One way of doing this is to randomly select a pair of angles

(ψ, φ) where $0 \leq \psi \leq 90^o$ and $0 \leq \varphi \leq 180^o$, such that the surface of a hemisphere may be described. An implicit assumption in this is that electrons are only released in a forward direction, away from the cathode surface. A standard spherical to Cartesian conversion may be used to transform from (v, ψ, φ) to (V_X, V_Y, V_Z) as follows:

$V_X = V\sin(\psi)\cos(\varphi)$,

$V_Y = V\sin(\psi)\sin(\varphi)$,

$V_Z = V\cos(\psi)$.

However to deduce the velocity we need to find an average KE across the macroscopic CNT cathode. Assuming an average emitter length of 10μm a rough estimate can be made. If the extraction field is 1V/μm then the KE = 10eV, and if the field is 10V/μm then KE =100eV. This is a wide range; nonetheless its effect on the FSS and transmission rate has been studied. Figure (2.16 (a)) shows a plot of a focal spot area as a function of varying "α" where different lines represent different KE. The FSS (area) ranges between 0.005mm^2 and 0.008mm^2.

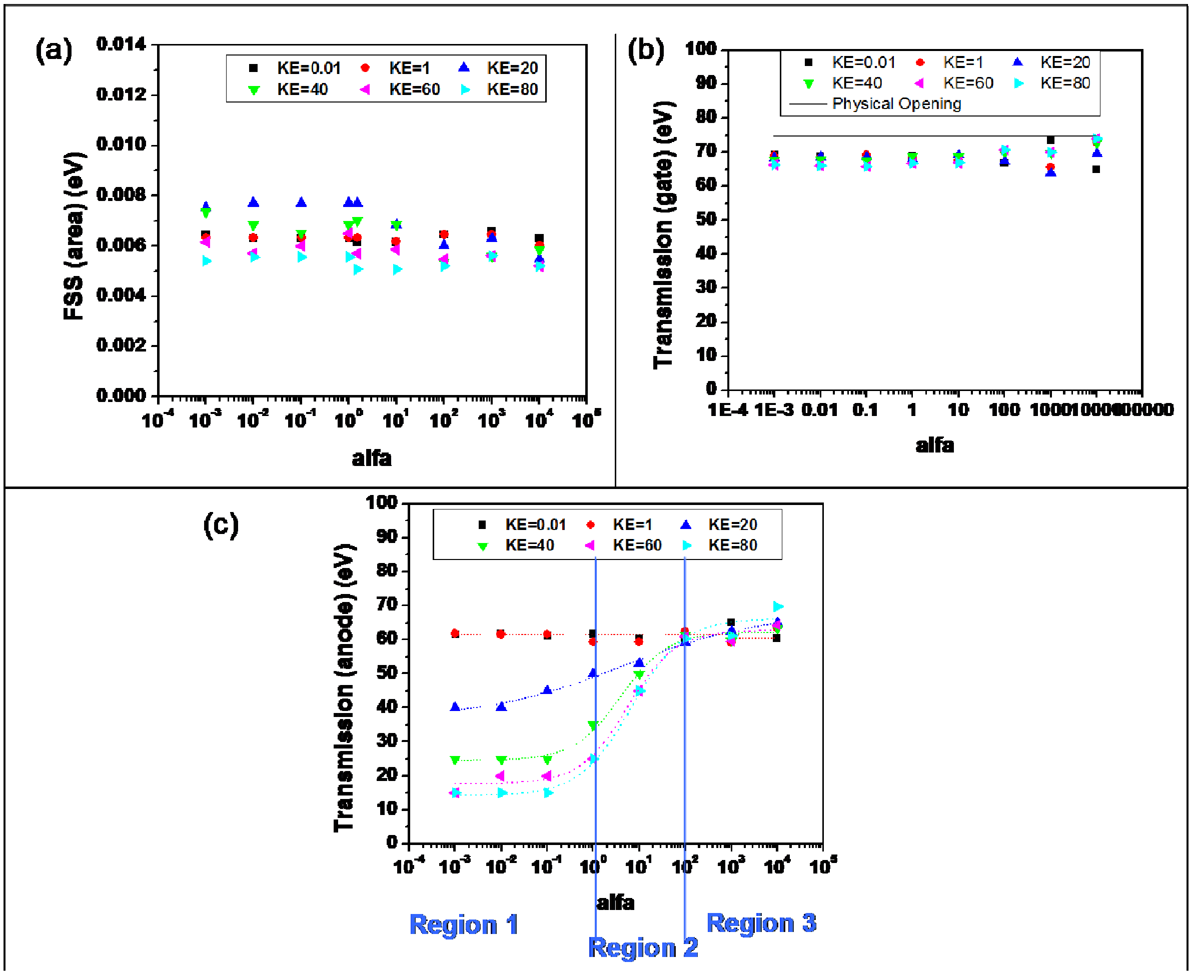

Figure 2.18: (a) Plot of FSS (area) as a function of α for different KE. It ranges between 0.005mm^2 and 0.008mm^2. (b) and (c) is the plot of the transmission rate for different KE.

The effect on transmission rate as a function of “α” has also been studied. Figure (2.16) (b) and (c) shows a plot of the same and also its dependence on KE. From the plot we see that the gate transmission is weakly dependent on KE and “α”. It is very close to the physical opening of the gate mesh which is 75%. However the anode transmission is very sensitive to the KE as well as “α”. For ease of understanding the range of “α” can be broadly divided into three regions primarily based on the transmission. Region3 where “α” ranges between 100 and high primarily means a current distribution which is strongly forward biased. It also means that the “virtual emitter” has a small angular divergence; hence, the emitted electrons can easily be focused. This means majority of the electrons pass through the focusing structure irrespective of the KE and reach the anode exhibiting high anode transmission.

At $\alpha \leq 1$ (Region1), we see a dramatic drop in transmission rate with increasing KE. At low “α” the current distribution is uniform with the electrons having a large angular divergence (0 and 90°). At low KE it is easy to focus back the electrons, however with increasing KE the high angular velocity makes it challenging to focus back the electrons. More electrons are blocked by the focusing structure and the anode transmission drops drastically. Region2 ($1 \leq \alpha < 100$) exhibits a similar trend as Region1 with moderate drop in transmission rate with increasing KE. This is an intermediate region between the two extreme cases and has a current distribution which is reasonably forward biased.

We can also infer from this plot that there are multiple combinations of α and KE to achieve a particular transmission rate such as 50% to match the experiment. Hence, it is necessary to fix one parameter to determine the other. In this case we already know α=8.6 from our cathode characterization and this value have been used to determine the KE that fits our model the best.

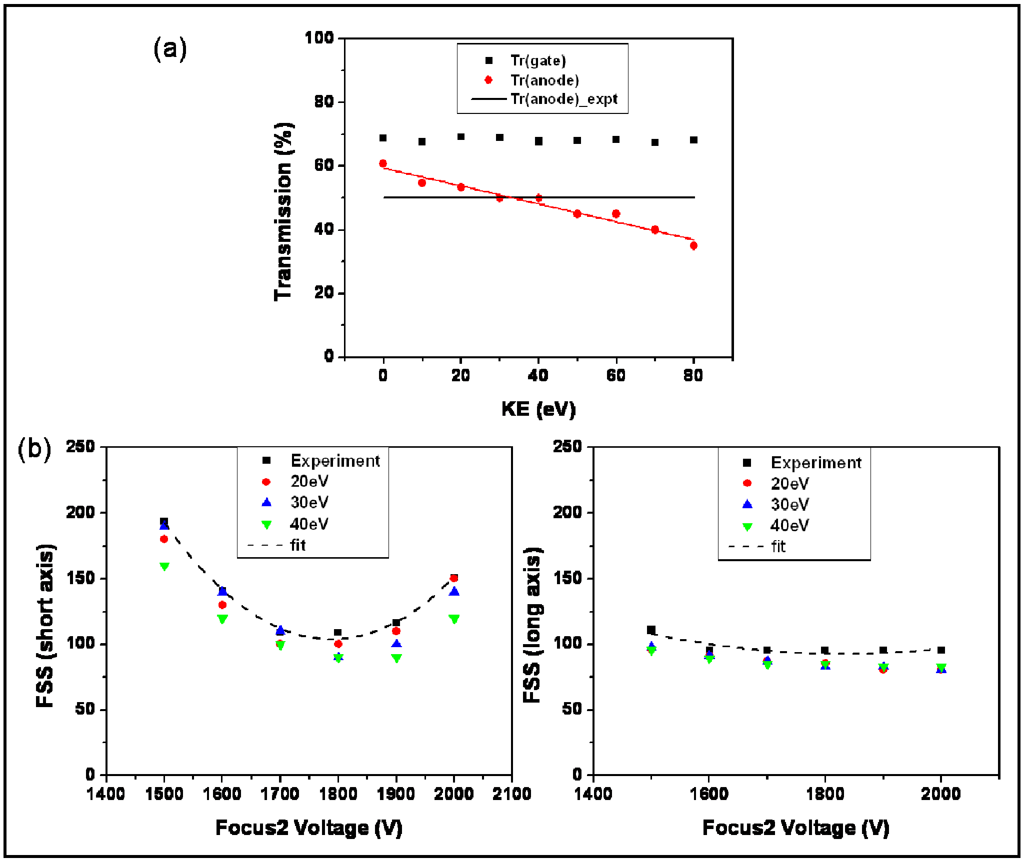

Figure 2.19: (a) Plot of transmission as a function of KE for α = 8.6 derived empirically from the cathode characterization. The physical gate opening is 75% and experimental gate transmission is 69% which is very close to the simulated data. Experimental anode transmission is 50%, which intersects the anode transmission plot at 30eV. This is the KE that has been used for the final simulations. (b) Plot of FSS along the two axes for different KE at α = 8.6. The curve for 30eV fits the experimental data the best.

Figure (2.17 (a)) shows a plot of transmission rate as a function of KE at α=8.6. From the plot 30eV fit the experimental anode transmission of 50%. Thus 30eV has been used to study the FSS (refer Figure (2.17(b))) which shows good agreement. The final combination of α=8.6 and KE =30eV has been used to specify the initial particle dynamics.

2.5.3 Comparison of Emission Models with Experimental Data

A comparison of the two electron emission models studied here has been shown in Figure (2.18). We see quantitative agreement between simulation and experiment using the Random Distribution model. FSS agrees within 16% and the transmission rate shows a close fit.

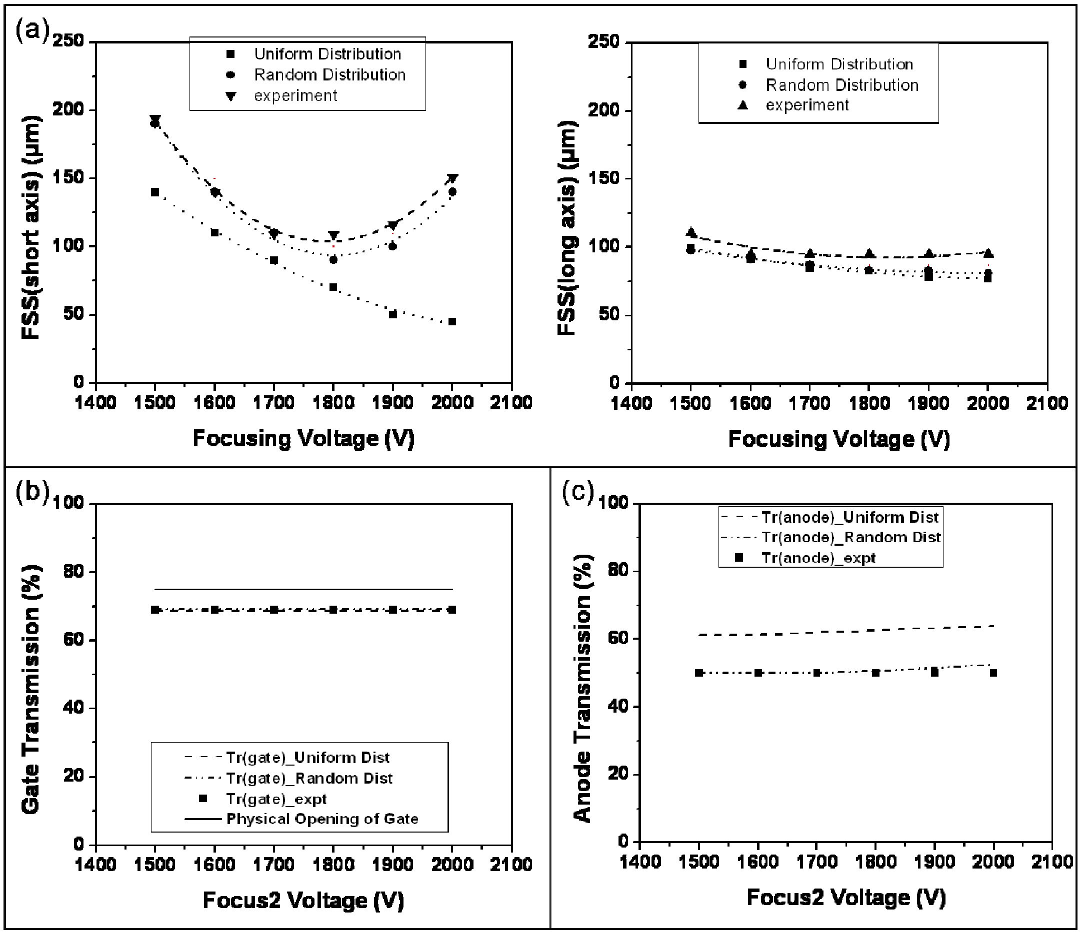

Figure 2.20: : a) Plot of the FSS (axis) as a function of the top focusing voltage for a 2.35 x 0.5 mm cathode, operating at 40KV anode voltage and about 1300V gate voltage for 0.2mA cathode current. The simulated results for the 3 different model studied have been compared with actual experimental data. The experimental measurements show best agreement (within 16%) with the Random Distribution model. (b) The physical gate opening is 75% and experimental gate transmission is 69% which is very close to the simulated data. The plot suggests that the gate transmission is independent of the emission model. (c) The Uniform Distribution model predicts significantly high anode transmission in contrary to measured value, suggesting over simplification of the field emission model. The Random Distribution model exhibits quantitative agreement with measured value.

2.6 Summary

In this chapter a brief overview of the FE analysis software OPERA-3D has been given from a physical rather than a mathematical perspective. Introduction of the actual CNT field emission x-ray source that we intend to design through this research has been done. The simulation environment in which the analysis will be conducted has been presented with the mention of some limitations. In particular, representation of the cathode characteristics turned out to be inadequate, which led to the formulation and development of a new emission model which takes into consideration the random distribution of CNTs on a large emission surface with varying field enhancement factor. The characteristics of the random emission model are as follows:

- Emitter Position – Randomly generated within the user specified emission geometry by using a Matlab program.
- Number of emitters -10,000 chosen from a range of 5000 and 15,000.
- Current Distribution – derived by using actual cathode performance and experimental setup
- Velocity Distribution – derived by using the measured anode transmission as the fitting parameter at KE=30eV. It is also assumed to be uniform along the three angular components.

Details of the new emission model followed by comparison with experimental data concluded this chapter. This model facilitated the development of a reliable simulation platform for electron optics simulations which will be used in the next two chapters to design and optimize CNT based x-ray sources for specific applications in medical imaging.

References

---

[1] L. Jacob, “An Introduction to Electron Optics”, New York: John Wiley & Sons. Inc, 1951.

[2] P. Dahl, “Introduction to Electron and Ion Optics”, Academic Press, New York and London, 1973.

[3] 0. Klemperer, W. D. Wright, “The Investigation of Electron Lenses”, Proceedings of the Physical Society, 51, 296, 1939.

[4] W. Ehrenberg and W.E. Spear, “An Electrostatic Focusing System and its Application to a Fine Focus X-Ray Tube”, Proceedings of the Physical Society B, 64,67, 1951.

[5] W.E.Spear,”Investigation of Electron Optical Properties of an Electrostatic Focusing System”, 1951, Proceedings of the Physical Society B, 64, 233, 1951.

[6] http://en.wikipedia.org/wiki/Electrostatic_lens.

[7] V.E. Cosslett, “X-ray microscopy”,Reports on Progress in Physics, 28 381, 1965.

[8] C.W.Trowbridge , K. Hoffer , and H.R. McK. Hyder, “Fields, Focusing and Aberration in Electrostatic Accelerator Tubes”, IEEE Transactions on Magnetics, Vol 40, No2, March 2004.

[9] http://en.wikipedia.org/wiki/Lens_%28optics%29#Spherical_aberration.

[10] http://en.wikipedia.org/wiki/Space_charge.

[11] A.R.Knox, A.Asenov, A.C.Lowe, *Solid_State Electronics* 45, 841-851, 2001.

[12] Vector Fields Opera 3D Reference-Scala, 2006 and ASK document from Opera.

[13]Y. Cheng, et al., “Dynamic radiography using a carbon nanotube-based field emission x-ray source”, Review of Scientific Instruments, Vol.75 No.10 p. 3264, 2004.

[14] J. Zhang, et al., “A nanotube-based field emission x-ray source for microcomputed tomography”, Review of Scientific Instruments,76, 094301, 2005.

[15] Liu, Z., Zhang, J., Yang, G., Cheng, Y., Zhou, O., and Lu, J.P., "Development of a carbon nanotube based microfocus x-ray tube with single focusing electrode", Review of Scientific Instruments, 77, 054302, May 2006.

[16] A.R. Lang and D.A.G.Broad, “Electron optics of x-ray tubes and the design of unbiased sharply-focusing cathodes”,British Journal of Applied Physics, 7, 221, 1956.

[17] J.S. Thorp, “A Study of an Electron Focusing System in an X-Ray Tube”, British Journal of Applied Physics, 1,144, 1950.

[18] B.M. Moores and P.Brubacher, “Focal Spot Studies and Electron Focusing in a Demountable X-Ray Tube”, Physics in Medicine and Biology, 19, 605, 1974.

[19] B.J. Udelson, “Electrostatic Focusing of an Electron-sheet Beam in a Symmetric Planar Structure”, International Journal of Electronics, vol 21, Bo 3, 241-276, 1966.

[20] G.H.N. riddle, “Electrostaic Einzel lenses with reduced spherical aberration for use in field-emission guns”, Journal of Vacuum Science and Technology, 15(3), May/June 1978.

[21] “ Summarized Proceedings of conference on high-intensity X-ray beams- London, April 1950”, British Journal of Applied Physics, Vol 1, Dec 1950.

[22] Liu, Z., Yang, G., Lee, Y.Z., Bordelon, D., Lu, J.P., Zhou, O., "Carbon Nanotube Based Micro-Focus Field Emission X-ray Source for Micro-Computed Tomography", Appied Physics Letters, 89, 103111, 2006.

[23] Meyyappan, M., Carbon Nanotubes: Science and Applications. Boca Raton: CRC Press, 2005.

[24] R. H. Fowler and L. W. Nordheim, Proceedings of the Royal Society of London, Ser. A 119, 173, 1928.

[25] Wei Zhu ,”Vacuum Microelectronics”, Wiley- Interscience publications, 2001.

[26] S Suzuki, C Bower,Y Watanabe, and O Zhou, Applied Physics Letters, vol 76, 26 June 2000.

[27] J. Zhao, J. Han, and J. P. Lu, Physical Review, B 65, 193401, 2002.

Chapter 3 : Design and Characterization of CNT based X-Ray Source for Dynamic and Stationary Micro-CT Systems

3.1 History and Background of Computed Tomography

Computed tomography (CT) is a very powerful tool for non-invasive medical imaging. Since its introduction in the early 1970s, it has wide spread diagnostic applications mostly because of its superiority over conventional x-ray radiography. Apart from medical applications, CT is an important probing tool in biology, materials inspection, security screening and industrial sectors as well [1].

Conventional radiography provides high-resolution images, but projects a three dimensional object onto a two dimensional plane, hence all depth information is lost during the projection process. In diagnostic and clinical applications this can be misleading and also potentially dangerous. In addition, conventional radiography has difficulty in differentiating between various tissues without contrast agents. Potential solutions to the above limitations lead to the development of conventional tomography.

Conventional Tomography

The word "tomography" is derived from the Greek words *tomos* (slice) and *graphein* (to write). Conventional tomography is an x-ray imaging method which includes synchronous movement of an x-ray source and a detector during the exposure. Consequently, structures in the focal plane appear sharp, while structures in other planes are blurred. Thus, by adjusting the direction and extent of motion, different planes can be selected depending on the object of interest. Though conventional tomography solves the problem of depth perception it suffers from high imaging dosage. This causes unnecessary irradiation of surrounding normal tissue and is not desirable for practical purposes.

Computed Tomography

Computed tomography, on the other hand, not only provides depth perception; it also helps in differentiating soft tissues as well as provides quantitative information about various tissue densities. The principle behind computed tomography technique is to reconstruct a three dimensional image of an object from multiple projection images taken from different viewing angles.

The mathematical basis for this technique was developed by Radon and published in 1917. Several research groups worked independently on the reconstruction algorithm, but Allan Cormack, at Tufts University in 1963, developed an accurate non-iterative method which made it possible to actually do a tomographic reconstruction. However, the first clinical CT scanner was not built until early 1973 by Housfield, at EMI in England. Cormack and Housfield were awarded the Nobel Prize for their contribution to this field in 1979.

CT has been one of the pillars of radiologic diagnostics. Based on scanning geometry, four generations of CT scanners have been developed. Nearly all current CT scanners use third or fourth generation geometry. During the process it has also undergone tremendous advancement in terms of speed, image quality and patient comfort. Figure (3.1) shows a schematic of the evolution of CT generations.

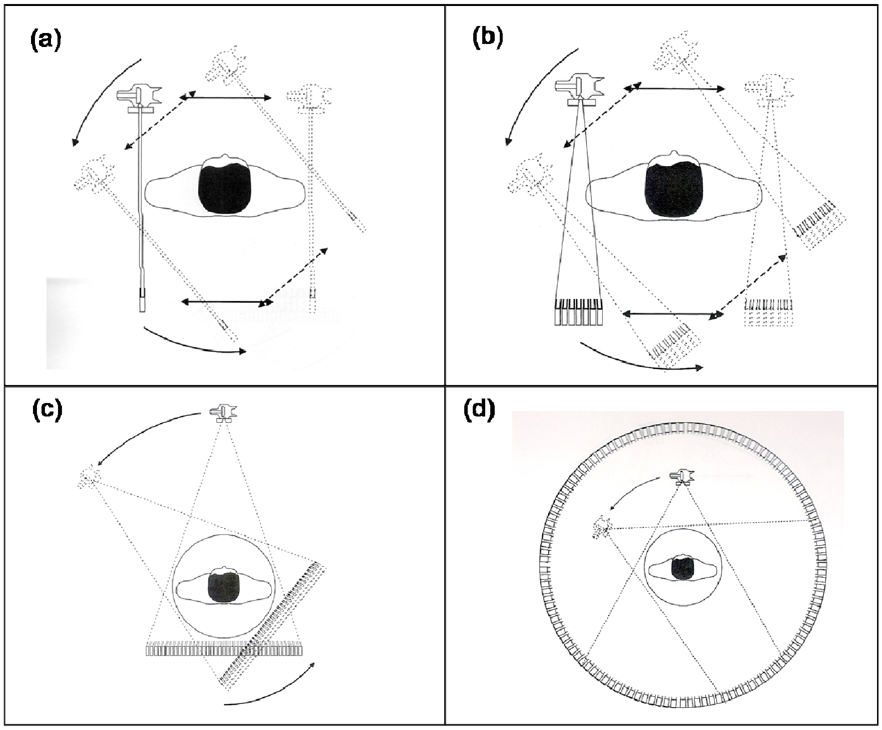

Figure 3.1: Evolution of the CT scanner: (a) First-generation scanner using a pencil x-ray beam and a single detector. (b) Second-generation scanner with a fan x-ray beam and multiple detectors. (c) Third-generation scanner using a fan x-ray beam and detector array. (d) Fourth-generation scanner with a fan beam and a stationary circular detector array [2].

3.2 Micro-CT Scanner Based on Micro-Focus X-ray Tube

CT scanners have widespread applications; however a typical CT scanner's spatial resolution is typically in the order of mm. This limits its performance for high resolution medical imaging. The spatial resolution of a CT scanner is primarily determined by the focal spot size of its embedded x-ray source, given all the other geometric parameters. Currently micro-focus x-ray rubes with micrometer scale focal spot size are commercially available. The integration of the high resolution micro-focus tube with the CT technology has evolved into a new technology called micro computed tomography (micro-CT). It is basically a scaled down version of the CT scanner with higher spatial resolution, typically in the order of 10s of micrometers, for imaging small objects. Micro-CT has emerged as a powerful non-invasive tool for biomedical research. It has been applied to high-resolution imaging of bone structures and soft tissues of small animals amongst other applications.

A typical micro-CT scanner comprises of a micro-focus tube, a sample stage and a flat panel x-ray detector as shown in Figure (3.2). The entire process is controlled by a computer station. There can be two geometries where (1) the x-ray source and detector are mounted in parallel and rotate around the specimen, or (2) where the x-ray source and detector are fixed but the sample stage is rotated 360° for image acquisition in different views. Typically for micro-CT, the cone-beam geometry is widely used where the x-ray source has a large cone angle to cover the entire specimen. The two dimensional projection images are then used to reconstruct a three dimensional image of the object.

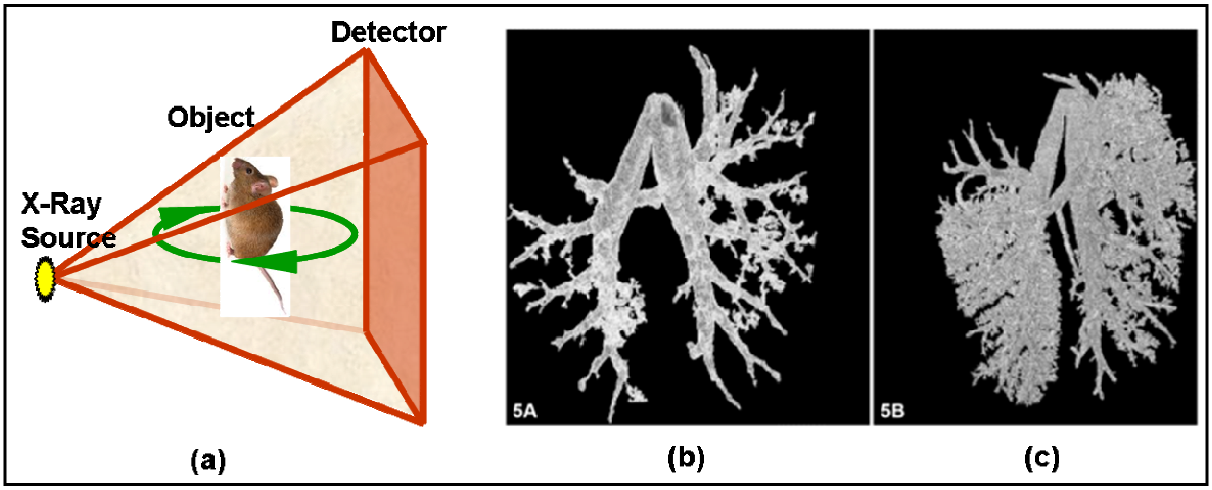

Figure 3.2: (a) The typical cone-beam geometry used in micro-CT scanner. In this scanning mode, cone-beam x-ray generated by the x-ray source has large enough cone angle to cover the entire object and the transmitted x-ray images are recorded by a two dimensional x-ray detector. (b) Low-resolution and (c) high-resolution 3D models from micro-CT image data of the airway of fixed mouse lungs (reproduced from http://tpx.sagepub.com/content/35/1/59/F5.expansion.html)

Current micro-CT scanners are typically comprised of conventional x-ray sources which have limited temporal resolution because of the intrinsic electron emission mechanism. This is a huge limitation for dynamic imaging of small animals where the source needs to be synchronized with the physiological motion of the animal. As can be seen in table (3.1), mouse has 10 time's faster respiration and cardiac cycle than human beings. This means to capture an image without motion blur it has to be acquired within a very small time frame or very high temporal resolution. Also, high spatial resolution is needed to visualize small anatomical features in the mouse. In addition total dose needs to be small to do longitudinal disease studies. These limitations can be addressed by a CNT based x-ray source with high temporal and spatial resolution and will be discussed in the next section

Specimen	Human	Rat	Mouse
Weight (g)	70,000	250	25
Breath (min)	12	85	120
Heartbeats (min)	60	300	600

Table 3.1: Comparison of different physiological characteristics for varying specimen size.

3.3 Micro-Focus X-Ray Source with CNT Field Emitters

Based on the field emission micro-focus x-ray source developed at our laboratory, a desktop cone-beam x-ray micro-CT imaging system has been built for the general radiographic and tomographic imaging purposes. An integral part of a micro-CT scanner is the micro-focus x-ray tube. Hence, design and development of a CNT based micro-focus tube has been the primary goal of this work which will be described in detail in the remainder of this chapter. Before going into the details of the tube design an overview of the system is briefly described.

Figure (3.3) shows the CAD design of the arrangement of the micro-CT scanner. It comprises of a CNT field emission micro-focus x-ray tube, a flat panel detector a high precision goniometer (Model 430, HUBER, Germany), and a home-made mouse bed. The x-ray tube and the detector are mounted on two translational stages and can rotate around the sample (mouse bed) stage. The two translational stages are positioned on the opposite sides of the goniometer and have the flexibility to adjust the distances.

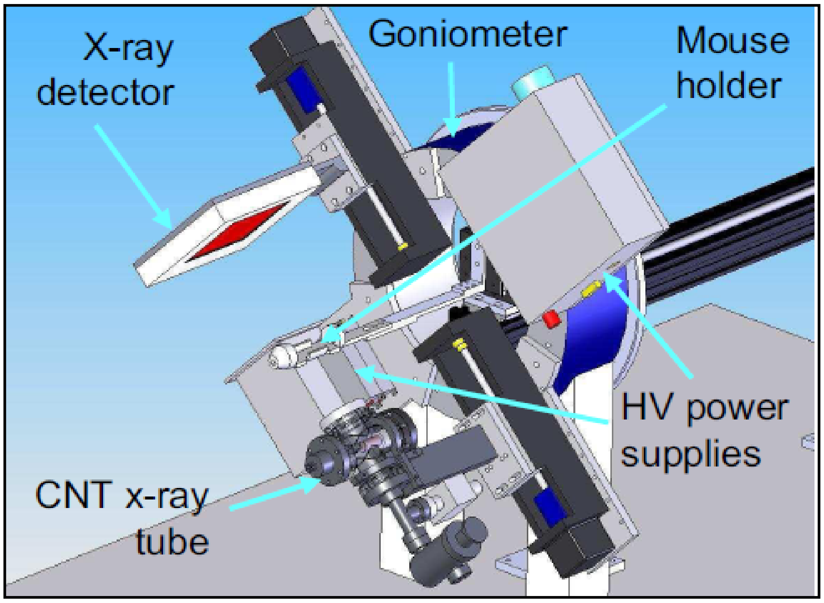

Figure 3.3: schematic diagram of the micro-CT scanner. It includes a stationary x-ray source, a sample rotation stage, a 2D digital x-ray detector, and a computer workstation. [3, 4].

A schematic representation of a single source unit is shown in Figure (3.4). It consists of a CNT cathode, a gate electrode with a tungsten 2D square mesh for the extraction of the electrons, an electrostatic focusing unit (comprised of Focus1 and Focus2 electrodes) and a stationary target (anode made of molybdenum). By applying a variable electric field to the gate electrode, usually in the order of 0-10V/μm, electrons are extracted from the CNT cathode. The emission current from the CNT cathode can be varied by adjusting the gate potential. The two focusing electrodes are controlled by two independent power supplies connected to them. Depending on the potential applied to the focusing electrodes the electron beam trajectory changes, thus varying the FSS. A systematic study of various parameters affecting the FSS has been conducted using electron optics simulations. Experimental measurements were also performed to confirm the results as reported in the following sections. The aim is to obtain 100µm FSS with small cathode pitch. This enabled us to develop a compact x-ray source which is portable. The design is based on Einzel lens type electrostatic focusing x-ray source design that has been previously developed in the "Zhougroup"[5,6,7].

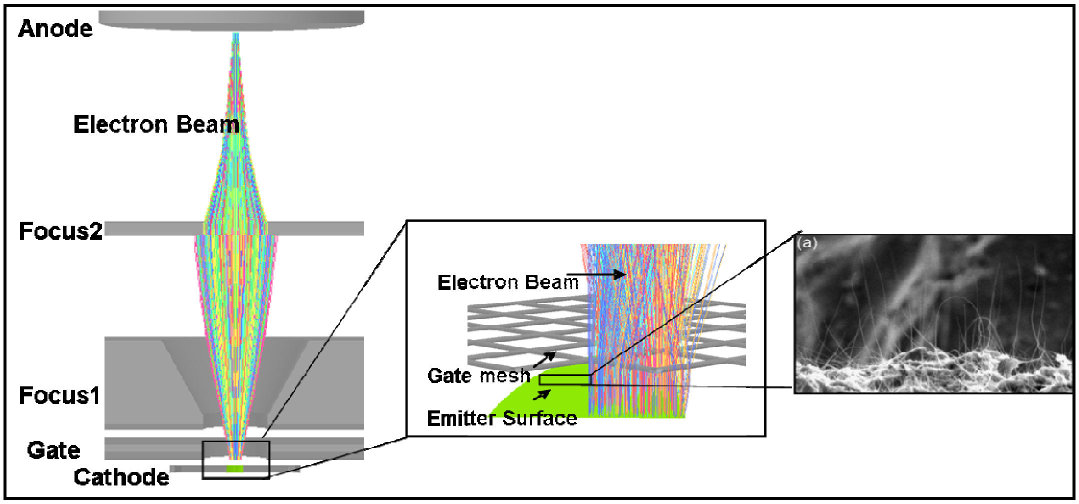

Figure 3.4: Schematic of the basic components of a micro-focus x-ray tube consisting of a cathode, a gate electrode, a focusing unit (Focus1 and Focus2) and an anode with takeoff angle of 12°. Also seen is the detailed assembly of the gate mesh above the cathode emission surface for extraction of the electrons and a high resolution SEM image of the cathode with activated CNTs. The representative beam profile also gives an idea about the trajectory followed by the beam.

3.4 Initial Optimization of Geometric Parameters using Uniform Emission Model

Initial simulations were performed with a coarse model assuming that the electrons have no divergence and are emitted perpendicular to the emission surface. The trend of the electron beam behavior was studied at this phase rather than the absolute numbers. A single source unit was considered for simulations with a flat anode for ease and accuracy of the simulations. In addition, to reduce computation time, symmetry was applied to the model. Quarter symmetry was applied to the actual simulations. The following section demonstrates the effects in more detail.

3.4.1 Different Focusing Geometry

As mentioned earlier, the x-ray tube design is based on the Einzel type electrostatic focusing design developed earlier in the “Zhougroup”. For this tube design different shapes for the Einzel type lens were considered. As seen in Figure (3.5), three different geometries were studied: (a) a truncated cone shape with two focusing electrodes, (b) a clear through-hole with two focusing electrodes and (c) a single inverted truncated cone structure. The simulated FSS for the different structure showed that the a truncated cone shape with two focusing electrodes was the most effective focusing structure and was considered for the final design, as shown in Figure (3.5)(d).

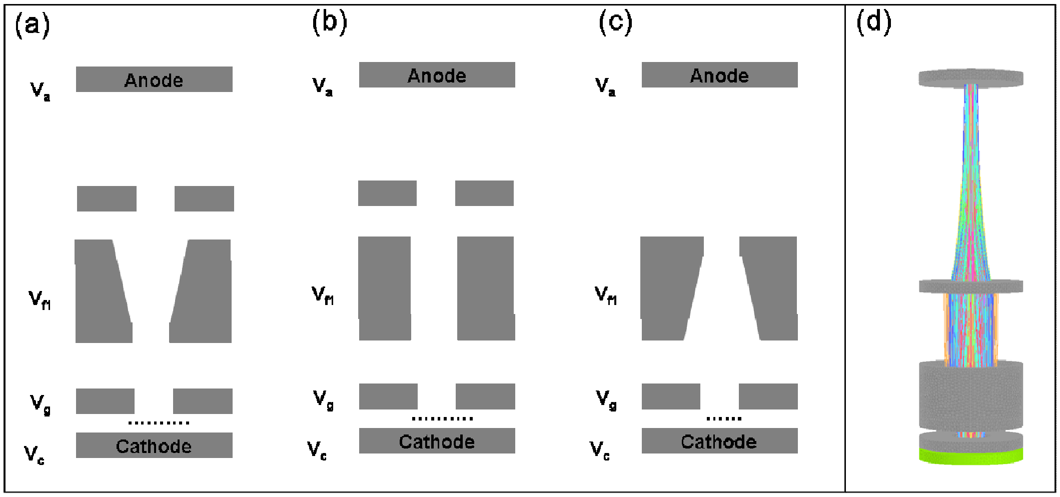

Figure 3.5: Different focusing geometry for the middle focusing electrode was studied. (a) a truncated cone shape with two focusing electrodes, (b) a clear cylindrical structure with two focusing electrodes and (c) a single inverted truncated cone structure. The simulated FSS for the different structure showed that the truncated cone shape (a) with two focusing electrodes was the most effective focusing structure. (d) Representative beam profile using the truncated cone geometry.

3.4.2 Effect of Anode Angle

For simplicity of design and model setup a flat anode was used for actual simulations instead of a tilted anode. However, it was important to see the effect of this assumption, and a comparison of the two cases was made. The two models considered are shown in Figure (3.6), where everything was kept constant except for the anode angle. Typically for micro-CT scanners the anode tilt angle is 12º for a reflection type micro-focus x-ray tube. Hence, a 12º tilted anode has been compared to an anode with no tilt angle.

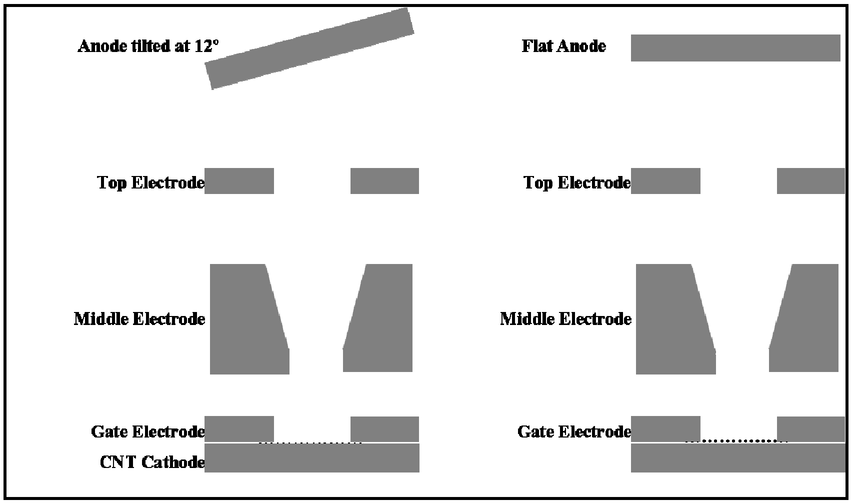

Figure 3.6: The model considerations for anode tilt angle effect. An anode with 12º tilt angle has been compared with an anode with no tilt angle.

The electric potential at the centre of the anode was plotted as a function of distance from the cathode surface to the anode surface. The graph didn't show any significant change in the potential distribution on the anode surface for the two models considered here. Also, the FSS exhibited negligible difference; hence the flat anode was used for all the future simulations.

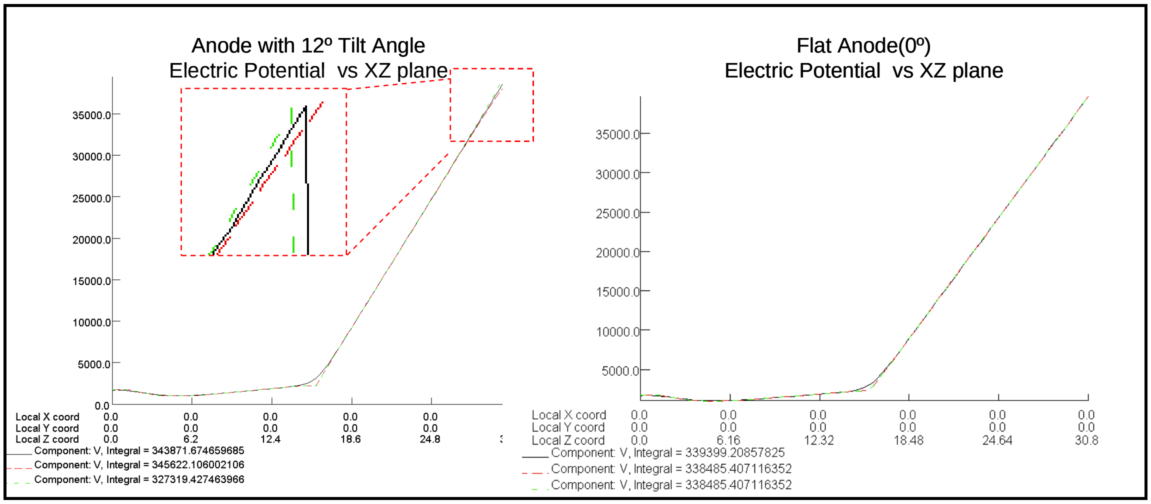

Figure 3.7: Plot of potential distribution along the length of the x-ray tube. Difference in the potential distribution because of anode tilt angle is negligible.

3.4.3 Effect of Machining Tolerance

Since the pitch between the individual x-ray cathodes was only 5mm, a study was performed to see the effect of lateral misalignment for 100µm. Two extreme cases were considered, where the apertures for all the electrodes were increased by 100µm in the first case, and decreased by 100µm for the second. The results show that the FSS increased by 8% when the apertures were increased by 100µm but remained unaffected in the second case. The anode transmission changed within 5% of the original case. Figure (3.8) shows a schematic representation of the study.

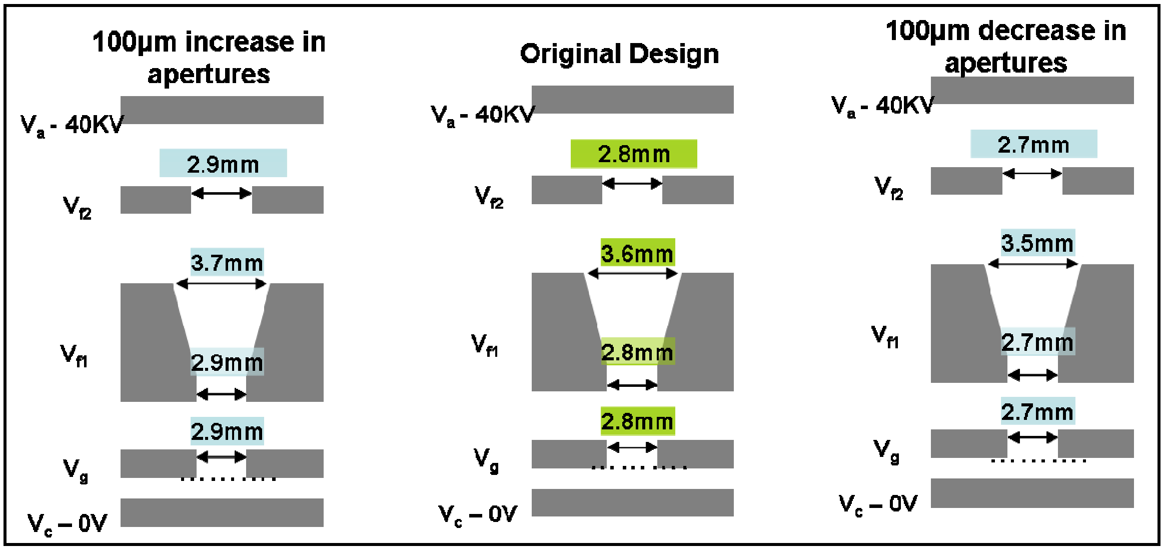

Figure 3.8: The machining tolerance was assumed to be within 100µm. Hence, the apertures for the electrodes were increased /decreased from the original design to check the effect on the focal spot size as well as the transmission rate. The simulation was done at anode potential 40KV and gate potential 1500V. The focusing voltages were V(f1)=1000V and V(f2) =2200V respectively. The cathode considered was a 1mm circular cathode.

3.5 Final Micro-Focus X-Ray Source Design using Random Emission Model

After the initial studies and on further optimization of the geometric parameters the new design was finalized with individual pixel pitch of 5mm. The electron optics simulations predicted that a FSS of 100µm x 120 µm (long axis x short axis) can be reached by using this structure, which is 25% smaller than the early results of 112 µm x 152 µm. Figure (3.9) shows a picture of the actual prototype x-ray tube built for laboratory testing and the inset is a schematic representation of the in-chamber components. The x-ray source is a 3 unit module consisting of a field emission CNT cathode, a focusing structure and a Mo target (anode) housed in a vacuum chamber. The housing is made of a stainless steel tube with an aluminum x-ray exit window. The high vacuum was created using a mechanical pump and an ion pump and was operated at 10^{-7} Torr. Some of the key performance characteristics of an x-ray source include flux, resolution and stability. Significant effort has been put in the CNT cathode fabrication to ensure its long-term stability. The CNT cathode used in this study has a 2.35mm x 0.5mm elliptical area and can easily reach an emission current of 3mA (325 mA cm^{-2}) under pulsed mode. For long term stability, a constant cathode current of 3mA for 90hrs can be maintained with only 13% change in extraction voltage due to gradual CNT cathode degradation [8]. 3mA was chosen since it is the maximum current allowed under the present operating condition of 40KV anode voltage, 60% transmission rate at the anode and isotropic 100μm FSS, without going into anode heat limitation. The max power for a stationary-anode micro-focus x-ray source approximately follows the empirical relationship

$$P_{\max} \approx 1.4\left(d_{f\_FWHM}\right)^{0.88} \qquad \text{Equation 3.1}$$

for anode potential 40KV, where $d_{f,FWHM}$ is the focal spot size in microns[5,6].

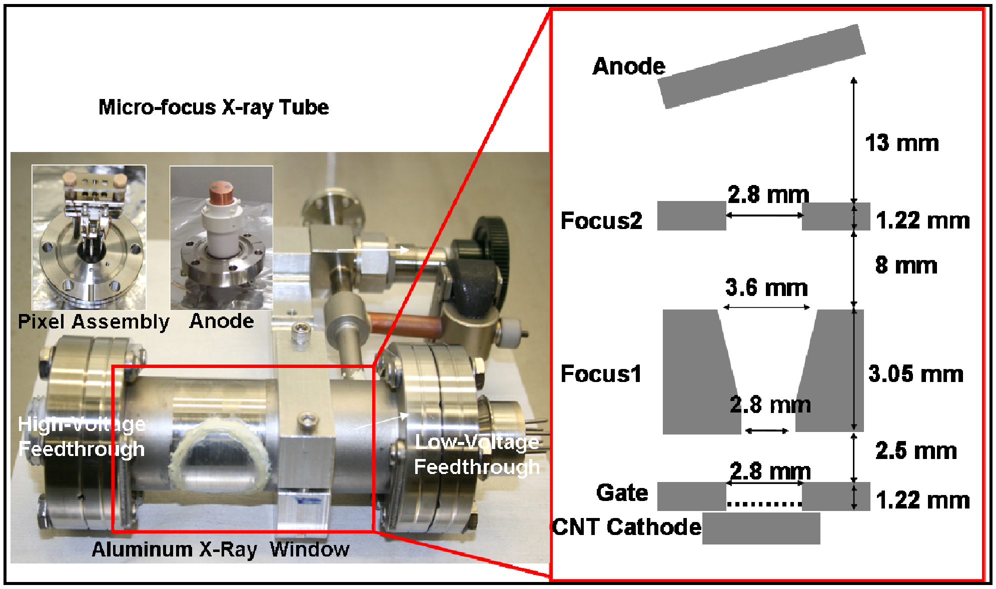

Figure 3.9: Image of the actual x-ray tube with an Al exit window. The inset shows the dimensions of a single cathode-anode assembly.

The micro-focus FEX tube has a triode structure and the tube current is controlled by the potential applied to the gate electrode. The gate electrode comprise of a wire mesh which helps in the extraction of electrons from the CNT cathode when a bias voltage is applied to the gate electrode. The electrons diverge after passing the gate mesh which is subsequently focused back by an active focusing unit made of metal diaphragms placed after the gate electrode before striking the anode as seen in Figure (3.4). The focusing unit is based on an asymmetrical Einzel type lens. The focusing electrodes have individual and independently controlled potential that shape the beam profile and eventually the focal spot size of the electron beam [9]. The geometric parameter of the gate electrode and the focusing unit has been optimized with the aid of electron optics simulations.

3.6 Experimental Setup for Focal Spot Size (FSS) Measurement

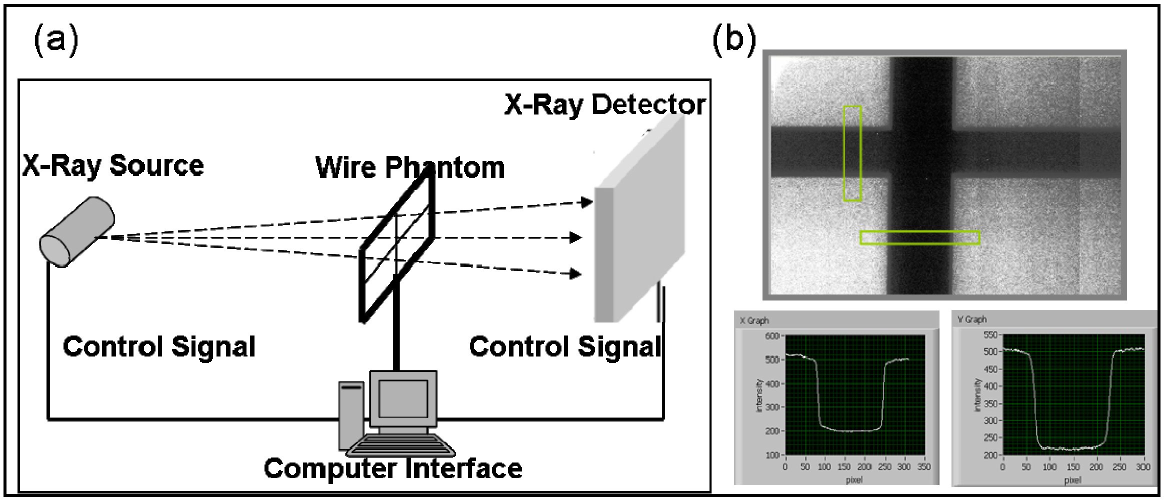

Figure 3.10: (a) Schematics of the experimental setup. It comprise of an x-ray source, a 1mm tungsten crosswire phantom and a 2D flat panel detector (Hamamatsu C7921) with pixel size 50µm and can be externally triggered. There is also a control station for data acquisition and other automated operations. (b) Projection image of the cross wire phantom and the region of interest used to obtain the line profile along the vertical and horizontal direction using a 1.18 x 0.25 mm CNT cathode.

Figure (3.10) is a schematic representation of the FSS measurement setup. It consists of the CNT micro-focus x-ray tube, the crosswire phantom and a 2D x-ray sensor. The sensor used for FSS measurement is a flat-panel (Hamamatsu C7921) 2D detector arranged in cone beam geometry. The detector contains a CsI scintillator plate, a 1056x1056 photodiode array with a total field of view of 52.8x52.8mm.The available pixel size is 50μm and the video output is a 12 bit digital signal. The spatial resolution is measured using the geometric blur of a 1mm tungsten crosswire. The exposure window of the detector and the beam on-time of the x-ray source are synchronized to acquire the projection image. A line profile is obtained from the projection image of the crosswire as see in Figure (3.10(b)) in the vertical and horizontal direction. The FSS is then calculated based on the European Standard EN 12543-5[10].

3.7 Field Emission Performance of the CNT Micro Focus X-Ray Source

To evaluate the field emission properties of the CNT cathode and also to measure the FSS the micro-focus tube was assembled with a 2.35x 0.5mm elliptical cathode. The tube was then baked at high temperature overnight to remove all the moisture or any adsorbed gas inside the tube. A proper conditioning of the tube is essential to eliminate unnecessary arcing and breakdown. First, a high voltage conditioning is done where the anode voltage is incremented in steps up to 55KV; this reduces the chances of arcing as well as removes any unwanted hot spot. This is followed by a field emission measurement in triode mode. The anode voltage is set at 10KV, the top focusing electrode at 2000V and the middle focusing electrode at 300V. The gate voltage is then incremented in steps using a labview program. Figure (3.11) shows a representative plot of the experimentally measured emission current density versus the applied electric field. For a CNT cathode with an area of 0.92 mm^2, the current density at 8.7 V/μm is 385mA/cm^2.

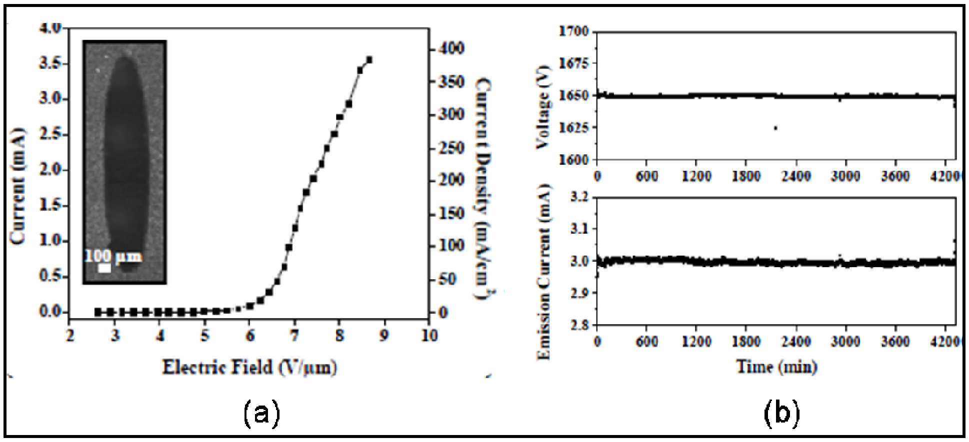

(a)

(b)

Figure 3.11 : (a) Field emission current as function of applied electrical field for 2.35 x 0.50 mm cathode. The measurement conditions used were 10 KV at anode, 2000 V at top focusing electrode and 300 V at middle focusing electrode. Inset shows Optical image of the CNT cathodes.(b) Emission lifetime measurement of a 2.35 x 0.50 mm CNT cathode at constant current mode into the micro focus X-ray tube. The measurement conditions used were 40 KV at anode, 1400 V at Focus2 electrode and 1300 V at Focus1 electrode. The peak emission current in the pulsed mode was fixed at 3mA and an averaged peak current of 3.00 ± 0.01mA was obtained [8].

3.8 Agreement between Simulation and Experimental Results

FSS measurements were done using a 2.35x0.5mm cathode at 40KV anode potential. The gate potential was 1260V with an emission cathode current of about 0.2mA. A duty cycle of 50 % (0.2 f/s and 2.5 sec pulse width) was used for image acquisition. Table 3.1 shows the summarized experimental results for varying focusing potentials.

F1/F2	1500	1600	1700	1800	1900	2000
800	108*194	99*155	99*112	96*101	99*112	95*132
900	111*194	95*140	95*105	95*109	95*116	95*151
1000	127*202	111*135	103*104	107*104	103*124	109*163
1100	155*201	127*132	103*104	95*104	99*132	103*171
1200		151*147	134*109	111*109	103*140	116*186

Table 3.2: : Summary of the typical variation of the focal spot size as a function of the applied potential for Focus1 and Focus2 electrodes for a 2.35 x 0.50 mm CNT cathode. The unit for the vertical and horizontal direction is micrometer. The experiment was done at 40KV anode voltage and 1260V gate voltage using a 1D linear tungsten mesh.

To confirm the reliability and accuracy of any simulated data, I have selected a random row from Table (3.1) to plot the FSS as a function of the top focusing electrode

(Figure (3.12)). The smallest FSS that can be achieved using this tube design is 95x104µm. Simulation and experimental results agree within 16% of each other. This gives 25% smaller FSS compared to the earlier results. The transmission rates also show good agreement.

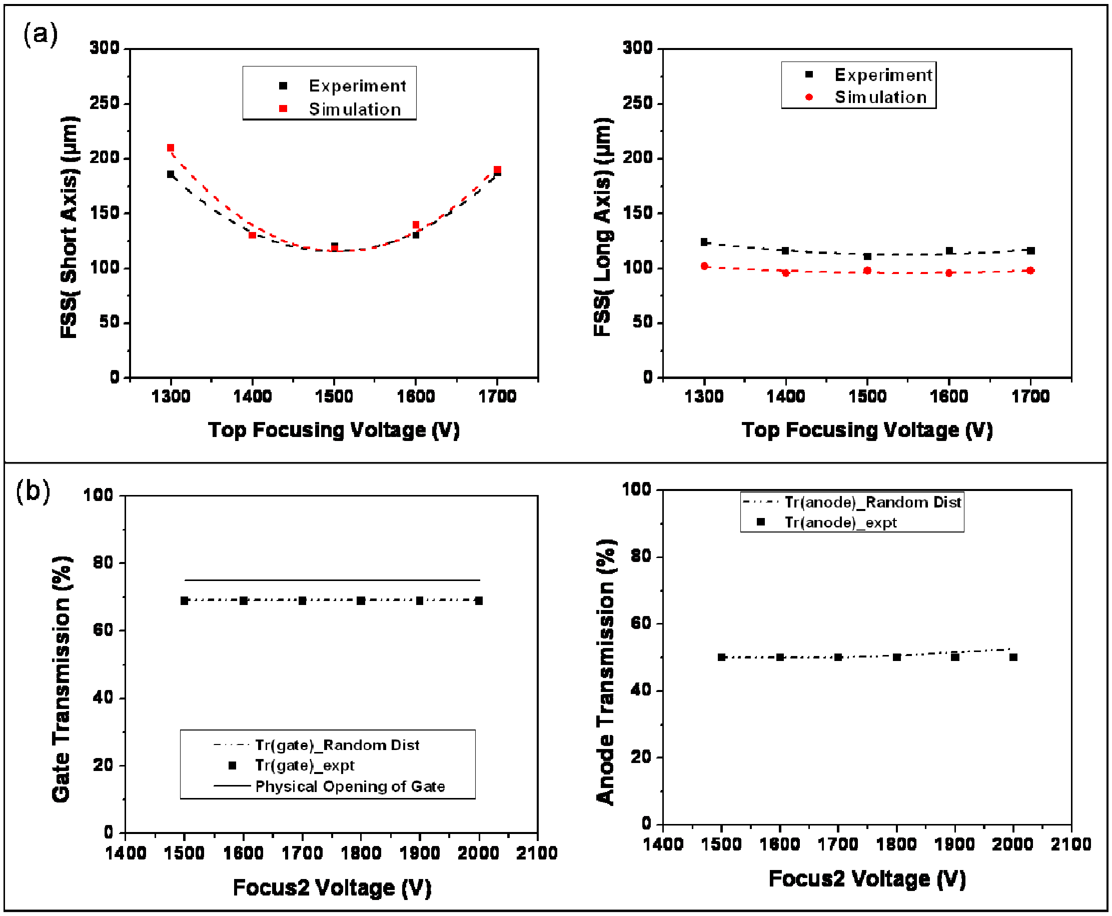

Figure 3.12: (a)Plot of the focal spot size as a function of Focus2 potential. The cathode size is a 2.35x0.5mm elliptical CNT cathode measured at 40KV anode voltage ,1260V gate voltage and 900V Focus1 voltage. Simulation and experiment agree within 16%. (b) Plot of transmission rate at gate and anode showing quantitative agreement.

3.9 Effect of Various Parameters on the FSS

Some of the important performance characteristics of an X-Ray source are flux, stability and resolution. The first two factors have been successfully achieved [8]. Here the focus is mainly on high spatial resolution of the x-ray tube. Since the spatial resolution of any scanner is primarily dependent on the x-ray FSS, given all the other parameters, it's crucial to have a good understanding of its behavior. A systematic study of the effect of various parameters on the FSS using the "Random Distribution" electron emission model has been done. This gives us a feel for the source behavior under operating conditions with room to improve any critical issues. The details of the study have been described in the following sections.

3.9.1 Mesh Optimization and Variable FSS

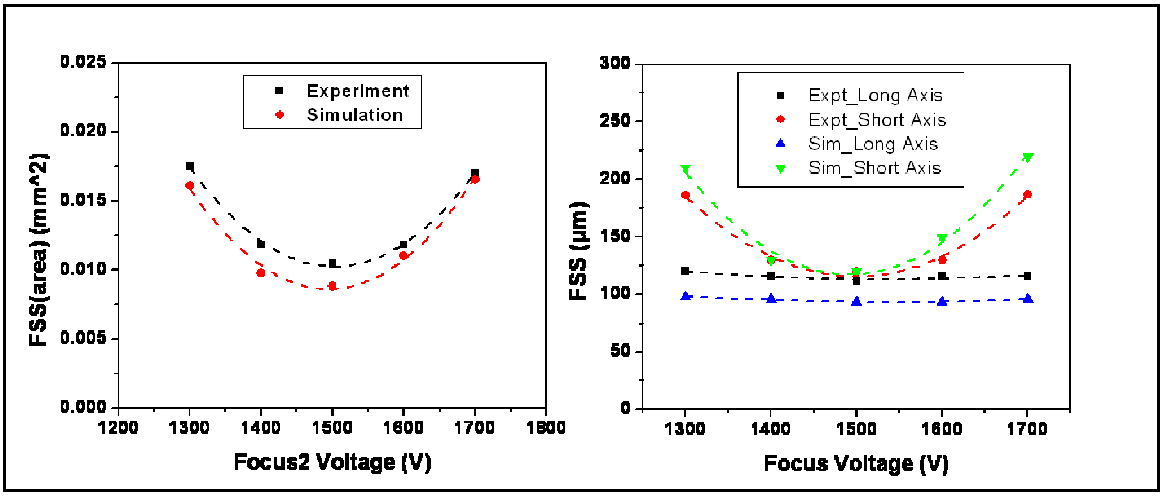

Figure 3.13: A plot of FSS as a function of the top focusing voltage at 40KV anode voltage and 1260V gate voltage. Simulation and experimental values agree within 24% of each other

A prototype tube was built in the laboratory for initial testing. The results of the experimental measurements of FSS have been plotted as a function of the Focus2 voltage as shown in Figure (3.13). Simulation and experimental results agree within 24% of each other and the smallest FSS achieved is 110 x 120µm, which is 27% larger than our target value of 100x100µm. This led us to investigate further and we found that the gate mesh wires in addition to electron extraction from the CNT cathode also strongly deflect the electron beam trajectories, making it challenging to focus the electron beam. The divergence phenomenon has been shown in Figure (3.14). After passing the gate mesh, electrons diverge due to the non uniform electric field distribution near the gate mesh wires. This happens in both the long and short axis of the cathode which limits the focusing power of the electrostatic lens. One of the major improvements done in this work is to replace the 2Dmesh (initial tube design had a 2D square mesh geometry, Figure (3.14) (top)) by a 1D linear mesh and to study its impact on the FSS. The idea is to reduce divergence along the short axis of the cathode by eliminating mesh wires along this axis. As seen in Figure (3.14) (bottom), when the gate mesh is replaced by a 1D linear mesh which has parallel wires only along the short direction of the cathode, reduction in electron beam divergence is observed thus giving a small FSS. Furthermore, for a given mesh wire size and comparable physical opening of the mesh, 1-D linear mesh will have smaller pitch compared to 2-D square design. For example a 2D mesh (pitch 250μm and wire width 25μm) with 81% physical opening will translate to a 1D mesh with 81% physical opening with 25μm bar width but 131μm pitch which is ~38% smaller pitch. This implies a uniform electric field distribution on the emitter surface thus achieving higher x-ray flux for a given cathode current.

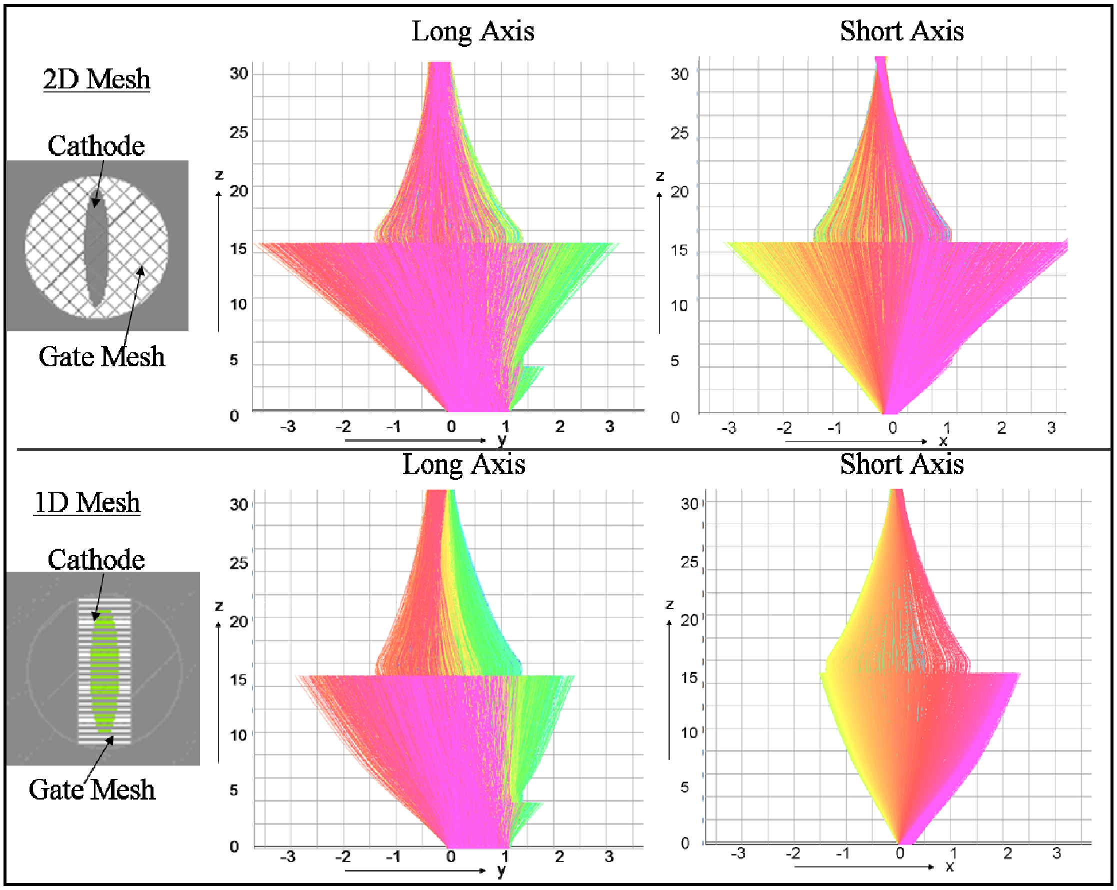

Figure 3.14: (top) Shows the beam divergence after passing through the 2D square gate mesh. The electrons experience large divergence in both directions of the cathode making it difficult to focus them back to a point on the anode surface. (Bottom) When the 1-D linear gate mesh is used the divergence along the short axis of the cathode is reduced making it easier to focus the beam. In addition, smaller amount of the beam is blocked by the focusing structure, enhancing x-ray flux generated. (The beam trajectory profiles show half symmetry)

However, using the 1D linear gate mesh solves only part of the problem since the wrong mesh geometry can again jeopardize the results. To optimize the gate mesh, a set of electron optics simulation was done with three different 1D linear gate mesh pitch (100µm, 125 µm & 150 µm) with same wire width of 25 µm and 50 µm thickness As seen in Figure (3.15), the electric field non-uniformity increases with large mesh pitch, which can lead to large FSS. Again, if the pitch is too small, it will compromise the transmission rate, allowing only a small fraction of the cathode current to reach the anode. Based on the simulation results a pitch of 100 µm was found to be optimal.

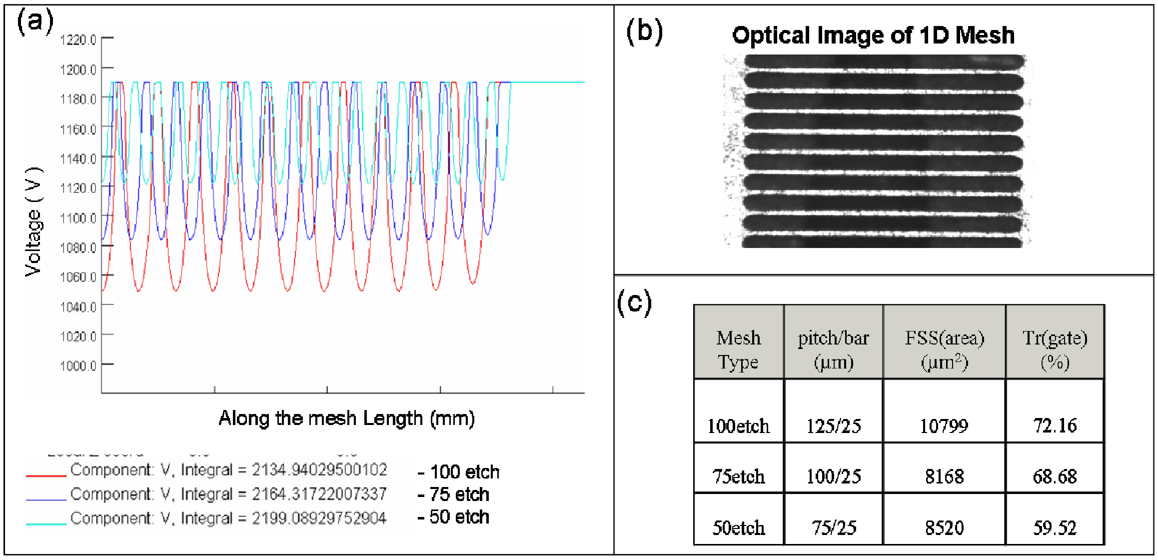

Mesh Type	pitch/bar (μm)	FSS(area) (μm^2)	Tr(gate) (%)
100etch	125/25	10799	72.16
75etch	100/25	8168	68.68
50etch	75/25	8520	59.52

Figure 3.15: (a) plot of the gate potential along the mesh length has been shown for the different pitch (75μm, 100 μm & 125 μm). It is clear that the field becomes very non-uniform as the pitch increases this will cause more divergence. Again if the pitch is too small it will compromise the transmission rate as is evident from (c). (b) Optical image of the 1D mesh. (c) FSS and transmission rate at gate for the different 1D mesh. Based on the FSS and the transmission rate a pitch of 100 μm with wire width of 25 μm and 50 μm tungsten etched mesh was chosen for this experiment.

The experimentally measured FSS (area) for 1-D linear and 2-D square mesh are shown in Figure (3.16 (a)) as a function of the Focus2 voltage. Using the 1D mesh leads to a 30% reduction in the FSS (area) compared to 2D mesh. Also seen in the curve is a minimum point, which is the optimal region of operation for high spatial resolution imaging. A 20% overall gain in anode transmission is also observed. This is primarily due to the fact that there is less beam divergence hence fewer electrons are blocked by the focusing electrodes.

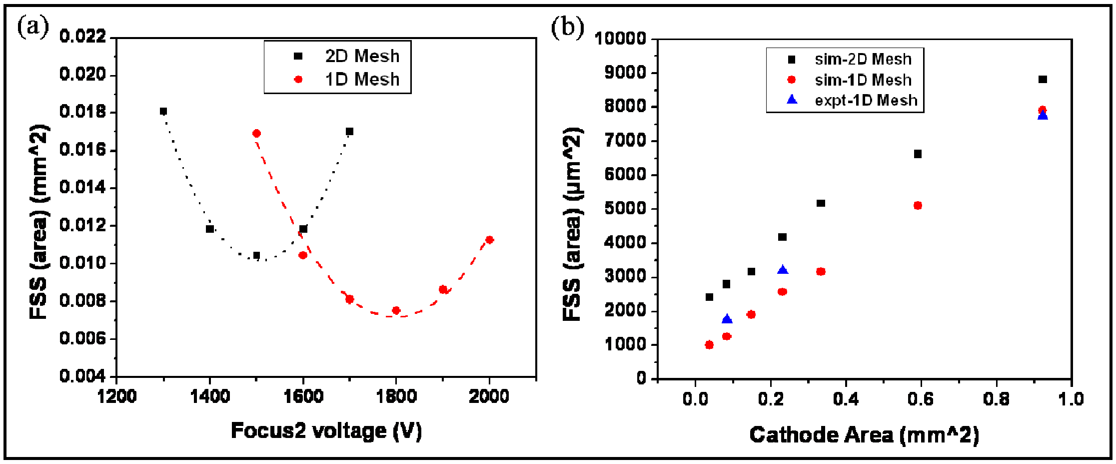

Figure 3.16: (a) Plot of the experimentally measured FSS (area) as a function of Focus2 voltage at 40KV anode voltage and 1260V gate voltage. These results confirm the simulated values. Smallest FSS achieved using 1D mesh is 95x104µm compared to 110x120 µm using 2D mesh. This gives a 32% reduction in focal spot area. Cathode used is 2.35x0.5mm elliptical CNT cathode. (b) Plot of optimal FSS (area) as a function of CNT cathode area for different cathode size. The 1D linear mesh has better focusing power that the 2-D square mesh.

The change in the gate mesh geometry helped in achieving high spatial resolution. In an attempt to further reduce the focal spot size, the cathode size was varied (made smaller). Figure (3.16(b)) shows the plot of the FSS (area) as a function of the cathode area. It can be seen that across all cathode sizes, the 1D mesh exhibit better focusing power than the 2D mesh. Experimental measurements have also been added to the plot which confirms the predicted values. We can reliably conclude here that the electron optics simulations can reliably and accurately predict the electron beam behavior.

However, we also observe a decrease in the focusing power as the cathode size is reduced. This is evident from the Figure (3.17) where the demagnification factor decreases with decrease in cathode size. One possible cause for this might be that at smaller cathode size the current density is much higher, hence there is a significant space charge effect. It also means that this particular focusing structure is less effective for small cathodes.

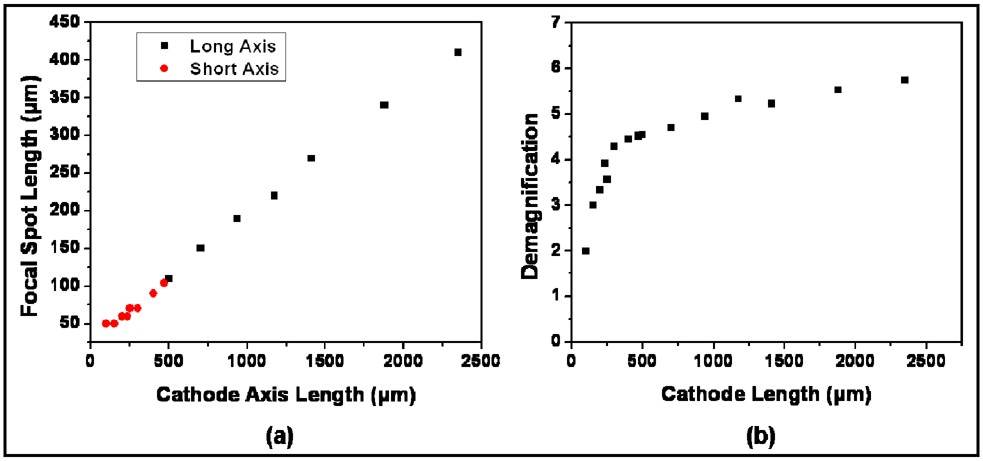

Figure 3.17: (a) Shows a plot of the FSS as a function of the cathode axis length. (a) Shows the demagnification factor for plot (a). As is evident there is a clear decrease in the focusing power as the cathode size becomes smaller.

3.9.2 Effect of Anode Potential and Distance between Focus2 and Anode

Figure (3.17) shows the variation of FSS as a function of the electric field between the anode and focus2. The plot shows two curves. One shows the influence of varying anode potential; keeping the distance between cathode and anode (represented by black squares) same. The second curve (red dots) shows the effect of varying the distance between Anode and Focus2, keeping a fixed anode potential. The overlapping of two set of data indicates that the focusing power is dependent on the electric field distribution between focus2 and the anode. We can also say that for a given anode potential, there is an optimal distance to get the smallest FSS. However, there are some practical constraints to the smallest distance that can be used for a system. The distance cannot be too small as this might cause electrical breakdown on application of a high voltage and might lead to arching. This is not desirable as it might lead to cathode failure or sometimes even complete system failure.

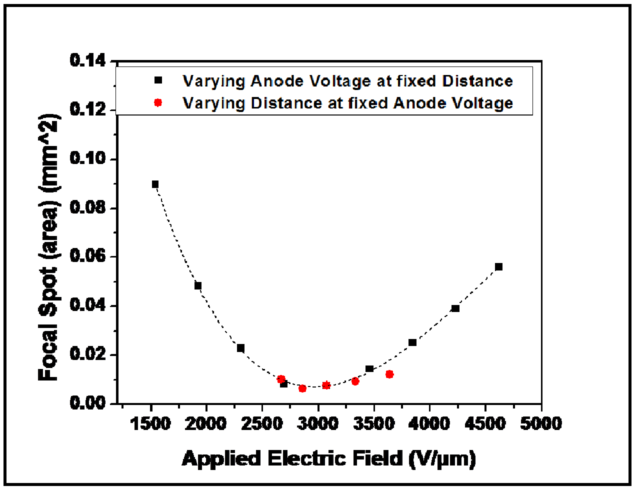

Figure 3.18: Plot of the FSS as a function of the applied electric field. Curve 1 (represented by black squares) shows the influence of varying anode potential on the FSS while keeping the distance between Focus2 and Anode fixed at 13mm. Second curve (red dots) shows the effect of varying distance between Focus2 and anode at a fixed anode voltage, 40KV. Fitting curve has been added for ease of reading the data. All these simulations were done at gate voltage 1260V, V_{f1} 900V and V_{f2} 1700V respectively.

Experimental measurements done at 40KV and 50KV have been summarized in Table (3.3). We observe a change in the effective FSS area with varying cathode size for a fixed distance between Fcous2 electrode and the anode. There is a definite reduction in focal spot area as the anode voltage increase.

Cathode Area (mm^2)	Effective Focal Area (µm^2)		
	40 KV Anode Voltage		50 KV Anode Voltage FSS (long x short)
	FSS (long x short)	Demagnification (Linear)	
0.923 (2.35x0.500)	7596 (93x104)	11.0	6970 (87x102)
0.461 (2.35x0.500)	5150 (83x79)	9.5	4778 (77x79)
0.231 (1.18x0.250)	3455 (50x88)	8.2	3141 (50x80)
0.139 (1.18x0.150)	4536 (76x76)	5.5	4334 (62x89)
0.055 (0.706x0.100)	2782 (46x77)	4.5	2757 (54x65)

Table 3.3: Effective focal area at 40 and 50 KV anode voltages. The measurements were performed at a magnification of 8 using a tungsten cross-wire phantom and following the European Standard (EN 12543-5).

3.9.3 Effect of Focusing Voltages

The Einzel type lens shapes the electron beam profile when a potential is applied to the focusing electrodes. The beam profile varies with the combination of the focusing voltages applied, thus varying the FSS. The principal function of the focusing structure is to focus the divergent beam to a finite point before reaching the anode surface. The Focus1 electrode primarily helps in harnessing the divergent electrons coming out of the gate mesh and pre-focuses the beam to a parallel shape before it reaches Focus2 electrode. In addition, V_{f1} primarily determines the size of the FSS. On the other hand, the Focus2 electrode moves the axial focal plane along the vertical direction. However, the effects of the two focusing electrodes are not completely independent of each other [6].

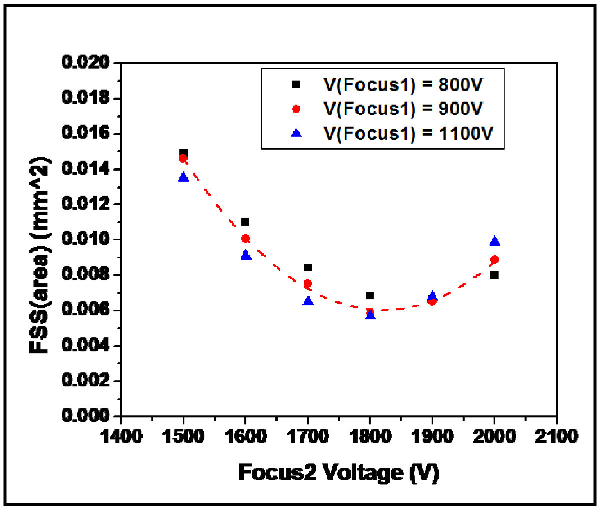

Figure 3.19: Plot of the FSS(area) as a function of Focus2 voltage for different V_{f1}. The effective focal spot area is insensitive to V_{f1} that gives a broad region of operation to maintain the same focal spot area just by tuning the focusing potentials. However, the FSS is highly sensitive to V_{f2} following a parabolic shape with change in V_{f2}. Fitting curve has been added for ease of reading.

Figure (3.19) shows the effective focal spot area as a function of the Focus2 potential. The plot shows the behavior at three different Focus1 voltages: 800V, 900V and 1100V. It is clear that in the optimal range of operation, the focal spot is insensitive to the applied Focus1 potential but highly sensitive to the Focus2 potential. The curve is parabolic, showing an optimal region of operation where the FSS is the smallest. Since the effective focal spot area is insensitive to V_{f1}, that gives a broad region of operation to maintain the same focal spot area just by tuning the focusing potentials.

Table (3.3) shows the measured FSS (long x short) for different combination of focusing potentials. The column on the left shows the F1 potential and the top row shows the F2 potential. Different combination of focusing voltages, gives different FSS. However, there is an optimal combination where the smallest FSS can be achieved. The measurements were done at 40KV anode potential with an anode tilt angle of 12º. The gate potential was 1260V with an emission cathode current of about 0.2mA. A duty cycle of 50 % (0.2 f/s and 2.5 sec pulse width) was used for image acquisition. We can confirm from this table that the FSS is insensitive to the Focus1 voltage in the optimal region of operation. However it is highly sensitive to the top focusing electrode.

F1/F2	**1500**	**1600**	**1700**	**1800**	**1900**	**2000**
800	108*194	99*155	99*112	96*101	99*112	95*132
900	111*194	95*140	95*105	95*109	95*116	95*151
1000	127*202	111*135	103*104	107*104	103*124	109*163
1100	155*201	127*132	103*104	95*104	99*132	103*171
1200		151*147	134*109	111*109	103*140	116*186

Table 3.4: Summary of the typical variation of the focal spot size as a function of the applied potential for Focus1 and Focus2 electrodes for a 2.35 x 0.50 mm CNT cathode. The unit for the vertical and horizontal direction is micrometer. The experiment was done at 40KV anode voltage and 1260V gate voltage. The gate mesh used was a 1D linear tungsten mesh.

3.9.4 Effect of Gate Potential

An advantage of FEX is that one can operate at constant current (flux) mode by adjusting the gate voltage automatically to maintain constant current. The necessary gate voltage will gradually increase during the lifetime of the tube due to cathode degradation. Thus it is important to understand the FSS variation with gate voltage. Figure (3.20(a)) shows the effects of the gate potential on the focal spot size. The results show that the focal spot size is not significantly affected by the intrinsic cathode decay over time. It changes at a rate of $5x10^{-6}$ mm^2/V over a range of 530V of gate voltage. This is highly desirable to be able to maintain the same FSS over the lifetime of the source. Experimental measurements have confirmed this prediction and are summarized in Table (3.4). These results show that similar focal spot size can be maintained even when gate potential is increased over time to maintain the same cathode current. Furthermore, a slight change in FSS can be compensated for by tuning the focusing voltages.

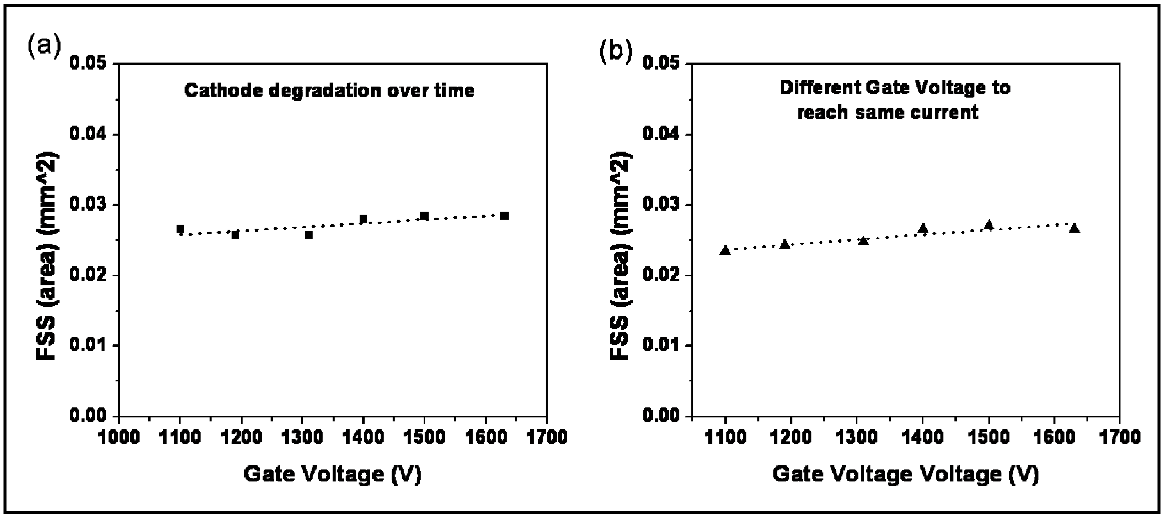

Figure 3.20: (a) Plot of FSS (area) as a function of gate voltage showing very small change in FSS with increase in gate voltage. This graph simulates the phenomenon of intrinsic cathode decay over time where the gate voltage needs to be adjusted to maintain the same current. (b) Similar plot showing small difference in FSS (area) for different gate voltage. This graph simulates the non-uniformity in cathode performance where different cathodes require different gate voltage to emit the same current.

Gate Potential (V)	**Focal Spot Size (μm)**	**Focal Area (μm^2)**
1100	**78 x 124**	**7596**
1190	**80 x 113**	**7100**
1630	**63 x 123**	**6086**

Table 3.5: Summary of the focal spot size and focal area as function of the gate potential. The experimental conditions are anode voltage 40 KV, Focus2 1300 V and middle Focus1 1400 V. The cathode current was 0.2mA.

A study was also performed to investigate the effect of different gate voltages on the FSS while maintaining the same current. This can be the case for different cathodes with non-uniform performance, where different gate voltage is required to achieve the same cathode current. Figure (3.20 (b)) show the plot of FSS for varying gate voltages keeping other parameters constant. The FSS is weakly dependent on the varying gate potential. This means even with non-uniform cathode performance with different cathodes we can achieve and maintain similar FSS over time.

An experimental verification of Case1 has been described here. A 2.35 x 0.50 mm CNT cathode was used to determine the focal spot size at two different current levels, 0.30mA and 1.00mA. Same experimental conditions were used except for varying the cathode currents. A duty cycle of 50 % (0.2 f/s and 2.5 sec pulse width), anode voltage of 40 KV and the gate voltage for a 0.30 and 1.00mA is 1160 and 1400 V, respectively. Table (3.5) and (3.6) show the focal spot measurements done at 0.3mA and 1mA cathode current. It can be inferred from the two tables that the minimum FSS does not change significantly. This is very crucial for medical applications where the CNT micro focus tube can operate at different current levels without affecting the focal spot size.

Middle/Top Electrode (V)	1400	1500	1600	1700	1800	1900
1400	80 x 163	100 x 117	107 x 137	107 x 130	100 x 162	113 x 188
1500	80 x 155	87 x 97	107 x 130	114 x 136	107 x 162	107 x 194
1600	93 x 163	87 x 111	87 x 111	100 x 144	113 x 176	107 x 214
1700	87 x 163	86 x 117	87 x 110	87 x 130	107 x 183	107 x 208
1800	93 x 169	94 x 124	93 x 104	87 x 130	100 x 162	114 x 220
1900	93 x 160	86 x 124	90 x 110	87 x 123	93 x170	114 x 214
2000	93 x 170	86 x 124	94 x 111	87 x 137	93 x 162	107 x 216

Table 3.6 Summary of the typical variation of the focal spot size as function of the applied potential for the focusing electrodes for a 2.35 x 0.50 mm CNT cathode at a current of 0.30 mA. The unit for the vertical and horizontal direction is μm.

Middle/Top Electrode (V)	1400	1500	1600	1700	1800	1900
1400	94 x 183	100 x 136	120 x 130	120 x 130	114 x 150	114 x 181
1500	94 x 196	94 x 124	107 x 124	120 x 144	120 x 155	114 x 196
1600	93 x 195	94 x 123	87 x 111	114 x 123	106 x 170	127 x 201
1700	100 x 201	93 x 137	94 x 104	87 x 124	100 x 176	120 x 208
1800	107 x 201	87 x 137	87 x 117	87 x 124	93 x 156	114 x 215
1900	100 x 215	87 x 144	86 x 117	86 x 124	87 x 163	120 x 207
2000	107 x 203	94 x 136	86 x 110	87 x 130	94 x 156	100 x 202

Table 3.7 Summary of the typical variation of the focal spot size as function of the applied potential for the focusing electrodes for a 2.35 x 0.50 mm CNT cathode at a current of 1.00 mA. The unit for the vertical and horizontal direction is μm.

3.4 Dynamic Micro-CT Scanner Developed At UNC

The performance of the CNT based micro-focus x-ray tube has been demonstrated in a dynamic micro-CT scanner developed at UNC called “Charybdis” [11,4]. As seen in Figure (3.21) it consists of a flat panel detector, a rotating gantry with the CNT x-ray micro-focus tube mounted on it and a mouse bed. The system provides high spatial (≤100μm) and temporal (10-20msec) resolutions with gating capability. In a typical CT scan, 400 projections are acquired over a circular orbit of 199.5° with a stepping angle of 0.5°. Figure (3.21 (b & c)) shows reconstructed slices of a cardiac gated mouse using Charybdis.

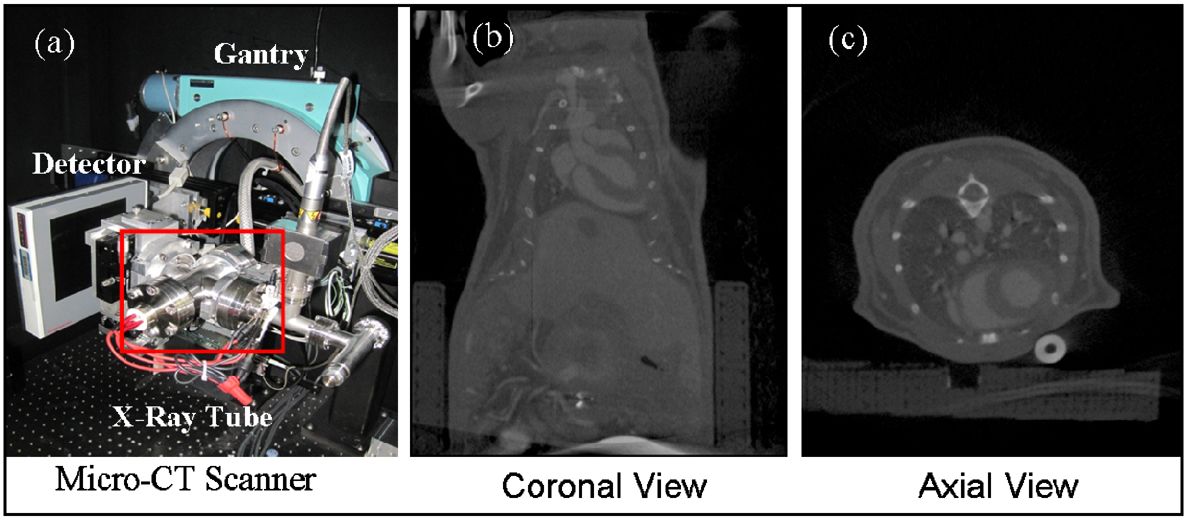

Figure 3.21 (a) Picture of a dynamic micro-CT scanner developed at UNC. It has a CNT micro-focus x-ray tube, a detector, a sample stage and a rotating gantry. The x-ray tube and the detector are mounted on the gantry and can rotate around the sample during imaging. (b) Representative image slice of a mouse heart using a CNT micro-CT scanner. Imaging was done at 50kVp and 3mA cathode current. Reconstructed images are the courtesy of Laurel Burk. For further detail for micro-CT imagine, see [11].

3.5 Stationary Micro-CT System Based On Multi-Beam FEX

Furthermore, this tube design can be translated into a multi-beam field emission x-ray (MBFEX) source array arranged in a linear or non-linear manner with a pitch of 5mm for individual beam units. A MBFEX is capable of generating x-ray pulses from multiple viewing angles without any associated mechanical motion of the source. The x-ray pulses can be generated sequentially or in a multiplexed manner leading to a dramatic reduction in data acquisition time. The elimination of the source motion eliminates any focal spot blur associated with it and the short scan time reduces motion blur due to patient movement. Thus MBFEX has the potential to improve the image quality. Such a source array can be integrated into a “stationary” CT [12,13] or tomosynthesis [14,15] configuration. The concept of non-rotating gantry with spatially distributed x-ray source dates back to the 1970s with the development of the Dynamic Spatial Reconstructor (DSR) [16]. The electron beam computed tomographic system (EBCT)[17] and scanning-beam digital x-ray system[18] came later. However, limited viewing angle, size and maintenance issues led to the demise of these systems. CNT based MBFEX can overcome most of these limitations.

At UNC we have studied the feasibility of integrating this MBFEX into a stationary micro-CT configuration. An ideal stationary micro-CT system would have a circular geometry with zero missing data such as schematically represented in Figure (3.22). This would require ring geometry with cathodes along the tract with corresponding detectors. This geometry would give high resolution images with no missing data and no motion blur. In theory image acquisition time would reduce dramatically due to elimination of any mechanical motion. However, building such a system would cause innumerable engineering challenges, not to mention the amount of resources and funding required. Hence, two alternative configurations have been studied to build a stationary micro-CT system and have been described in the following paragraphs.

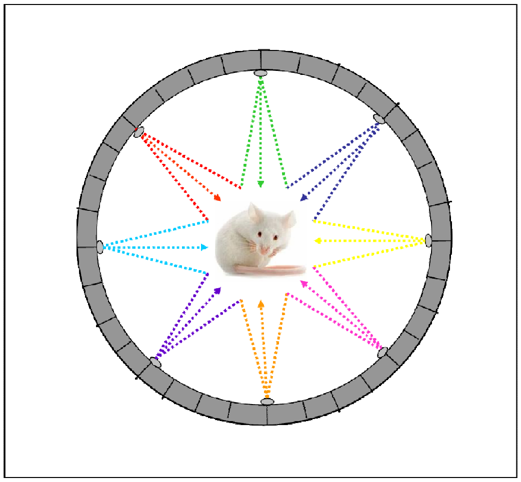

Figure 3.22: Schematic representation of an ideal stationary micro-CT system with no missing data.

Stationary Micro-CT System with Linear X-Ray Source Array

A hexagonal configuration with three detectors and three source arrays has been studied here. The overview of the system design has been shown in Figure (3.23). Each source array is comprised of 20 spatially distributed individual beams arranged in a linear manner. A segment of this entire configuration has been built for initial study.

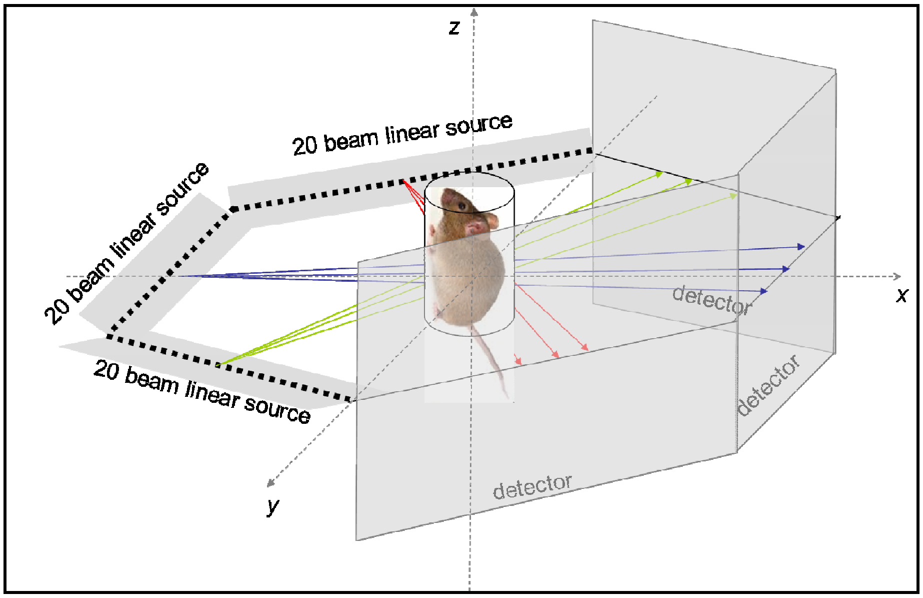

Figure 3.23: Overview of a stationary micro-CT system with hexagonal configuration comprising of three detectors and three source array. Each source array is comprised of 20 spatially distributed beams arranged in a linear manner.

As mentioned earlier the source comprises of 20 discrete CNT based field emission cathodes arranged in a linear array on a single glass piece (shown in Figure (3.24 (d)) with individual control for each cathode. [19,12]. The entire cathode-anode assembly with the focusing structure can be seen in Figure (3.24 (c)). The stationary micro-CT scanner can capture up to 20 projection images from different viewing angles without any mechanical motion of the system. After one linear scan of the 20 beams the object needs to be rotated in steps of 36º till it covers the entire 360º. The entire 360º scan can be completed in 10 steps. Figure (3.24(a)) shows a schematic diagram of the setup. The picture in the right shows the prototype scanner built at UNC. Some preliminary FSS measurement results are shown in Figure (3.24).

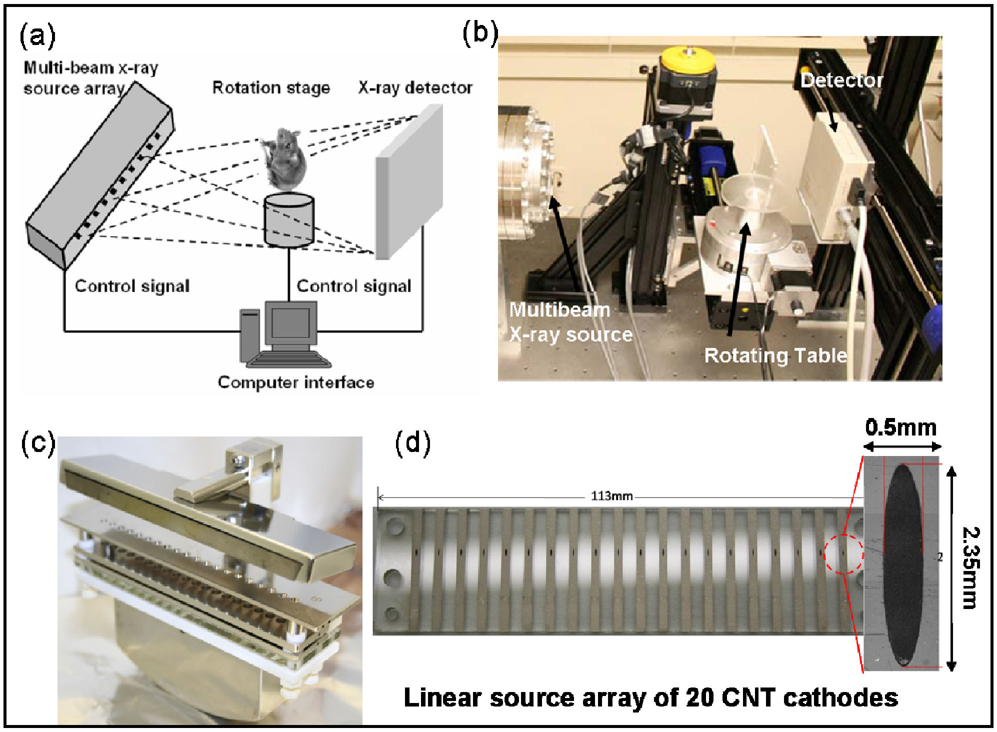

Figure 3.24: (a) Schematic drawing of the MBμCT system with a multi-beam x-ray source array, rotation stage, x-ray detector and corresponding computer interface. (b) The overview of the prototype MBμCT system developed at UNC. Picture reproduced from reference [19] (c) Actual in-chamber components of the entire cathode assembly (d) a single glass piece with 20 individual CNT cathodes arranged in a linear array.

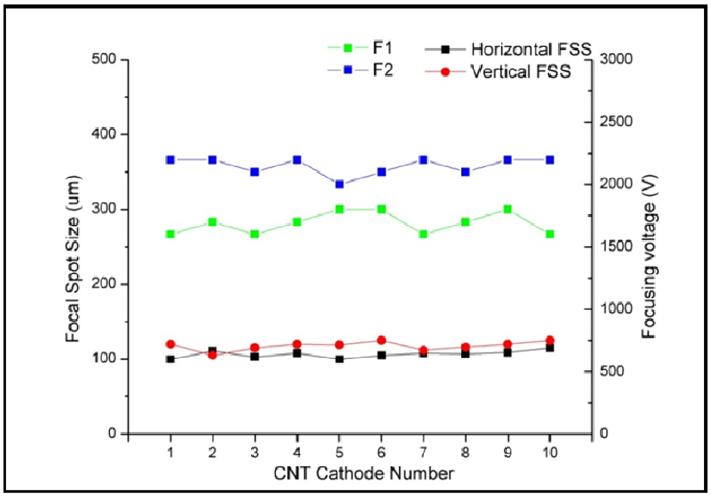

Figure 3.25: FSS for 10 different cathodes measured in the prototype 20beam x-ray source.

Stationary Micro-CT Scanner with Non-linear x-ray source array

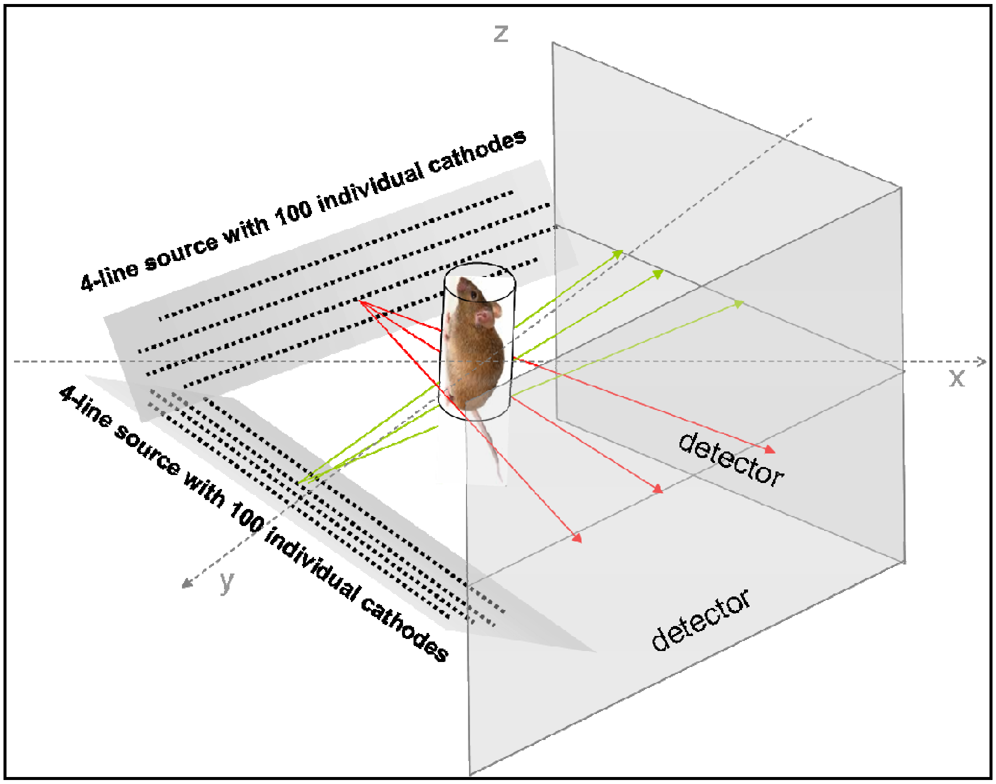

Figure 3.26: Overview of a stationary micro-CT system with square geometry. It consists of 2 detectors and 2 source array. Each source array has 100 individual beams arranged in four rows of 25 beams non-linearly distributed.

The second configuration studied is a square geometry stationary micro-CT system with non-linear source array. The system overview can be seen in Figure (3.25). It comprises of two source array and two detectors. Each source array has 100 individual beams arranged in four rows of 25 beams. The rows are non-linearly spaced. This is a very compact design as can be seen from the overview. A prototype system with a section of this configuration comprising of 26 beams was built for initial testing. This was built at Xintek Inc. Nanotechnology Innovations in collaboration with UNC and NCSU. The overview of the prototype configuration is shown in Figure (3.26 (a) and (b)). (d) Shows the actual cathode with 26 individual CNT cathodes deposited on a single glass piece. The entire cathode-anode assembly with the focusing structure can be seen in (c). This prototype has been successfully built and tested with some initial phantom imaging.

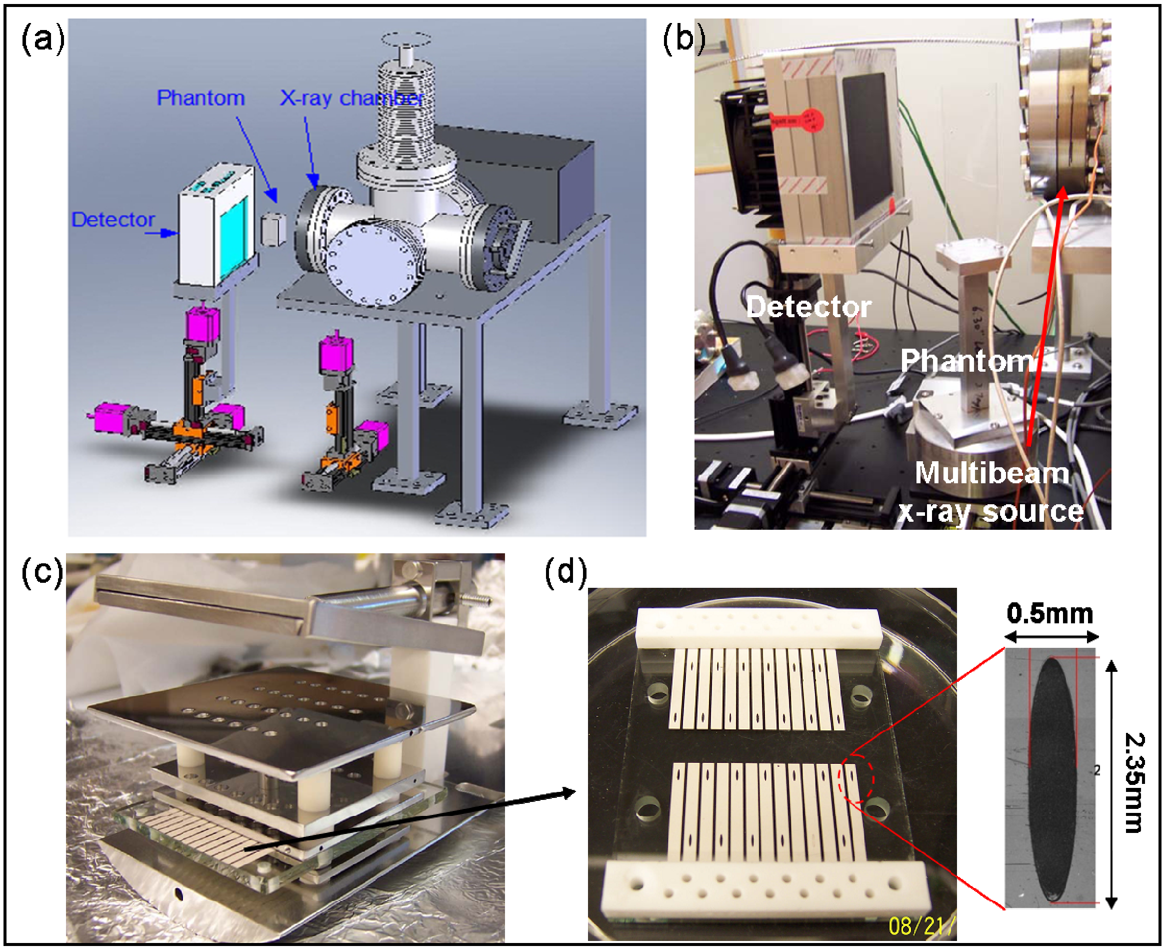

Figure 3.27: (a) Schematic drawing of the stationary micro-CT system with a multi-beam field emission x-ray source, rotation stage and x-ray detector. (b) The overview of the prototype system developed at Xintek Inc. (c) Actual in-chamber components of the entire cathode-anode assembly. (d) A single glass piece with 26 individual CNT cathodes arranged in a non- linear array. Pictures courtesy of Dr. Peng Wang.

3.6 Summary

A CNT based field emission micro-focus x-ray source has been designed and developed. One of the primary characteristic of an x-ray source is its spatial resolution, which is determined by the focal spot size of the electron beam. Hence, a systematic study of different factors affecting the focal spot size has been conducted. We see that the focal spot size is highly sensitive to Focus2 voltage and virtually insensitive to Focus1 voltage. In addition it is not much dependent on the gate extraction voltage which is a big advantage especially for medical imaging where the dose needs to be varied for patients of different size. This means that a constant focal spot size can be maintained over the lifetime of the x-ray source even when the gate extraction voltage needs to be adjusted owing to cathode degradation over time. Extensive electron optics simulations have been performed to fully characterize the micro-focus tube. An isotropic 100μm focal spot size can be easily achieved using this tube design. Further more, the cathode size can be varied to get a variable focal spot size with the smallest ~50μm. A prototype micro-focus tube was built in the laboratory for initial testing. Experimental measurements confirm the predicted simulated results.

Application of such a CNT based field emission micro-focus tube has been demonstrated in the field of medical imaging. A dynamic micro-CT scanner has been successfully built with the micro-focus tube mounted as the x-ray source. The micro-CT scanner has demonstrated capabilities of gated imaging of the heart and lung of a mouse. In addition, a spatially distributed Stationary Multi-beam micro-CT scanner has also been built using the micro-focus tube design. This technique has the potential to improve the image quality in addition to facilitate short scanning time. In conclusion a CNT field emission micro-focus tube has been successfully designed and characterized. The versatility of the tube design has been demonstrated through the translation of the design to real life medical imaging devices.

References

[1] C.L. Morgan, Basic principles of computed tomography. 1983, Baltimore: University park press.

[2] Jerry L. Prince and Jonathan M. Links, “Medical Imaging; Signals and Processing”, Pearson Prentice Hall Bioengineering.

[3] J. Zhang,Y. Cheng, Y. Z. Lee, B. Gao and Q. Qiu, W. L. Lin, D. Lalush,J. P. Lu and O. Zhou, “A nanotube-based field emission x-ray source for microcomputed tomography”, Review of Scientific Instruments, **76**, 094301, 2005.

[4] Cao, G., Calderon-Colon, X., Wang, P., Burk, L., Lee, Y.Z., Rajaram, R., Sultana, S., Lalush, D.S., Lu, J.P., and Zhou, O., “A dynamic micro-CT scanner with a stationary mouse bed using a compact carbon nanotube field emission x-ray tube”, Proc of SPIE Vol. 7258, 72585Q-1-72585Q-17, 2009.

[5] Liu, Z., Zhang, J., Yang, G., Cheng, Y., Zhou, O., and Lu, J.P., "Development of a carbon nanotube based microfocus x-ray tube with single focusing electrode", Review of Scientific Instruments, 77, 054302, May 2006.

[6] Liu, Z., Yang, G., Lee, Y.Z., Bordelon, D., Lu, J.P., Zhou, O., "Carbon Nanotube Based Micro-Focus Field Emission X-ray Source for Micro-Computed Tomography", Applied Physics Letters 89, 103111, 2006.

[7] Cheng, Y., Zhang, J., Lee, Y. Z., Gao, B., Dike, S., Lin, W., Lu, J. P., and Zhou, O., “Dynamic radiography using a carbon-nanotube-based field-emission x-ray source”, Review of Scientific Instruments, 75(10), 3264-3267, 2004.

[8] Calderon-Colon, X., Geng, H., Gao, B., An, L., Cao, G., and Zhou, O., "A carbon nanotube field emission cathode with high current density and long-term stability", Nanotechnology 20, 325707, 2009.

[9] Zhang, J., Yang, G., Rajaram, R., Guan, E., Lee, Y.Z., Lalush, D.S., Chang, S., Lu, J.P., Zhou, O**.,** "A stationary scanning X-ay imaging system based on carbon nanotube field emitters", Medical Physics 33 (6): 2159, June 2006.

[10] European Committee for Standardization EN 12654-5, 1999.

[11] Cao, G., Lee, Y.Z., Peng, R, Liu, Z, Rajaram, R., Calderon-Colon, X., An, L., Wang, P., Phan, T., Sultana, S., Lalush, D. S., Lu, J.P., and Zhou, O**.,** "A dynamic micro-CT scanner based on a carbon nanotube field emission x-ray source**"**, Phys. Med. Biol. 54, 2323-2340, 2009.

---

[12] R. Peng, J. Zhang, X. Calderon-Colon, S. Wang, S. Sultana, P.Wang, G. Yang, S. Chang, J. Lu, and O. Zhou, “Design, optimization and testing of a multi-beam micro-CT scanner based on multi-beam field emission x-ray technology”, SPIE Medical Imaging, 7622, 2010.

[13] J. Zhang, R. Peng, S. Chang, J.P. Lu, and O. Zhou, “Imaging quality assessment of multiplexing x-ray radiography based on multibeam x-ray source technology”, SPIE Medical Imaging, 7622, 2010.

[14] Guang Yang, Ramya Rajaram, Guohua Cao, Shabana Sultana, Zhijun Liu, David Lalush, Jianping Lu, Otto Zhou, “Stationary digital breast tomosynthesis system with a multi-beam field emission x-ray source array”, Proc. of SPIE Vol. 6913, 69131A, 2008.

[15] X. Qian, R. Rajaram, X.Calderon-Colon, G.Yang, T. Phan, D. Lalush, JP. Lu, and O. Zhou, “Design and characterization of a spatially distributed multibeam field emission x-ray source for stationary digital breast tomosynthesis”, Medical Physics,36,10, October 2009.

[16] RA Bobb, EA Hoffman, L.J. Sinak, L.D. Harris, and E.L. Ritman, Proc. Of the IEEE 71(3), 1983.

[17] MJ Lipton, CB Higgins, D farmer, and DP Boyd, Radiology 152(3): 579-582, 1984.

[18] MA. Speidel, B P. Wilfley, J M. Star-Lack, and JA. Heanue, and MS. Van Lysel, Med. Phys. 33(8), 2006.

[19] R. Peng, J. Zhang, X. Calderon-Colon, S. Wang, S. Sultana, P.Wang, G. Yang, S. Chang, J. Lu, and O. Zhou, “Design, optimization and testing of a multi-beam micro-CT scanner based on multi-beam field emission x-ray technology”, Proc of SPIE Vol. 7258, 72585Q-1-72585Q-17, 2009.

Chapter 4 : CNT based X-Ray Source Design for Stationary Digital Breast Tomosynthesis (sDBT) System

4.1 Introduction

According to the National Cancer Institute (NCI), breast cancer is the second most common cancer in women in the United States. 192,370 new cases of breast cancer in women were reported in 2009 of which 40,170 were fatal [1]. The NCI also estimates that 12.7% of women born today will be diagnosed with breast cancer at some point of their lives.

A large amount of resources has been commissioned for breast cancer research to find ways to prevent and cure it. Despite a long-term increase in the incidence of breast cancer, data from the Surveillance, Epidemiology and End Results (SEER) Program show a decrease in breast cancer mortality rate of 2.3% per year from 1990 to 2001 [2]. The increased incidence of breast cancer is due to the widespread availability of screening mammography. Other forms of screening include breast self-exam, clinical breast exam, ultrasonography and magnetic resonance imaging, but x-ray mammograms continue to be the most widely used and cost-effective way to screen for cancer.

Mammography can identify cancers that are too small to find by physical examination in addition to finding ductal carcinoma *in situ* which is a non-invasive condition. Mammography uses x-rays to obtain images of the compressed breast on either an x-ray film or a digital detector. Although screening mammography is widely accepted around the world for early breast cancer detection, it is not 100% accurate. This is mainly due to the fact that it is a two dimensional imaging modality that tries to image a three dimensional breast. It is possible that some lesions might be obscured by over and underlying normal tissue especially in the case of radio-dense breasts. In addition, in conventional mammograms, depth information about the lesions is not made available [3,4].

The limitations of the conventional x-ray mammography modality led to the development of tomographic imaging of the breast. In standard tomographic imaging, the x-ray tube and the detector move synchronously around the object of interest on opposite sides to obtain multiple projection images. These projection images are used to develop reconstructed images which show specific planes of interest throughout the object body. One primary advantage of tomographic imaging is its capability to provide depth information. It improves the conspicuity of features by removing overlapping tissues. It can also improve local contrast by restricting the dynamic range to a single slice. Tomographic imaging of the breast can be done using either a dedicated breast computed tomography (DBCT) system or a digital breast tomosynthesis system.

Soon after the advent of the CT technology, the concept of dedicated breast CT (DBCT) started. DBCT is considered better than projection mammography since it has the potential to eliminate overlapping structures [5]. Typically in DBCT, 300-500 images of the breast are taken as the scanner rotates 360° which are then reconstructed to obtain three dimensional slices through the breast. However, the first clinical experience [6] showed the technology does have some limitations. The first study failed to visualize micro-calcifications. Also with 500 or more projection images the dose was definitely an issue. In addition DBCT had limited efficiency in imaging the chest wall. In conclusion, DBCT has the potential; however, improvements and modification are necessary to overcome the present limitations.

4.2 Digital Breast Tomosynthesis (DBT)

Digital breast tomosynthesis (DBT) is a limited angle tomography technique that takes a number of low dose projection images over a certain angular range. The total dose is still comparable to conventional two-view mammography. These projection images are then used to obtain three dimensional reconstructed images of the breast. The reconstructed dataset consists of slices that are relatively free of tissue clutter compared to a standard mammogram. This technique reduces a major limitation of tissue overlap in conventional mammograms. The geometry of a DBT system is shown in Figure (4.1). Different groups have developed their own reconstruction algorithms to allow image reconstruction for the limited angle tomosynthesis geometry. Most of the current DBT systems use a stationary detector and a movable x-ray source.

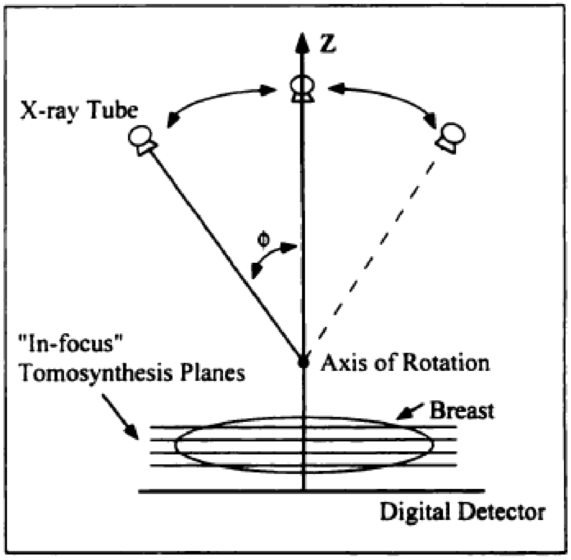

Figure 4.1: Schematic representation of a DBT system configuration [7].

4.3 Current DBT Scanners and their Limitations

There are currently at least three tomosynthesis systems under development by major medical technology companies. These include the Senographe 2000D from General Electric (GE) [8], the Mammomat Novation 9 from Siemens [9] and Selenia from Hologic [10]. All these systems are modified full field digital mammography systems and use a rotating gantry technique. The gantry with the x-ray source moves about 15° to 50° around the patient while acquiring 11 to 49 projection views of the breast which are then reconstructed using different algorithms. The resultant depth resolution is about 1mm while the in-plane resolution is between 100 and 150 μm. GE uses the step-and-shoot technique wherein the gantry containing the x-ray source makes a full stop at each projection angle to obtain an image before moving on to the next view. Hologic and Siemens use the continuous rotation technique wherein the gantry keeps moving continuously, albeit slowly, so that x-ray images of the patient are acquired at each projection angle even while the source is moving.

It is evident from published work that DBT is a potential alternative to conventional mammography. However, it must be noted that the systems from all the three leading manufacturers demonstrate an imaging time of about 7 to 40s. This is much longer compared to 1s imaging time for conventional mammography. A longer scan time leads to image degradation since it introduces blur from patient motion. Also, any kind of gantry movement leads to effective focal spot enlargement, thus affecting the image quality [10].

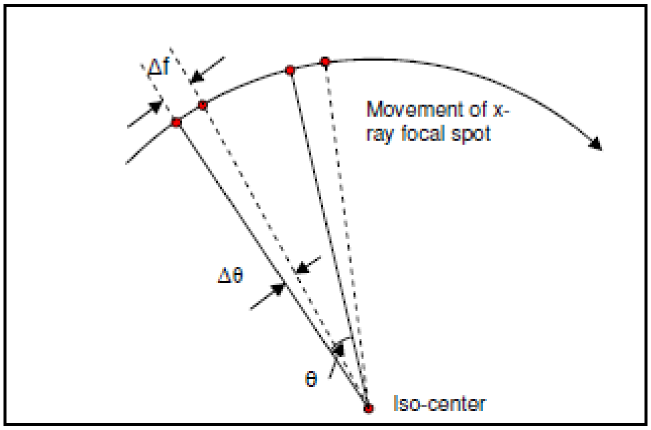

Figure 4.2: Schematic of the focal spot enlargement of continuous rotation mode. The gantry rotates angle θ between two imaging positions. During the x-ray radiation period, the gantry rotates angle Δθ and moves Δf along the arc. Δf is the additional x-ray focal spot size induced by gantry rotation. The value is determined by the x-ray radiation period and gantry rotation speed. For a typical scan, θ=3°, Δθ=0.12°, and Δf=1mm [11].

This phenomenon has been schematically explained in Figure (4.2). This means DBT can be a potential alternative to conventional mammography if the current system configuration can be improved. One possibility is to reduce the scan time, hence reduce the time during which the patient has to endure compression pain as well as reduce patient motion blur. This can be achieved by integrating a fast rotating gantry, but that makes it an expensive ordeal, not to mention significant enlargement of the focal spot size. The other approach is a non-rotating gantry with distributed x-ray source. This was tried at Mayo clinic using the Dynamic Spatial reconstructor [12] but it was not successful because of cost, size and maintenance issues. Other techniques, such as electron beam computed tomographic system [13] and scanning-beam digital x-ray system [14] were proposed. But such systems tended to be cumbersome and generally had limited angular coverage.

This led to the development of a spatially distributed multi-beam carbon nanotube (CNT) based field emission x-ray source for stationary DBT system in our laboratory at UNC. The system comprises of multiple individual emitters with independent electronic controls housed in a single vacuum chamber. This eliminates any delay between consecutive exposures involving gantry motion and is limited only by the detector readout time which results in reduction in total imaging time. The image quality is much improved because there is no mechanical motion or vibration (elimination of focal spot blur), and scan time is shorter (less blur due to patient movement). In addition, the elimination of moving parts makes the system design much simpler and compact. The first generation stationary DBT (s-DBT) system that has been developed in our laboratory is called Argus and from the table listed below it is clear that a stationary source definitely has its own advantage.

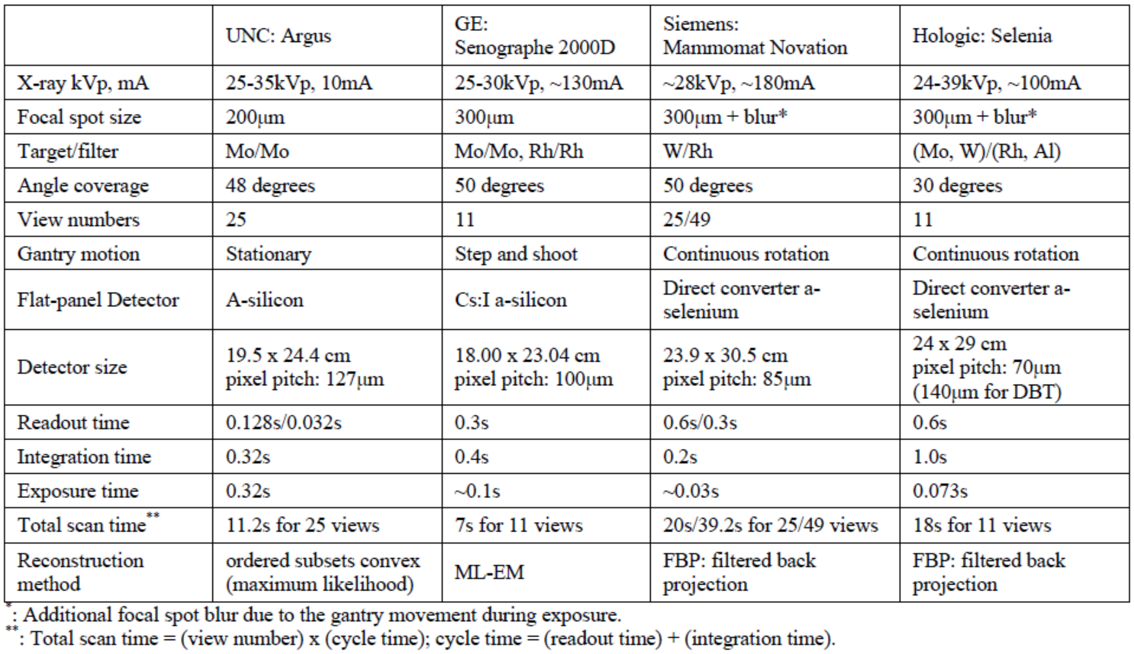

	UNC: Argus	GE: Senographe 2000D	Siemens: Mammomat Novation	Hologic: Selenia
X-ray kVp, mA	25-35kVp, 10mA	25-30kVp, ~130mA	~28kVp, ~180mA	24-39kVp, ~100mA
Focal spot size	200μm	300μm	300μm + blur[*]	300μm + blur[*]
Target/filter	Mo/Mo	Mo/Mo, Rh/Rh	W/Rh	(Mo, W)/(Rh, Al)
Angle coverage	48 degrees	50 degrees	50 degrees	30 degrees
View numbers	25	11	25/49	11
Gantry motion	Stationary	Step and shoot	Continuous rotation	Continuous rotation
Flat-panel Detector	A-silicon	Cs:I a-silicon	Direct converter a-selenium	Direct converter a-selenium
Detector size	19.5 x 24.4 cm pixel pitch: 127μm	18.00 x 23.04 cm pixel pitch: 100μm	23.9 x 30.5 cm pixel pitch: 85μm	24 x 29 cm pixel pitch: 70μm (140μm for DBT)
Readout time	0.128s/0.032s	0.3s	0.6s/0.3s	0.6s
Integration time	0.32s	0.4s	0.2s	1.0s
Exposure time	0.32s	~0.1s	~0.03s	0.073s
Total scan time[**]	11.2s for 25 views	7s for 11 views	20s/39.2s for 25/49 views	18s for 11 views
Reconstruction method	ordered subsets convex (maximum likelihood)	ML-EM	FBP: filtered back projection	FBP: filtered back projection

[*]: Additional focal spot blur due to the gantry movement during exposure.
[**]: Total scan time = (view number) x (cycle time); cycle time = (readout time) + (integration time).

Table 4.1: Comparison of the three tomosynthesis scanners being developed by major companies. Table reproduced from [11 Error! Bookmark not defined.Error! Bookmark not defined.**].**

4.4 Stationary DBT System developed at UNC

Figure (4.3(a)) gives an overview of the stationary full field DBT system Argus, comprising of a linear 25 beam source array based on CNT cathodes. The system geometry is comparable to regular mammography devices. A picture of the prototype tube with the detector and a breast phantom can be seen in Figure (4.3(b)). The flat panel detector used is Varian Paxscan 2520 with field of view19.5cm x 24.4cm. This ensures the capability of full field mammography. The distance between the phantom and the x-ray source is 64.52cm, which is comparable to other regular mammography devices. The x-ray sources are placed linearly for design simplicity with even angle distribution. The increment is 2° which gives 48° total angular coverage. The designed power output is 10mA per source. With the elimination of gantry rotation, the total imaging time is less then 9 seconds with a total x-ray flux of 80mAs when the detector is operated at 2x2 binning mode [11,15].

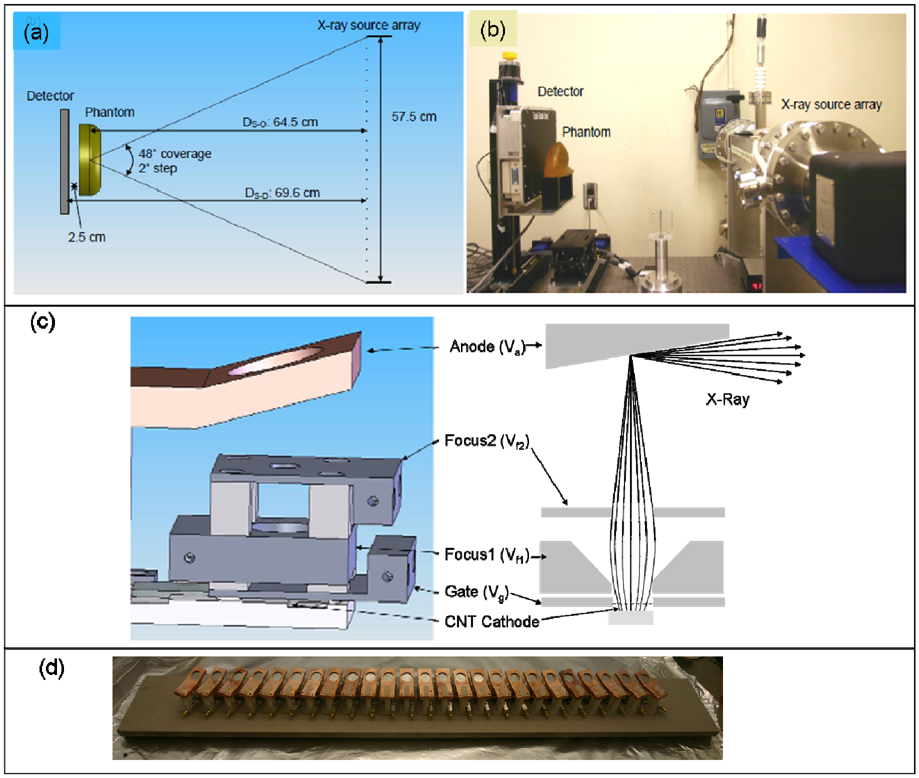

Figure 4.3: (a) Overview of the Argus system geometry with a source array of 25 individual CNT cathodes. (b) Picture of the actual system with the detector and a breast phantom. (c) Schematic representation of a single cathode-anode assembly with the detailed focusing structure. (d) Picture of the linear source array with 25 individual x-ray units [13].

The x-ray source is an integral part of the s-DBT system and has some detailed description here. The x-ray source design is primarily based on the micro-CT x-ray source geometry developed in our group previously. An individual source unit has been translated to a spatially distributed multi-beam source array. Each x-ray source unit consists of a CNT cathode, a gate electrode, a focusing unit and an anode with 16° take-off angle. The cathode is fabricated on a Si wafer with an elliptical emission area of 2.5mm by 0.72mm. The gate electrode has a tungsten woven mesh attached at the bottom for the extraction of the electrons. The focusing unit consists of 2 metal diaphragms based on Einzel-type lens to focus the beam to a finite point on the anode. Figure (4.3 (c)) shows a detailed drawing of an individual unit followed by a picture of the complete source array.

Each beam can achieve an isotropic focal spot size (FSS) of 190µm which has the potential for high spatial resolution. However, due to small cathode size and electronic limitations the current was only limited to 4mA which prolonged the scan time to achieve the target dose. Long time also means additional motion blur from patient movement and henceforth image quality degradation. This was a major limitation of this system. The prototype system Argus proved the feasibility of developing a stationary DBT system; however, it left room for further improvement.

In the meantime, a fixed gantry tomosynthesis system for image guided radio therapy was built by a group from Siemens Healthcare [16,17]. It consists of 52 sources that are arranged in a rectilinear array and operates at 80–160 kVp. In this case, the source comprises of CNT field emitters, a passive focusing system and a target anode. The passive focusing structure limits the focal spot size to 1.7mmx2mm. This is a pretty large beam size even though the tube current is not an issue. Figure (4.4) shows an image of the tube with 52 sources.

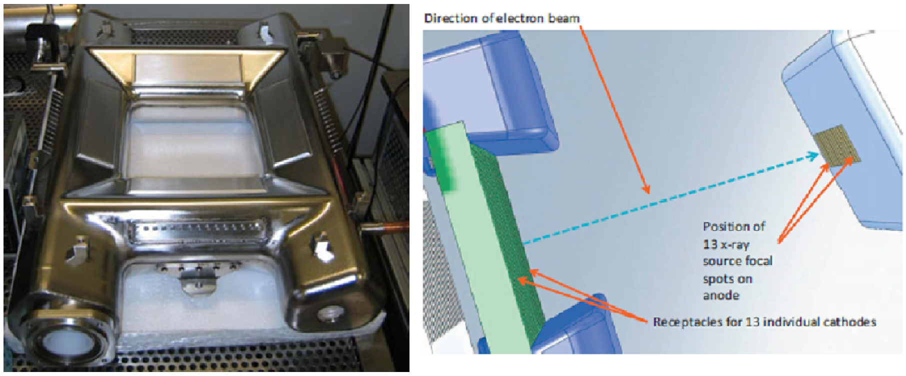

Figure 4.4: Square 52 emitter source array for IGRT (left). The cathode array facing the elongated anode shown in the tube geometry (right) [Error! Bookmark not defined.Error! Bookmark not defined.**].**

A feasibility study using this scanner showed that the focal spot blur was indeed eliminated using the stationary system. A breast phantom was imaged using DBT and stationary DBT scanners and looking at the line profiles along the direction of rotation clearly shows a much sharp peak with small distribution as shows in Figure (4.5).

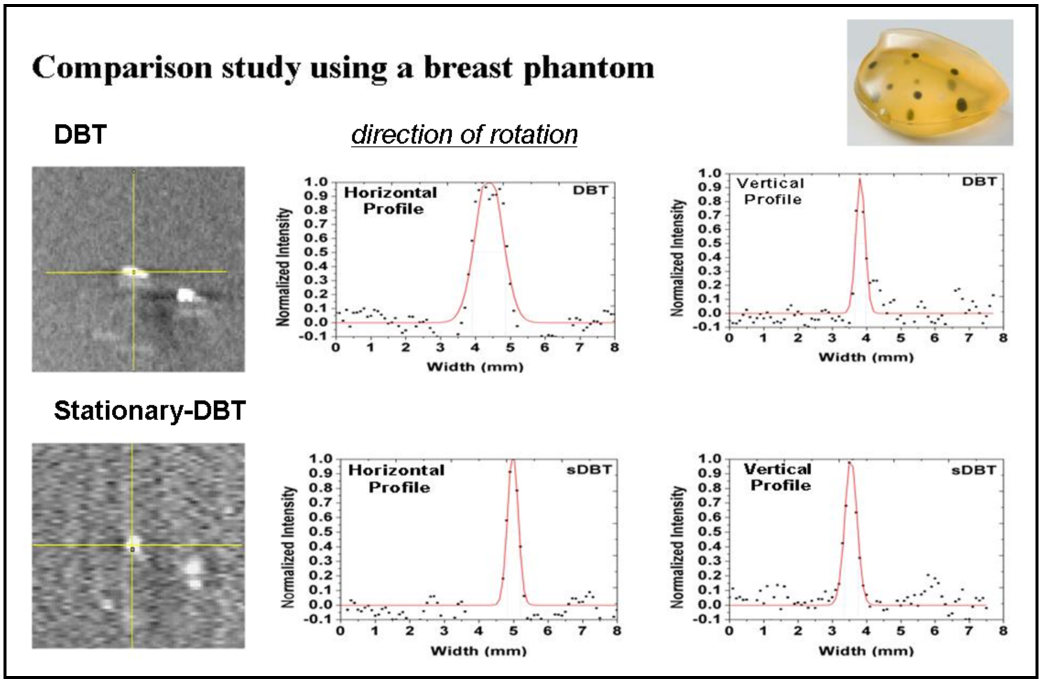

Figure 4.5: Feasibility study of elimination of focal spot blur along the direction of source rotation. A breast phantom was imaged using a DBT scanner and a stationary DBT scanner. The sharp peak with narrow distribution in the second case confirms that focal spot blur can indeed be eliminated using this stationary configuration (reproduced from http://www.physics.unc.edu/project/zhou/images/Images_2010/Comparison%20study%20using%20a%20breast%20phantom.jpg).

4.5 Motivation for High Power Stationary DBT Scanner

While Argus proved the feasibility of developing an s-DBT system, its low current proved to be a major limitation. However, the Siemens system for IGRT proved the possibility of achieving high current with a large cathode size. Equipped with this new knowledge we ventured into designing and developing a high power multi-beam x-ray source (named Argus3) which can be successfully integrated into an s-DBT system. One of the primary goals of this new system is to achieve short scan time of 4s (current DBT systems have a scan time ranging between 7s to 40s which mean the patient has to endure discomfort for that long) while maintaining 100mAs dose, which is comparable to conventional mammography. To achieve short scan time, high flux is required, which means a large cathode emission area is needed to generate high current. However, a large cathode might give a large FSS, which might degrade the image quality. To avoid such a possibility, an effective focusing structure is needed which can focus a large emission area into a small x-ray beam. This brings us to the motivation behind this research. Extensive electron optics simulations have been done to design and characterize a source unit that can meet the demands of a high power x-ray source without compromising the spatial resolution (target FSS is 0.3x0.5mm (long x short)). Details of the simulation study have been reported in the rest of the chapter with some initial test results.

4.6 System Overview

Argus3 is designed to be a stationary full field DBT with spatially distributed sources based on CNT field emission technology. The whole scanner is composed of a 31 x-ray source array, a flat panel x-ray detector (from Hologic Inc.), and a control station for synchronizing the source and detector, and also image acquisition. The overall geometry is shown in the Figure (4.5). The detector has a field of view of 29cmx24cm. The distance between the phantom and the x-ray source array is 65cm which is also the common iso-centre of the source array. The distance between the phantom and the detector is 5cm. The x-ray sources have even-angle distribution with 1° increment which gives 30° total angular coverage. This translates to a distance of 1.2cm between the adjacent x-ray sources. The 31 beams provide system flexibility such as one can use 31 beams to cover 30º in 1º step or 2º step (using 15 alternate beams). One can also cover only 15º using the central 15 beams [18].

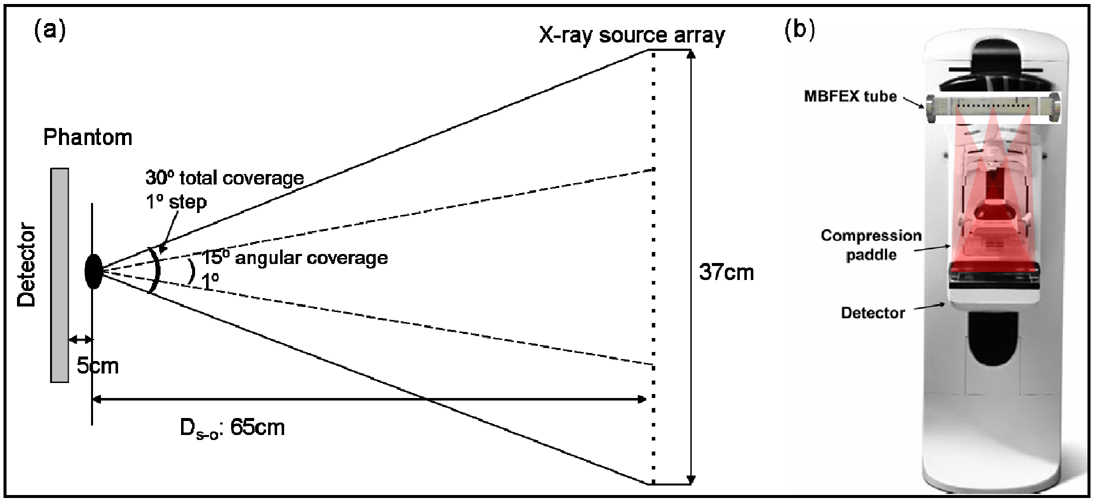

Figure 4.6: (a) Source array for Argus3. All x-ray sources are placed linearly with even angular spacing of 1degree which gives 30degree total angular coverage. The source to detector distance is chosen to be 70cm with the source iso-centre at 65cm from the source. (b) An overview of the multi-beam field emission x-ray (MBFEX) tube mounted with a compression pad and a detector.

4.7 Design of Individual X-Ray Source Unit

The x-ray source consists of 31 individual source units which are arranged in a linear array. Each source unit consists of a cathode made of CNT field emitters, a gate electrode for the extraction of the electrons from the emission surface, a focusing structure to get a small focal spot size (FSS) and a target (anode) for the x-ray generation. The entire unit is housed in a stainless steel chamber and is operated at high vacuum conditions.

4.7.1 Cathode Dimension and Performance

The first consideration was to determine the cathode current required per beam to get a total dose of 100mAs. The next step was to determine a cathode emission area which can deliver the high current of 40mA reliably in a stable manner. The detailed calculations have been shown in Figure (4.7).

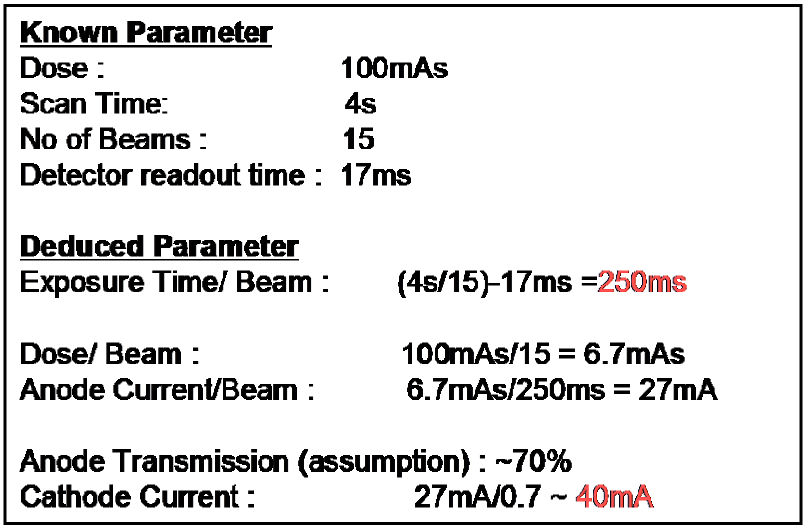

Known Parameter

Dose : 100mAs

Scan Time: 4s

No of Beams : 15

Detector readout time : 17ms

Deduced Parameter

Exposure Time/ Beam : (4s/15)-17ms =250ms

Dose/ Beam : 100mAs/15 = 6.7mAs

Anode Current/Beam : 6.7mAs/250ms = 27mA

Anode Transmission (assumption) : ~70%

Cathode Current : 27mA/0.7 ~ 40mA

Figure 4.7: Calculations showing exposure time and cathode current required to achieving 4s scan time using 15 beams.

From a previous study it has been confirmed that an elliptical cathode area of 2x8mm can reach 18mA cathode current in triode mode as seen in Figure (4.8 (a)) [15]. This was a clear indication that a much larger emission area is needed to achieve 27mA anode current. A CNT cathode of 2.5x13mm elliptical shape was determined after careful considerations. The performance of the cathode is shown in Figure (4.8) where an IV plot shows that the cathode can actually deliver high current. The stability of the cathode has been tested by performing a lifetime run for over 4000 min running at 250ms pulse width, 5s period at 40mA cathode current.

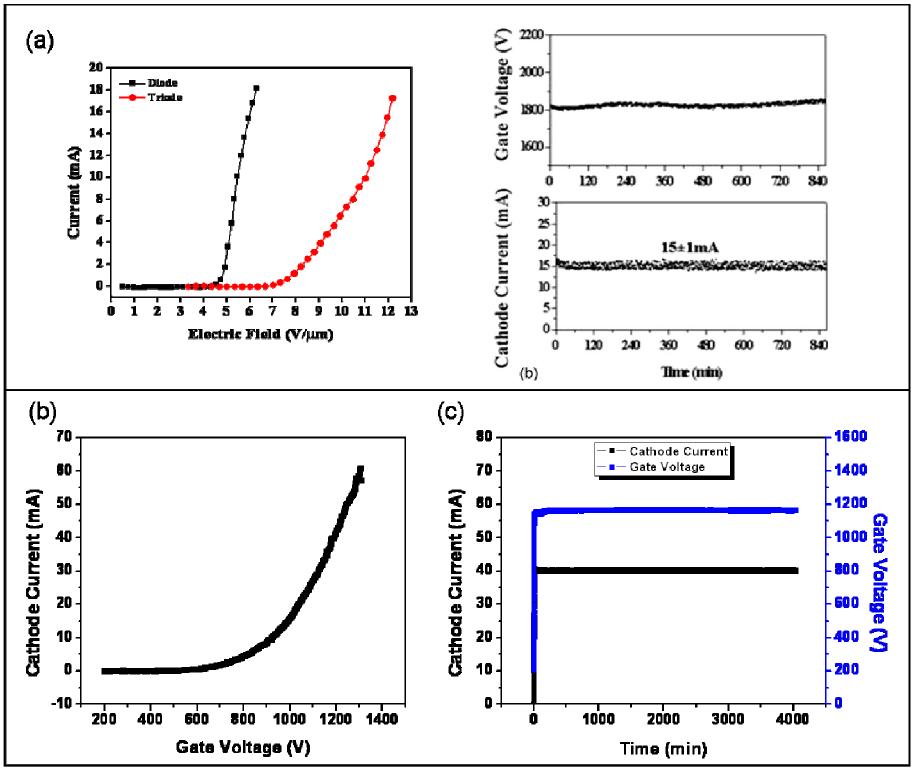

Figure 4.8: (a) Shown is the IV and lifetime plot of a 2x8mm cathode. The condition for the lifetime measurement is 10 ms pulse width, 1 Hz at 15mA.Image reproduced from [15]. (b) Shows the IV for a 2.5x13mm elliptical cathode in triode mode. (c) Exhibits the lifetime measurement for the same cathode shown in (b). The condition for the measurement is 250ms pulse width, 5s period at 40mA current.

4.7 Experimental Setup for Focal Spot Measurement

The FSS was measured based on the pinhole method [19].Figure (4.9(a)) shows the setup for the focal spot measurement. It consists of an x-ray source, a pinhole phantom and a detector all aligned such as the central beam of the x-ray source passes through the pinhole. Figure (4.9(b)) shows the actual module used for the FSS measurements. The image is then analyzed by performing a Gaussian fit to the intensity distribution and the focal spot size is determined at FWHM. A typical representation of the intensity distribution along the short axis of the cathode is shown in (d). This kind of single peak distribution is better for imaging in contrary to double peak distribution often seen in conventional sources which leads to deterioration of spatial resolution.

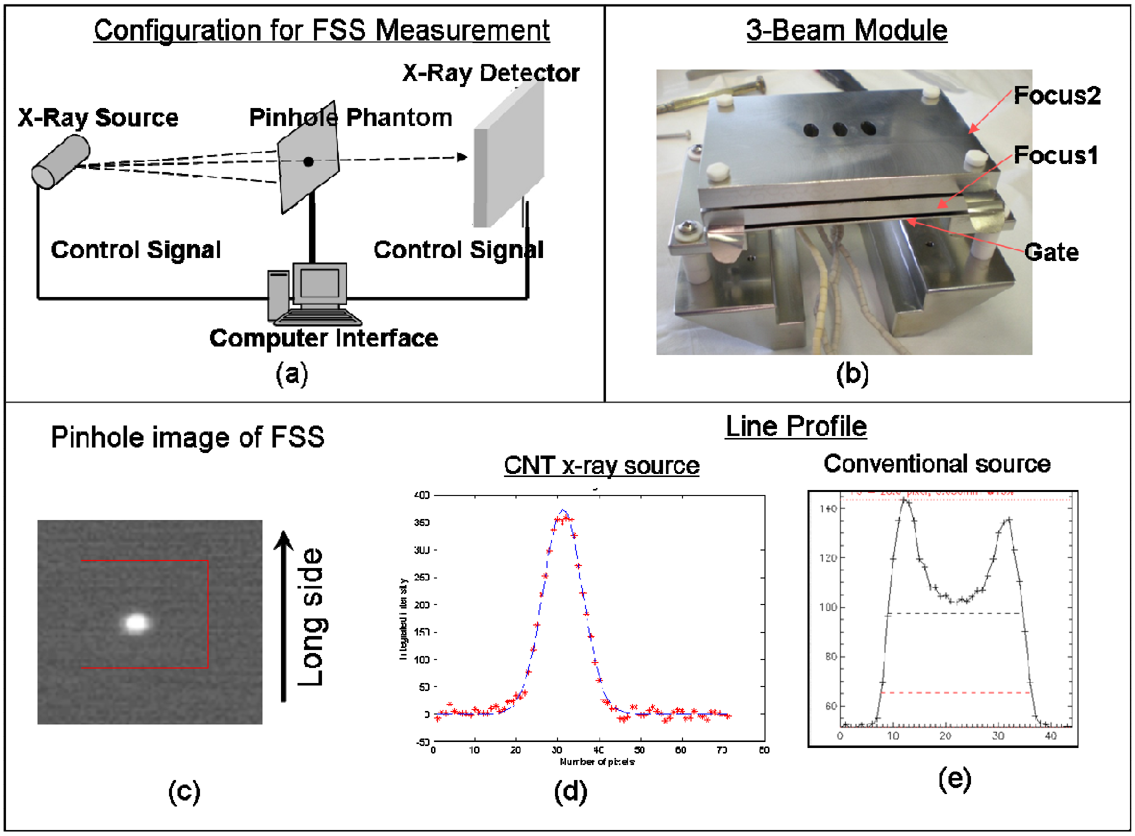

Figure 4.9: (a) Schematic representation of the FSS measurement configuration. It comprises of an x-ray source, a pinhole phantom and a 2D flat panel detector all aligned such that the central beam from the source passes through the pinhole and reaches the centre of the detector. A computer station controls the electronic interface. (b) Image of the assembled cathode unit (comprising of the cathode substrate, gate and focusing structure) used for the initial testing. (c) Representative image of an actual focal spot in 100µm pinhole configuration with typical line profile along the short axis of the focal spot (d). The profile show a Gaussian shaped intensity distribution with a single peak. (e) Shows a typical double peak often seen in conventional sources which leads to deterioration of spatial resolution.

4.8 Preliminary Simulation Study using Uniform Emission Model

Individual x-ray source design is based on the existing micro-CT geometry which consists of an Einzel type electrostatic focusing structure. However, given the cathode size and a pitch of 1.2cm it is impossible to implement the existing focusing structure. Hence, the goal is to design a simple structure which can accommodate the large cathode area. As a first step we compared different geometric structures for the active electrostatic focusing unit using an elliptical cathode of 2x8mm and studied the beam profile. Also, for simplicity of model setup, the electrons are assumed to be emitted at 90° to the surface with no divergence. This primarily affects the short axis and gives a smaller value compared to the actual number. However, the goal at this point is to study the beam profile and find a potential design and not actual focal spot size. Figure (4.10(a)) shows the structure of the x-ray source unit. It consists of a gate electrode for the extraction of electrons, an electrostatic focusing unit (comprising of Focus1 and Focus2) and a target anode.

The first study involved optimization of Focus1 geometry; hence, different configurations were considered for Focus1 electrode. For this particular setup the gate and Focus2 has a 10mm circular opening. Different geometries considered are as follows:

(a) a conical structure of bottom aperture 10mm and top aperture 15mm,

(b) a clear through-hole of 15mm in diameter, and

(c) a clear through-hole of 10mm in diameter.

Schematic representation of the different geometries can be seen in Figure (4.10(b). The primary goal is to simplify the design and to study how crucial the conical structure is for the beam profile.

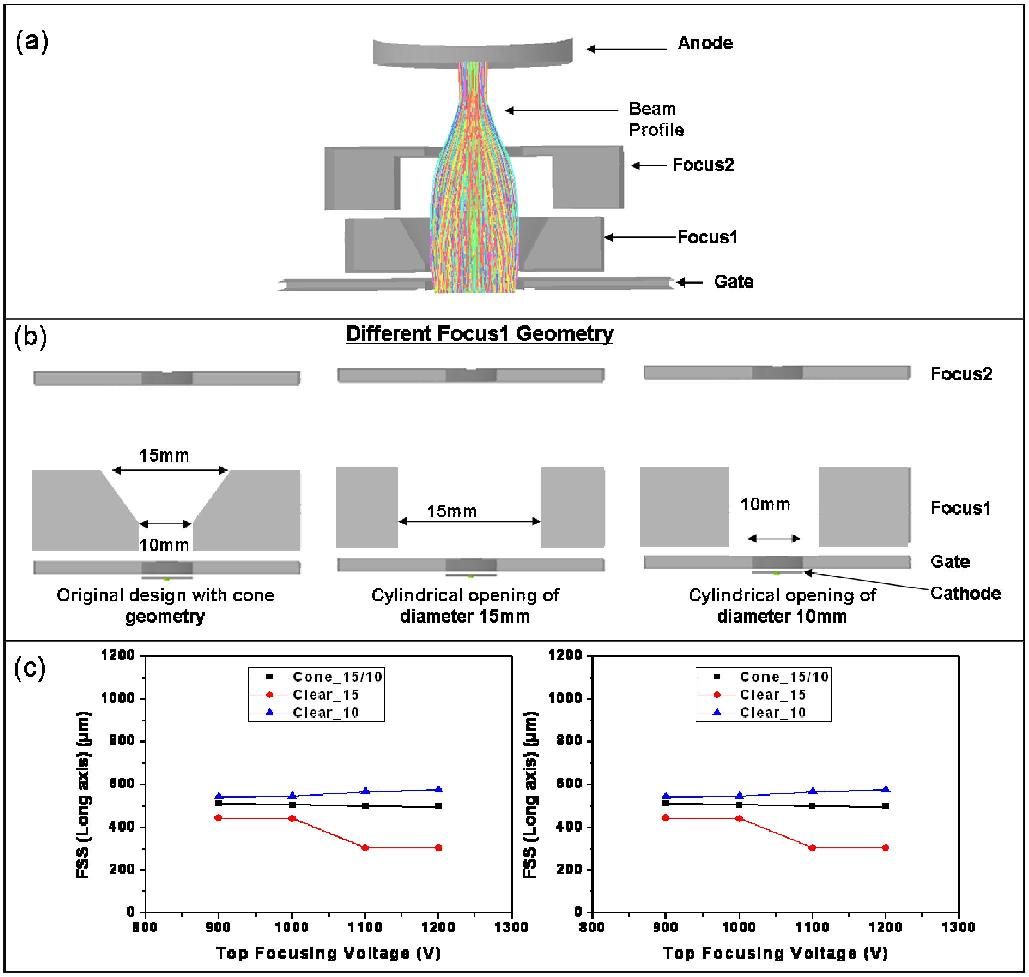

Figure 4.10: Simulation model for initial study. It is comprised of a CNT cathode, a gate electrode for extraction of electrons, an electrostatic focusing unit (Focus1 and Focus2) and an Anode. A representative electron beam profile can also be seen.

The preliminary results (Figure (4.9(c))) suggested that the conical structure is not essential. Also, when the Focus1 aperture is opened up to 15mm, it shows potential for achieving smaller FSS compared to the conical structure. This formed the basis for increasing the aperture in the long direction while the short direction was limited by the 1° pitch from the tube design. Different cathode sizes such as 2x8mm, 2x13mm and 3x13mm were considered to get a high current. The focal spot size for different emission area was studied using an initial design (let us call it Design-I). Design-I has an elliptical structure and the parameters are shown in Table (4.2). The simulations were performed at 40KV anode voltage and 1500V Gate voltage with a cathode current of 40mA using a 1D linear mesh geometry. Figure (4.10) exhibits a plot of the FSS (area) as a function of Focus2 voltage. The elliptical structure seems to be more efficient for the large cathode. About 500µm was the smallest value achieved along the long direction. Based on these results a set of measurements were conducted to confirm the predicted results.

	Gate Electrode	Focus1 Electrode	Focus2 Electrode
Dimensions (mm)	15x5	15x5	10x15

Table 4.2: Dimensions for Design-1. The electrodes have elliptical apertures.

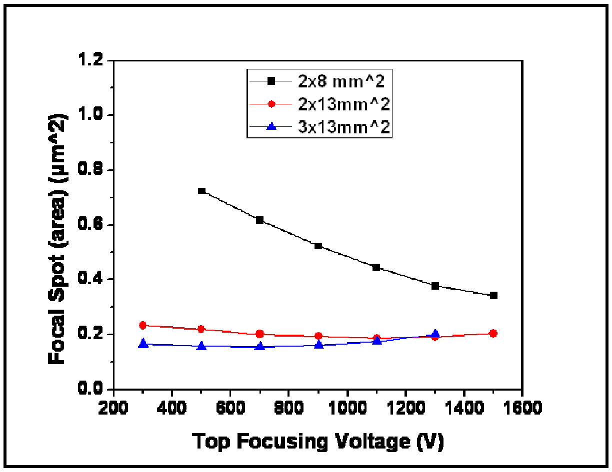

Figure 4.11: Preliminary simulation results (using uniform distribution model) showing the trend followed by FSS (area) as a function of Focus2 voltage for different cathode size. The results suggest that the focusing structure is more effective for large cathode sizes.

4.9 Results from Initial Design

A three pixel module of Design-I was built for initial testing of FSS. It consists of a gate electrode and two active focusing electrodes. The entire setup is housed in a stainless steel chamber and is pumped down to 10^{-7} Torr. The results of the initial measurements are seen in Figure (4.12). A 2x13mm cathode at 10mA current was measured at 40KV anode voltage. The results show that a focal spot size of 0.6x1.2mm (long x short) can be achieved, which is bigger than the targeted value. One primary reason for this is due to limited resources, the testing was performed with a 2D square mesh instead of the 1D linear mesh used for initial simulations. However, the measurements suggested improvements and optimization in designing was essential. One major improvement made was to replace the 2D woven tungsten mesh by a linear mesh. Details of the changes are discussed in the following sections.

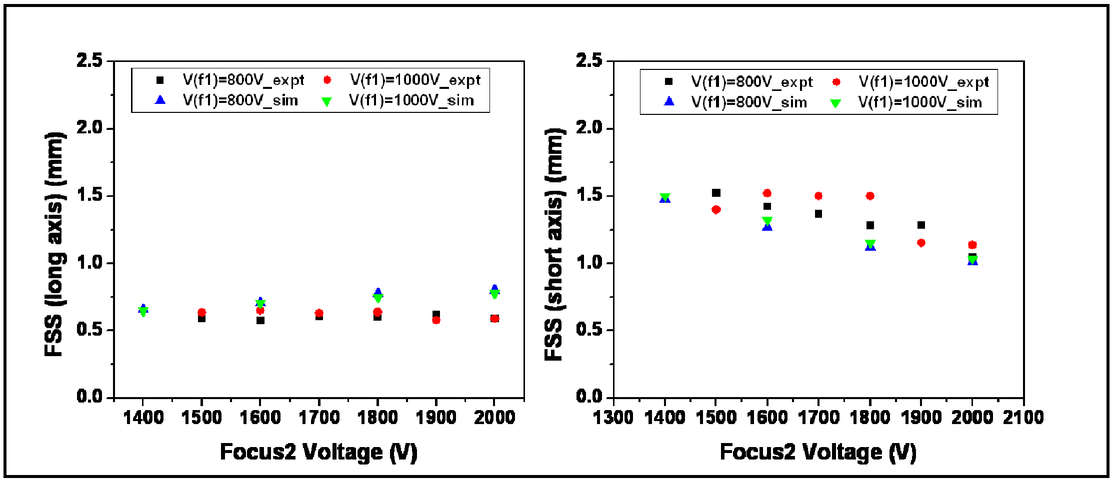

Figure 4.12: A plot of the FSS as a function of Fovus2 Voltage using Design-1. A 2x13 mm cathode at 10mA current was measured at 40KV anode voltage. The results show that a focal spot size of 0.6x1.2mm can be achieved using this design and a 2D square mesh. Simulations and experimental results show reasonably good agreement under similar conditions.

4.10 Optimized Individual X-Ray Source Unit Design

The process of design optimization involved varying different parameters such as the distance between Gate and Focus1, Focus1 and Focus2 and also Focus2 and Anode. The apertures for the electrodes can also be varied. An example has been shown in Figure (4.13), where a change in the Focus2 opening shows the change in the electron beam profile. Keeping everything fixed, a change in the Focus2 aperture shows a definite shift in the focal plane along the axial direction, which in turn changes the FSS. Thus it is crucial to note the changes in the beam profile with change in any parameter. This can be a critical guideline for design optimization.

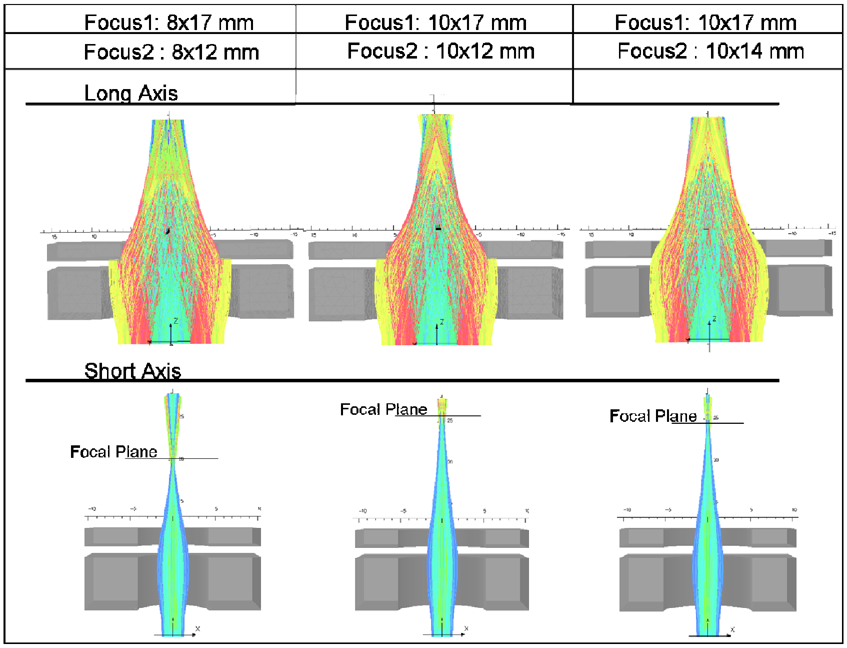

Figure 4.13: Representative beam profile exhibiting shift in focal plane along the axial direction with change in Focus2 aperture.

At this point even though the simulations seem to match the experimental results, we are not able to find a gate mesh which could sustain the high current and hence the thermal loading. From experience, tungsten would be the ideal material but due to the challenges in etching tungsten we were unable to find a supplier who could supply us with the finished product. The only option at this point was stainless steel, but given the fact that it has a low melting point we had to study different mesh geometries to see which would withstand the thermal loading. A simple model consisting of only a cathode, a gate electrode and an anode (refer Figure (4.14)) was used for this study. An elliptical cathode of 2.5x13mm was used with 190µm between the emission surface and the gate mesh. The simulations were conducted at 30 KV anode potential, 2000V gate potential at 40mA cathode current. One of the important parameters to note is the change in gate transmission with different geometry. Thermal simulations for each of these geometries were done separately by my colleague Andrew Davis. The results have been summarized in table 4.1.

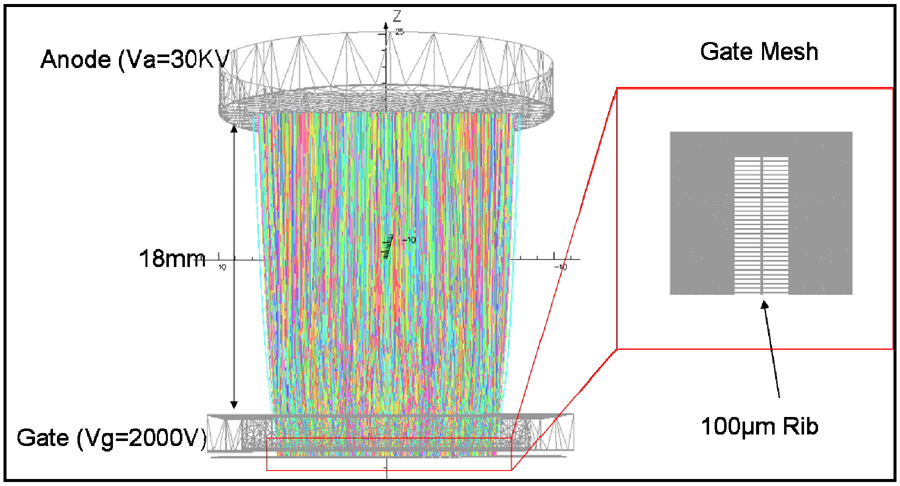

Figure 4.14:A simple model comprising of a cathode, gate electrode and gate mesh , and an anode. Inset shows the gate mesh with a rib passing through the centre. This model was used to primarily study different gate mesh geometry.

Pitch (µm)	Bar Width (µm)	Thickness (µm)	Rib (µm)	Cathode Current (mA)	Transmission Gate (%)
250	50	100	0	40.03	64.18
250	50	100	100	40.03	60.85
250	50	125	100	40.03	57.61
250	50	150	100	39.99	54.86
275	75	125	100	40.03	52.39
275	75	150	100	39.99	50.46
275	75	200	100	40.03	42.27

Table 4.3: Summarized results for different gate mesh geometry. There is an obvious decrease in transmission rate with decrease in physical opening. Also, increase in thickness of the mesh blocks more electrons resulting in a drop in the transmission.

Optimization of all the geometric parameters led to the final design as shown in Figure (4.15). The cathode assembly has an elliptical geometry with varying apertures for different electrodes. The cathode has an elliptical area of 2.5x13mm which is determined after careful consideration of emission area needed to get high current as well as sustainability of thermal loading by the gate mesh. At this point we were able to fabricate a tungsten etched gate mesh in-house. This solved all the earlier problems involving gate mesh melting (using the stainless steel mesh), high current and long exposure time.

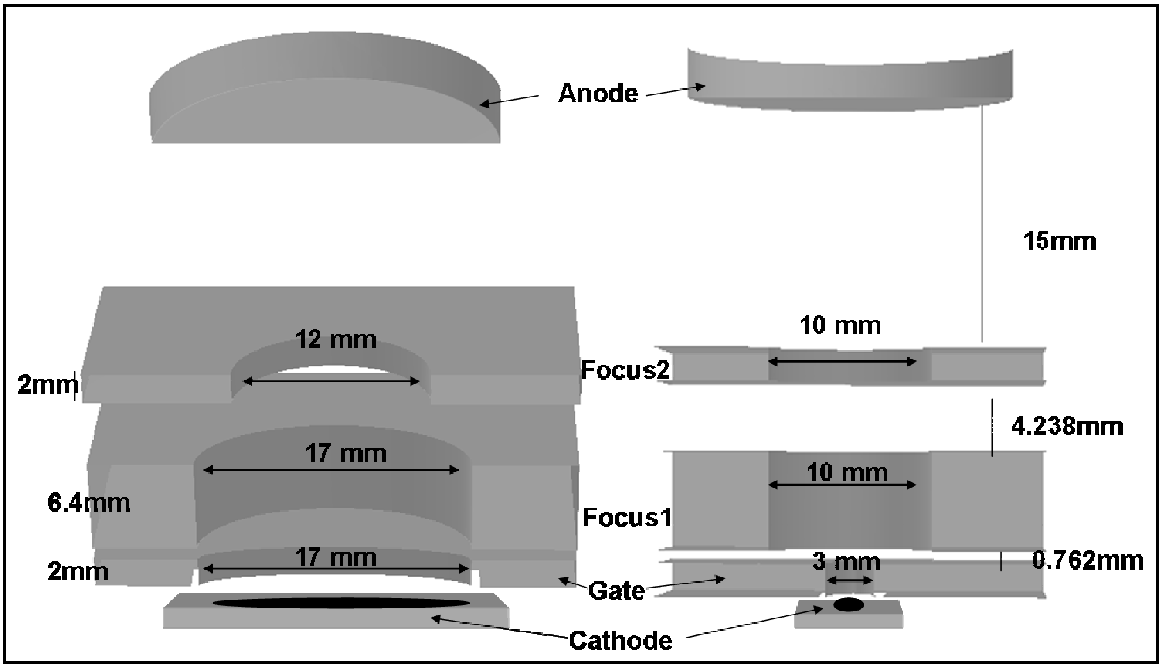

Figure 4.15 : Final design of a single cathode-anode unit. It has an elliptical cathode of 2.5x13mm, a gate electrode for electron extraction, an electrostatic focusing unit (Focus1 and Focus2) and an anode made of tungsten. The electrodes are made of stainless steel and have elliptical apertures.

Once the geometric parameters were optimized, the model was further refined with the integration of the electron divergence. This was done by the implementation of the "Random Distribution" electron emission model for specifying the initial particle dynamics. This represents a realistic model and gives more accurate results in terms of FSS and transmission rate. Figure (4.16) shows the results for the 2 types of emission models. As expected, a dramatic difference is observed in the short axis, whereas the long axis exhibits negligible difference. With the introduction of the divergence, it is more challenging to focus the beam back to a finite point, hence a larger FSS. The gate mesh used in these simulations is a linear 1D mesh. The cathode current is about 20mA and the anode voltage is 30KV.

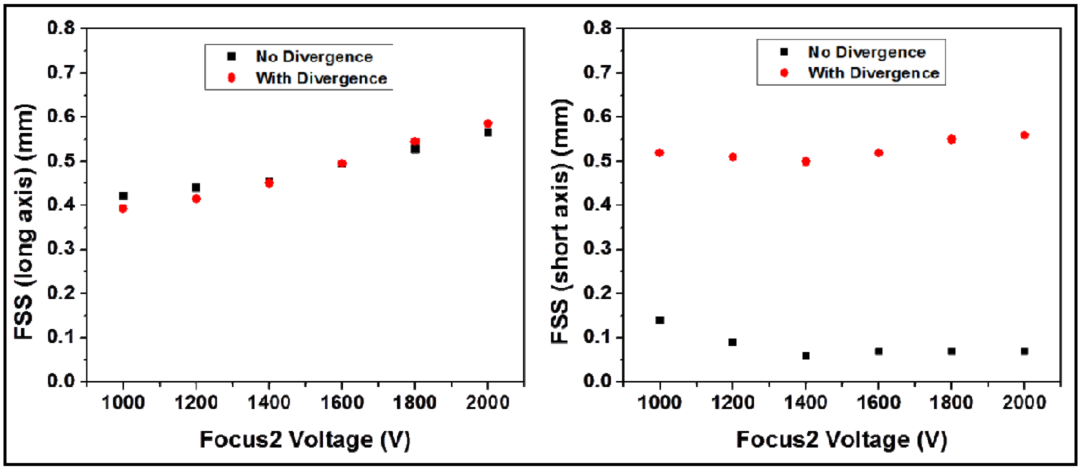

Figure 4.16: Here is a plot of the FSS as a function of the top focusing potential. The cathode used is 2.5x13mm elliptical area with a distance of 15mm between the anode surface and the top focusing electrode. Also, Va=30KV, Vg=2000V and V(f1) =1000V.

4.11 Effect of various parameters on the FSS

It is important to know the effect of different parameters on the FSS which affects the final spatial resolution of the x-ray source. Extensive electron optics simulations have been performed here to do a systematic study of the effect of different parameters. It will be discussed in detail in the following sections.

4.11.1 Effect of Distance between Focus2 and Anode

The initial simulations were performed at a distance of 15mm from the top focusing electrode to the anode surface. From experience, we know if this distance is too small it might cause arching and electrical breakdown due to the high voltage at the anode. 15mm seemed to be a safe distance in theory; however, from a manufacturing perspective, with 31 sources in a single assembly, 18mm seemed to be a safe bet. To check the effect on the FSS everything else was kept constant and only the distance was varied. The results show that the distance and the FSS are linearly related. Shorter distance seems to give a smaller FSS at 30KV anode voltage 9refer Figure 94.17)). However, the transmission does not change significantly with change in distance as can be seen in Table 4.4.

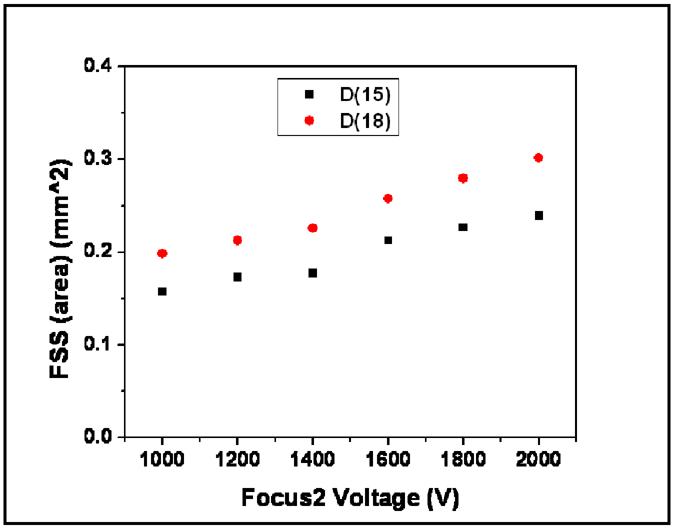

Figure 4.17: Shown is a plot of FSS (area) as a function of Focus2 voltage. We see that there is an increase in the size of focal spot area as the distance between the anode and Focus2 electrode is increased.

Distance	Cathode Current	Transmission Gate %	Transmission Anode %
D(18)	20.0	64.5	59.4
D(15)	20.0	64.5	59.8

Table 4.4: Summarized average transmission for two different distance 15mm and 18mm between the anode and Focus2 electrode exhibit no change in transmission rate.

4.11.2 Effect of Anode Potential

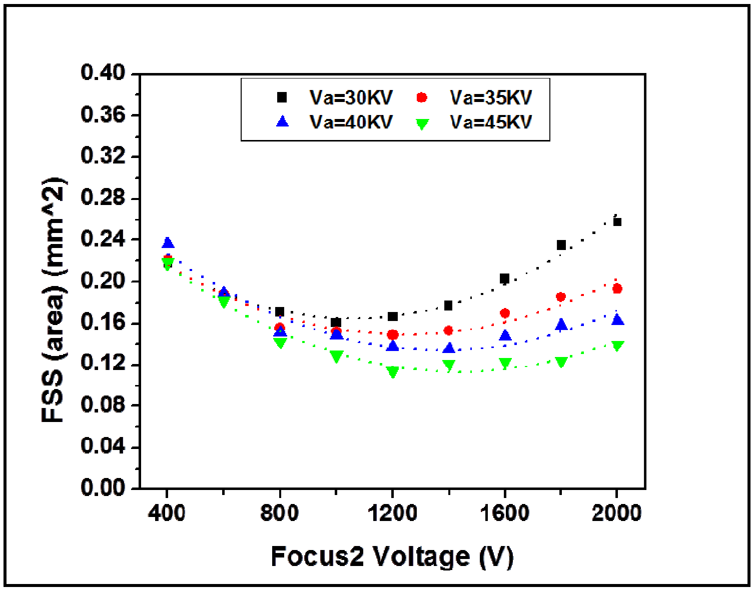

Figure 4.18: Shown is a plot of the FSS (area) as a function of the Focus2 voltage for different anode potential. The FSS (area) decrease with increase in anode potential, however, this phenomenon is observed only at high Focus2 voltage. This might mean at high Focus2 voltage the change in field distribution is significant and is demonstrated by a change in the FSS. The simulations are done at Vg =1250V and V_{f1}=1000V at 20mA cathode current.

A simulation study of the effect of the anode potential on the focal spot size was conducted. Here a cathode of 2.5x13mm has been used at 20mA current. The gate voltage and Focus1 voltages are 1250V and 1000V respectively. Figure (4.18) shows the plot of the FSS (area) as a function of the top focusing voltage for different anode potentials. As the anode potential is increased, we observe a definite decrease in the FSS, but this happens only at high Focus2 voltage. This means that at low Focus2 voltage the change in the electric field distribution is negligible with change in anode potential, keeping the FSS unaffected. However, at high Focus2 voltage, the change in field distribution is more significant and is demonstrated by a change in the FSS. The smallest FSS that can be achieved at 30KV is 470µmx530µm (long x short).

4.11.3 Effect of Focus1 Potential

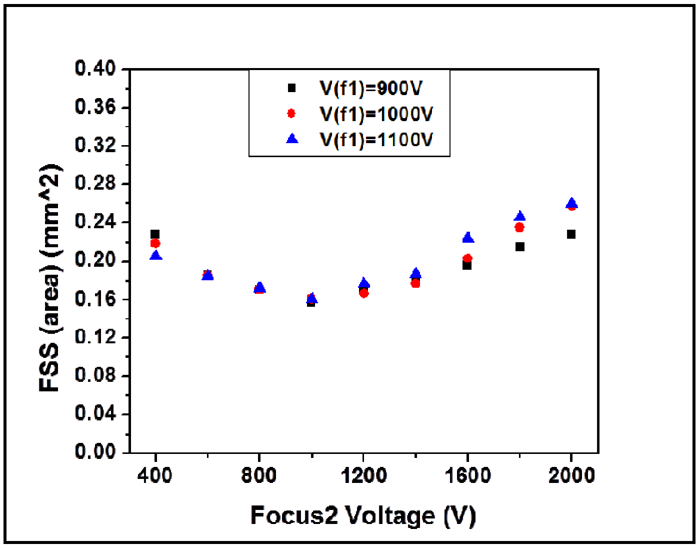

Figure 4.19: Shown is the effect of varying Focus1 voltage on the FSS (area) as a function of Focus2 voltage. It can be concluded that the FSS (area) is weakly dependent on the Focus1 voltage. It simulations were done at Va=30KV, Vg=1250V at 20mA cathode current.

Figure (4.19) shows the effective focal spot area as a function of the Focus2 potential. The plot shows the behavior at three different Focus1 voltages at, 900V, 1000V and 1100V respectively. From that the graph, it is clear that in the optimal range of operation, the focal spot is insensitive to the applied Focus1 potential but highly sensitive to the Focus2 potential. The curve shows a parabolic shape showing an optimal region of operation where the FSS is the smallest. Since the effective focal spot area is insensitive to V_{f1} that gives a broad region of operation to maintain the same focal spot area just by tuning the focusing potentials.

4.11.4 Effect of Different Current

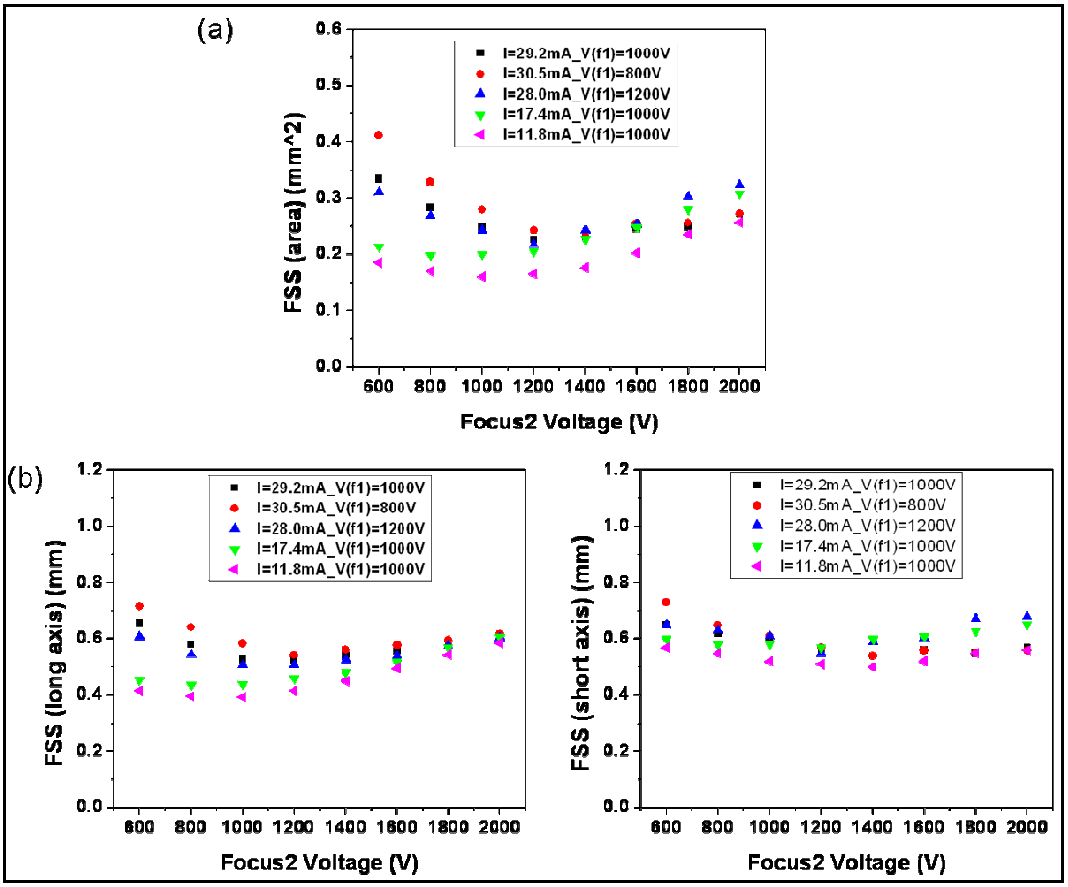

Figure 4.20: (a) Plot of FSS (area) as a function of Focus2 Voltage. (b) Plot of the FSS along the two axes as a function of Focus2 voltage. A definite increase in FSS is observed when the anode current increases (also meaning a higher gate potential) keeping the rest of the parameters fixed. The increase is primarily noticeable along the long axis and might be attributed to the large divergence caused by the mesh wires with increase in gate voltage.

Gate-Cathode Potential	Cathode Current	Anode Current	Anode Transmission
1590 V	48mA	29.2mA	60.9 %
1250 V	30 mA	17.4 mA	57.8 %
1050 V	20mA	11.8 mA	60.0 %

Table 4.5: Table summarizing the gate voltage and the corresponding cathode current, anode current and anode transmission.

We know that the field emission current is dependent on the applied electric field, in other words the cathode-gate potential. This means to increase the cathode current the gate potential needs to be increased accordingly (refer Table 4.5). Here we have studied the effect of different currents on the FSS. Keeping the anode voltage fixed at 30KV and everything else the same (V_{f1} = 1000V), the gate-cathode potential has been varied from 1050V to 1560V to increase the cathode current. The change in the voltage increases the FSS along the long axis by 200μm (refer Figure (4.20)). This phenomenon is observed only at low Focus2 voltage and might be a combination of different factors. Firstly the change in gate potential will change the electric field distribution between the gate and Focus1, thus affecting the FSS. Secondly the high gate potential will cause more divergence in the electron trajectories because of the gate mesh wires, and is mostly demonstrated by increase in FSS along the long axis. Effort has been put to achieve a smaller FSS at high current (cathode current 48mA) by tuning the focusing voltages, primarily V_{f1}. There is a shift in the plot when Focus1 voltage is changed to 800V and 1200V from 1000V; however it cannot be tuned back to the low current position.

4.12 Preliminary Experimental Measurements

A three pixel testing module was used for focal spot measurements using the pinhole method. The measurements were performed at 30KV anode potential and 20mA cathode current using a 2.5x13mm CNT based cathode. Due to availability of limited recourses at present the testing was performed with a 100μm pinhole instead of 30μm at low magnification. This translates to about an 80μm error bar. However, given the large error bar, we see reasonable agreement between simulation and experimental data as shown in Figure (4.21). A summary of the transmission can also be seen which shows quantitative agreement. A FSS of 0.5x0.6mm (long x short) is the smallest spot that can be achieved using this setup.

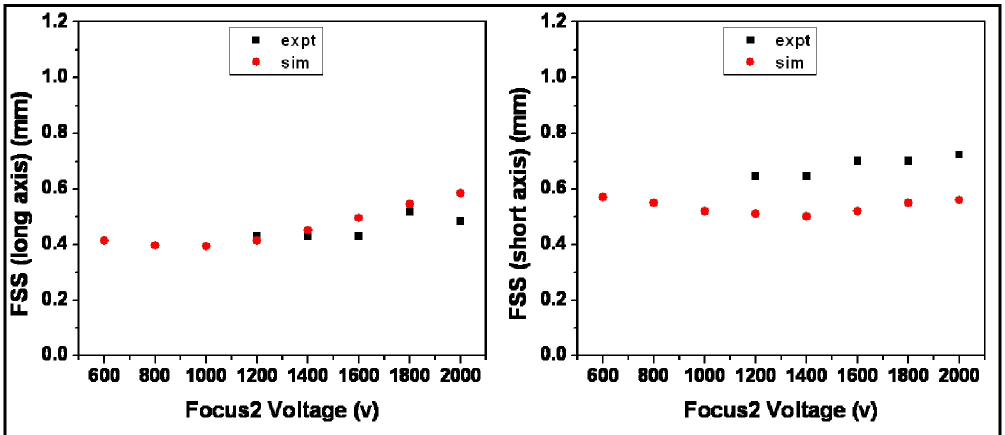

	Cathode current (mA)	Gate Transmission (%)	Anode Transmission (%)
Experiment	20.0	59.7	58.7
Simulation	20.0	64.1	59.0

Figure 4.21: Plot of FSS as a function of the Focus potential. There is reasonable agreement considering a 60µm error bar associated with the experimental data. A summary of the transmission rate show quantitative agreement. The measurements were done using a 2.5x13mm cathode at 20mA cathode current, 30KV anode voltage and 1000V Focus1 voltage. The FSS is determined using pinhole method.

4.13 Potential Improvements and Summary

Some preliminary simulations have been conducted in an effort to further reduce the FSS. This study mainly involves further gate mesh optimization keeping the same focusing structure. Three different gate mesh geometries have been studied with similar physical opening and thickness of 100µm. The primary difference is the wire pitch and the wire width as can be seen in Table (4.6).

Pitch (µm)	Bar Width (µm)	Thickness (µm)	Physical Opening (%)
250	50	100	80
200	50	100	75
125	25	100	80

Table 4.6: Table summarizing the parameters for the different gate mesh studied.

The FSS simulations have been performed at 30KV anode potential at 20mA cathode current, maintaining a distance of 15mm between Focus2 and anode. Figure (4.22) shows the FSS as a function of Focus2 potential for the different gate mesh. A definite decrease in FSS is observed when the pitch is decreased from 250µm to 200µm while maintaining the same bar width. A further decrease in size is demonstrated when the pitch is reduced to125µm. We can infer that the focal spot is highly sensitive to the pitch and this might be primarily due to a uniform field distribution on the emission surface with small pitch. There is also an overall gain in the transmission when the pitch is small (refer Table (4.7)). These are just preliminary results and need further research; however it might be the roadmap to further improvements.

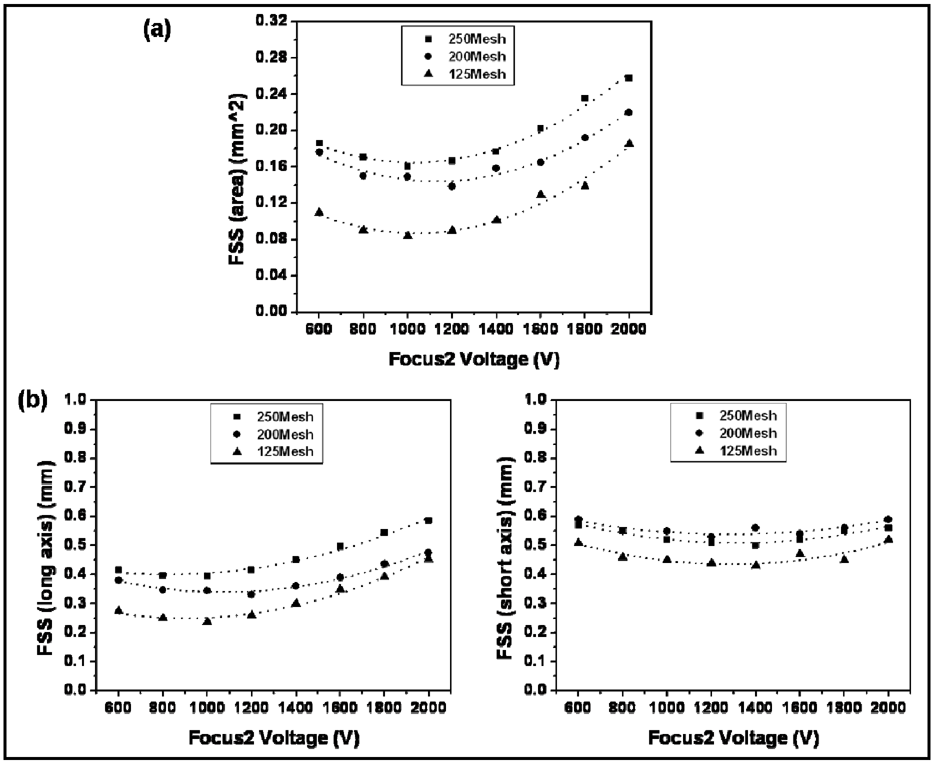

Figure 4.22: (a) Plot of FSS (area) for different gate mesh geometry. The graph suggests it is possible to achieve a smaller FSS with the current tube design just my modifying the gate mesh geometry (b) Shows the actual numbers along the long and short axis. A FSS of 0.3x0.5mm (long x short) can be achieved using this design. The simulations are done at 30KV anode potential and 20mA cathode current.

Mesh	I(cath) (mA)	Tr(gate) (%)	Tr(anode)(%)	Physical Opening
250	20.0	64.1	59.0	80.0%
200	20.0	60.5	58.6	75.0%
125	20.0	65.5	63.6	80.0%

Table 4.7: Comparison of the average transmission at gate and anode for different gate mesh geometry. The results suggest that there is an overall gain in transmission when the gate mesh has a small pitch. This might be attributed to the uniform electric field on the emission surface with small gate mesh pitch in comparison to large pitch.

4.14 Summary

A CNT based field emission x-ray source has been designed and developed. One of the primary characteristics of an x-ray source is its spatial resolution, which is determined by the focal spot size of the electron beam. Hence, a systematic study of different factors affecting the focal spot size has been conducted. We see that the focal spot size is highly sensitive to Focus2 voltage and weakly sensitive to Focus1voltage. In addition, it is also dependent on the current or gate extraction voltage. However operating in certain regimes helps in maintaining a constant FSS even for different anode current. This is very important for imaging patients of different size where the dose might needed to be adjusted by changing the anode current. Also, the intensity distribution on the anode exhibits a single peak (contrary to double peak often seen in conventional sources) which helps in preserving the spatial resolution. Extensive electron optics simulations have been performed to fully characterize the x-ray source. Initial experimental results show reasonable agreement in terms of FSS and transmission rate. This is primarily due to limited resources at present. It is an ongoing project and more testing are in progress. Some guidelines to future improvements and optimization have been provided. A prototype x-ray source with 31 beams is being manufactured right now and will soon be available for testing and characterization.

References

[1] http://www.cancer.gov/cancertopics/types/breast.

[2] Ries LAG, Eisner MP, et al.: SEER Cancer Statistics Review, 1975-2001. Bethesda, Md: National Cancer Institute, 2004.

[3] Manfred Sabel and Horst Aichinger, “Recent developments in breast imaging”, Physics in Medicine and Biology, 41 (1996) 315–368.

[4]E.D. Pisano, C.Kuzmiak, M. Koomen, and W. Cance,” What Every Surgical Oncologist Should Know About Digital Mammography”, Seminars in Surgical Oncology 2001; Special Issue: Technical Advances in Breast Cancer Diagnosis and Treatment 20:181–186.

[5] Boone JM, Nelson TR, et al. “Dedicated breast CT: radiation dose and mage quality evaluation”, Radiology 221: 657-667, 2001.

[6] Lindfors KK, Boone JM, et al., “Dedicated breast CT: initial clinical experience”, Radiology 246(3): 725, 2008.

[7] Niklason LT, Christian BT, et al.,”Digital tomosynthesis in breast imaging”, Radiology 205: 399-406, 1997.

[8] Wu T, Stewart A, et al.,”Tomographic mammography using a limited number of low-dose cone-beam projection images”, Medical Physics, 30(3), 2003.

[9] Bissonnette M, Hansroul M, et al.,”Digital breast tomosynthesis using an amorphous selenium flat panel detector”, Proc. of SPIE 5745, 2005.

[10] Ren B, Ruth C, et al.,”Design and performance of the prototype full field breast tomosynthesis system with selenium based flat panel detector”, Proc.of SPIE 5745, 2005.

[11] Guang Yang, Ramya Rajaram, Guohua Cao, Shabana Sultana, Zhijun Liu, David Lalush, Jianping Lu, Otto Zhou, “Stationary digital breast tomosynthesis system with a multi-beam field emission x-ray source array”, Proc. of SPIE Vol. 6913, 69131A, 2008.

[12] Bobb RA, Hoffman EA, et al.,” High-speed three dimensional x-ray computed tomography: the dynamic spatial reconstructor”, Proc. Of the IEEE 71(3), 1983.

[13] Lipton MJ, Higgins CB, et al.,”Cardiac imaging with a high-speed cine-CT scanner: preliminary results”, Radiology 152(3): 579-582, 1984.

[14] Speidel MA, Wilfley BP, et al.,”Scanning beam digital x-ray (SBDX) technology for interventional and diagnostic cardiac angiography”, Medical Physics, 33(8), 2006.

---

[15] X. Qian, R. Rajaram, X.Calderon-Colon, G.Yang, T. Phan, D. Lalush, JP. Lu, and O. Zhou, “Design and characterization of a spatially distributed multibeam field emission x-ray source for stationary digital breast tomosynthesis”, Medical Physics,36,10, October 2009.

[16] J. S. Maltz et al., “Fixed gantry tomosynthesis system for radiation therapy image guidance based on a multiple source x-ray tube with carbon nanotube cathodes,” Medical Physics, **36**, 5, 1624–1636, 2009.

[17] F. Sprenger et al, “Distributed source x-ray tube technology for tomosynthesis Imaging”, Proc. of SPIE Vol. 7622, 76225M , 2010.

[18] Ren B, Ruth C, et al.,”A new generation FFDM / tomosynthesis fusion system with selenium detector”, Proc.of SPIE 7622, 2010.

[19] European Committee for Standardization, EN 12543-2, 1999 E, Brussels, 1999.

Chapter 5 : Conclusion and Future Directions

In this research, topics related to development of CNT based field emission x-ray source technology and its related medical applications have been discussed. In this chapter I will summarize the results; at the same time I do realize there is potential for improvements. So I would like to finish this work addressing some future modifications.

Since the discovery of X-rays in 1895, it has opened doors to a myriad of applications. Medical imaging has been one of the prominent areas to have experienced a tremendous advancement in terms of diagnostic imaging and therapy. One of the integral components of such a device (e.g. micro-CT scanner, tomosynthesis scanner or radiation therapy system) is the x-ray source. Even though conventional thermionic x-ray sources are used widely for such systems, the thermionic technology has several limitations. The temporal resolution of a thermionic source is highly restricted by the inherent thermionic mechanism of electron production. In addition the high operating temperature results in short lifetime and large device size. On the contrary, field emission x-ray source can address most of these limitations. It has the capability of high temporal resolution up to microsecond and can generate pulsed x-ray in arbitrary waveform. Since its discovery in 1991 CNTs have been demonstrated to be excellent field emitters. Integrating CNTs as field emission x-ray sources has been relatively a new field. This novel x-ray source has the potential to replace conventional thermionic sources in many applications.

Development of a CNT based field emission x-ray source for medical device has been the focus of this work. One of the primary characteristics of an x-ray tube is its flux and spatial resolution. In this work, electrostatic focusing has been exclusively used to focus the electron beam. However, experimental demonstration of such a novel x-ray source would be impossible in the absence of a substantial development program. Instead, simulation tools have been employed to aid the design of the micro-focus tube. In addition, the lack of suitable methods of representing the electron emission characteristics of the CNT cathode resulted in the development of an emission model. A simple but intuitive emission model to emulate the behavior of a CNT cathode has been developed. This model takes into consideration the random distribution of CNTs on macroscopic emission area and their varying field enhancement factor. Even though a working model has been created which exhibits quantitative (within ~16%) agreement with measured results there is always room for further improvement. Further refinement of the model is possible by using the actual average field enhancement factor for generating the current distribution instead of using the effective $\overline{\beta}$ used from the cathode performance directly. Also, assumption of uniform velocity distribution along its angular components has been made. This can be further improved by integrating some kind of weighted distribution along the field direction. Extensive electron optics simulation using this emission model has been done to study the behavior of the CNT field emission x-ray source. A prototype x-ray tube was built in the lab for experimental validation of the simulated data.

An isotropic focal spot size of 100µm can be easily achieved using this tube design. Feasibility of such a tube being used as an integral part of a dynamic micro-CT scanner has been demonstrated. Some representative cardiac gated mouse images have also been presented. The tube design can also be translated to a spatially distributed multi-beam x-ray source array and has been successfully integrated into a stationary micro-CT configuration. A high power CNT field emission x-ray source has also been successfully designed and characterized. It is part of a multi-beam stationary DBT scanner operating at 100mAs with a scan time of 4s and 15 views. This is an ongoing project.

However, there are still plenty of challenges and opportunities remaining. As mentioned previously, for the micro-focus tube, the lens becomes ineffective for focal spot size less than 60 µm with the present design. The present design limitations on the focal spot size bring out new ideas to achieve smaller focal spot size. Preliminary simulation studies have been done with a knife-edge anode geometry which shows the potential to achieve smaller focal spot. A doughnut shaped cathode geometry might also help to achieve the same goal. For the prototype high power x-ray source, the focal spot size is larger than the target size of 0.3x0.5mm. However, preliminary studies show that design optimization of the gate mesh geometry with the same tube geometry might solve this problem. An alternative focusing structure will also achieve the same goal.

Overall, a simulation platform to perform reliable electron optics simulations has been developed and implemented to design CNT based field emission x-ray sources. The x-ray sources are tailored for particular application and have been successfully integrated into prototype micro-CT and stationary digital DBT scanners. Such scanners can have a significant impact in the field of medical imaging and diagnostics.